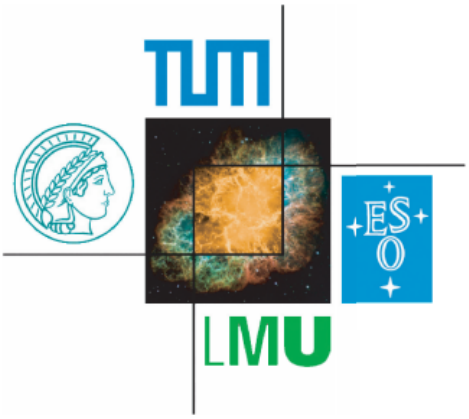

Technische Universität München

Partial Wave Analysis for Cusp Structure in $p+p \rightarrow p + K^+ + \Lambda$ Data

Master Thesis

Physik-Department E12 - Dense and strange hadronic matter

Excellence Cluster - Origin of the Universe

Shuna Lu

December 14, 2015

i

First reviewer: Prof. Dr. Laura Fabbietti

Second reviewer: Prof. Dr. Elisa Resconi

Scientific supervisor: Robert Münzer

Abstract

The associated strangeness production of K^+ and Λ is the energetic lowest possibility of creating particles with open strangeness in nucleon nucleon collisions. It has been extensively studied in proton proton collisions by the DISTO, COSY-TOP, FOPI and HADES collaborations. For these analysis it was shown the a cocktail of different production channels can contribute to the final state. Also interference plays a important role. Beside this effect it has another effect, which is visble by excess in the pΛ invariant mass spectrum. This excess orginates in the opening of the Simga-N channel creating an Cusp effect. These are at 2128.94 MeV (for nΣ^+) and at 2130.9 MeV (for pΣ^0). This effect is called as NΣ Cusp effect.

The present work is focused on the Partial Wave Analysis (PWA) of exclusive pp $\rightarrow$p + K^++ Λ events based on Bonn-Gatchina PWA Framework, which is able to fit a coherent sum of a set of transition waves to the experimental data. To describe the NΣ cusp effect, the Breit-Wigner distribution was used before but solely as a tool to determine the peak positions and widths of the cusp structure without physical interpretation. In this work, the Flatté parametrization is used, for it is considered to be more adequate for amplitudes near a threshold and provides more factors to interpretate this cusp phenomenon.

The datasets are mainly from DISTO collaboration with beam energy of 2.14GeV, 2.5GeV and 2.85GeV and from COSY-TOF collaboration with beam energy of 2.16GeV. It will present in this work the PWA analysis of single data sample, separately and later the combined data analysis to reduce the ambiguity of the results. It shows that PWA analysis give a nice agreement with experimental data, especially can reproduce quite nicely with a Flatté -like paramtezied Cusp waves. The fitting results of BG-PWA converges with negative Log-likelihood value and small χ^2 /ndf values. The realtive strength of all contribution channels shows that all datasets are that $N^*(1720)$, $N^*(1875)$, and $N^*(1900)$ contribute quite small, which also indicate they are not necessary for describing the data set. All systematic errors are below 10%. The scattering length for NΣ can be calculated as $\approx (0.637 - i0.1453) fm$ for combined data analysis of four data samples.

Contents

Chapter I

Introduction

1.1 Strong Interaction

The strong interaction between quarks and gluons is described by quantum chromodynamics (QCD). QCD is a type of quantum field theory called a non-abelian gauge theory with symmetry group SU(3). Since the gluons also carry charge, phenomena like gluon-gluon coupling appear, which leads to effects like asymptotic freedom and confinement [30].

1.1.1 QCD Phase Diagram

One property of QCD is asymptotic freedom. It states that the interaction strength between quarks becomes smaller as the distance between them gets shorter. The other prominent features of QCD at low-energy is color-confinement: Any strongly interaction system at zero temperature and density must be a color singlet at distance scale larger than $1/\Lambda_{QCD}$. As a consequence, isolated free quarks cannot exist in nature.

The different phases of the nuclear matter can be illustrated by the phase diagram of the nuclear matter in Figure 1.1. At low energies and low baryonic density the quarks form hadrons. Due to the asymptotic freedom of the QCD, at higher energies and densities, the coupling constant reduces, which leads to a transition to a deconfined phase - the Quark Gluon Plasma (QGP) - with freely moving quarks and gluons [12] [18]. The transition to this QGP phase is predicted to happen at low baryonic densities in a smooth cross-over. With increasing energies a critical point is predicted with a second order phase transition followed by an transition region (yellow band) in which first order phase transition appears. [30]

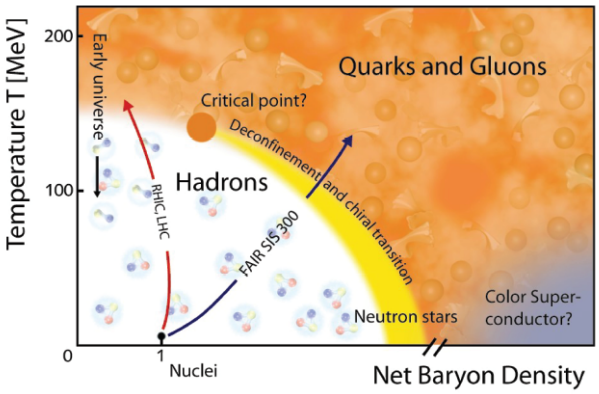

Figure 1.1: Phase Diagram of nuclear matter [31]. At low energies and low baryonic densities the quarks form hadrons. The yellow band indicates the temperatures and densities at which a first order phase transition from the hadronic phase to the quark gluon plasma takes place. At the critical point the first order phase transition turns into a second order phase transition, while at low densities and higher energies a crossover between the two phase is predicted. The arrows indicate the regimes, which will be accessible by experiments at the LHC, RHIC (red) and future experiment at FAIR (black).

1.1.2 Equation of State

The behaviour of the hadronic matter depending on the temperature and the density is described by the equation of state (EoS). The equation of state is used to describe the energy density of hadronic matter as a function of density and temperature. The determination of the EoS for hadronic matter is very important for the understanding of objects like neutron stars. Indeed, inside of such objects, high densities of nuclear matter can appear and depending on the EoS of hadronic matter different hypotheses about the components of the inner core of neutron star can be validated.

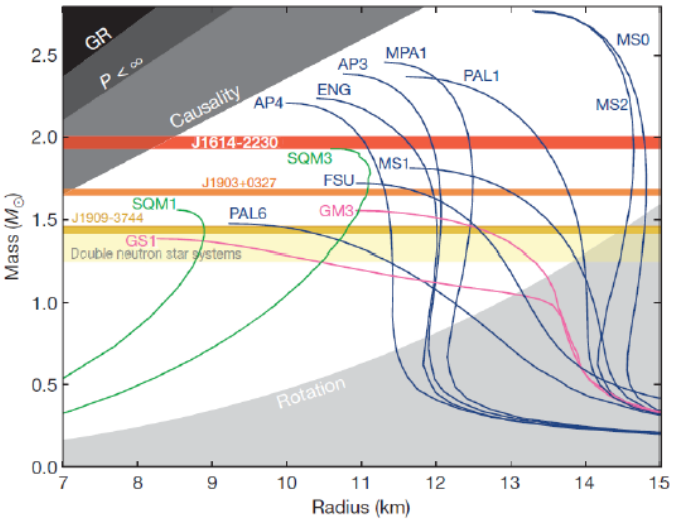

Figure 1.2: Neutron star mass versus the radius [13]. The different lines represent different theoretical predictions, like nucleonic matter (blue lines), nucleonic plus exotic matter (pink lines) or strange quark matter (green lines) [24]. The horizontal bands are constraints from measurements of neutron stars. [13] [22] [8]

In Figure 1.2, a diagram of neutron star mass versus the radius of the neutron star is shown. In this picture, the predicted mass-radius relation from different theoretical models, based on different EoS, are presented. While these results seem to favour a stiff equation of state with pure nucleonic matter, it was shown by theoretical calculations [43], that from certain energy densities the production of strange hadrons, like Λ and K^-, might be energetically favorable [39]. Although those effects could lead to a softening of the equation of state, they are not completely ruled out by the constraint of neutron star mass measurements [41]. In detail the open question turns to be, which strength of interaction of Nucleon and Hyperon has a major impact on the formation of particle in neutron stars. It is important for study Hyperon production and its mechanism.

1.2 Hyperon Production

1.2.1 OBE Model

In particle physics, a hyperon is any baryon containing one or more strange quarks. Since the discovery of strangeness, the hyperon nucleon (YN) interaction has been of fundamental interest both theoretically [11] as well as experimentally [2]. Unfortunately, since hyperons are short lived, this energy region is practically inaccessible by hyperon beams. Thus, possible bound states are indispensable as the source of information.

Theoretically, the production of Hyperons can be described by the One Boson exchange Modell (OBE). In this modell, a large variety of theoretical approaches to describe hyperon (Y) production in proton-proton collisions can be ordered into two classes of production scenarios depicted in Figure 1.3.

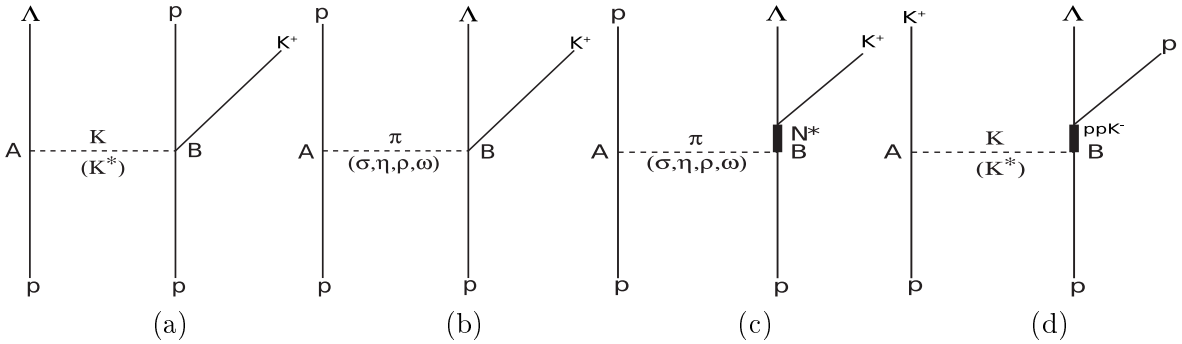

Figure 1.3: Feynman diagrams of the production of p + K^++ Λ according the one boson exchange model [42].

In Figure 1.3, on the one hand, kaon (and K^*) exchange manifests strangeness in the production mechanism itself. In this case resonances could be involved in principle, however, none is known in the Kp-system at present. On the other hand, π (and σ, η, ρ, ω) exchange shifts the strangeness production away from the interaction of both protons to the $p\pi \rightarrow$KY vertex. Since the subprocess $p\pi \rightarrow$KY is likely to involve an intermediate resonance (p$\pi \rightarrow N^*;\theta^*$; $N^*/\theta^* \rightarrow$KY), this scenario suggests the role of resonances to be of importance for proton-proton induced hyperon production. [42] It is not possible to measure one of these process separately, but can measure a combination of all of them.

1.2.2 p + K^++ Λ Production

The associated strangeness production of kaon and lambda is the energetic lowest possibility of creating particles with open strangeness in nucleon nucleon collisions. It in proton proton collisions has been extensively studied by the DISTO collaboration [5], the COSY-TOF collaboration [10], close to threshold by the COSY11 collaboration [40], and at a higher beam momentum by the HADES collaboration [17].

In spite of large experimental data base of p + K^+ + Λ production, no conclusive solution has been found on the exchange mechanism. While measurements of the spin transfer coefficient of the DISTO experiment indicate kaon exchange, COSY-TOF measurements yield a large N* contribution [10], which is a sign for dominant pion exchange [9]. Besides, this elementary reaction is also the basis of more complex reactions, which are under investigation and which need the precise knowledge of its observables. Among these complex reactions are the properties of hypernuclei [33], the possible existence of ppK cluster or bound states [16], and the prediction of strangeness enhancement in heavy ion interactions as a sign for the quark gluon plasma [9].

1.3 NΣ Cusp Phenomenon

In this work it mainly concentrates on the pΛ interaction at energies close to the threshold of the NΣ interaction. These are at 2128.94 MeV (for nΣ) and at 2130.9 MeV (for pΣ^0). This Σ-N cusp effect, which appears at or above the threshold mass for production of pK^+ $\Sigma(2130\,\mathrm{MeV/c^2})$, is interpreted as the result of a coupled channel interaction of Σ-N and p-Λ production. At these threshold, an excess in the production yield is observed, which is associated as an NΣ Cups effect. Due to the virtual character of the intermediate Σ-N state, this channel also interferes with the other p + K^+ + Λ production channels. In fact, it is difficult to study NΣ interaction, for example since they can not be studied via Hypernuclei, for which are very short-living. However, a series of both theoretical and experimental work are done all along.

1.3.1 Theoretical Interpretation

Recalling some coupled-channels dynamics [4] [38], conservation of flux and the associated unitarity of the S-matrix necessarily imply anomalies at the opening of new thresholds [38]. Specifically, at an S-wave threshold the cross section as a function of the energy will have infinite slopes at such a threshold in general. The resulting structures are usually called cusps or rounded steps, depending on their specific shape [4] [38]. Whether these structures remain primarily of academic interest or manifest themselves via large, experimentally observable effects depends strongly on the strengths of the interactions in the coupled channels. In particular, pronounced threshold phenomena always go along with near-by poles in the scattering amplitudes of the involved channels that are associated with (inelastic) virtual states or (unstable) bound states [4] [29]. In other words, It could be a cusp structure due to (and at) the opening of the NΣ threshold and then would be a signal for an inelastic virtual state or due to a bound pΣ^0or nΣ^+ state, i. e. a deuteron-like but unstable bound state. In the latter case the peak of the cross section has to be below the NΣ threshold. In principle, it could also be a pΛ resonance above the NΣ threshold. [25]

Modern meson-exchange models of the YN interaction such as the Juelich [20] [21] or Nijmegen potentials [34] [26] are derived under the assumption of (broken) SU(3) symmetry. This symmetry implies, that the strongly attractive forces that yield the deuteron bound state (in the 3S1-3D1 partial wave) and a virtual state in the 1S0 partial wave in case of the NN system will likewise act in the strangeness $S = -1$ sector. Specifically, there is a strong

coupling between the $N\Lambda$ and $N\Sigma$ systems. It is caused by the long-ranged tensor force provided by pion exchange and boosted by the fact that the thresholds of the two channels are only separated by 77 MeV. Therefore, it is not surprising that practically all YN interactions that fit the data and include explicitly the coupling between the $N\Lambda$ and $N\Sigma$ channels predict also sizeable threshold effects. [25]

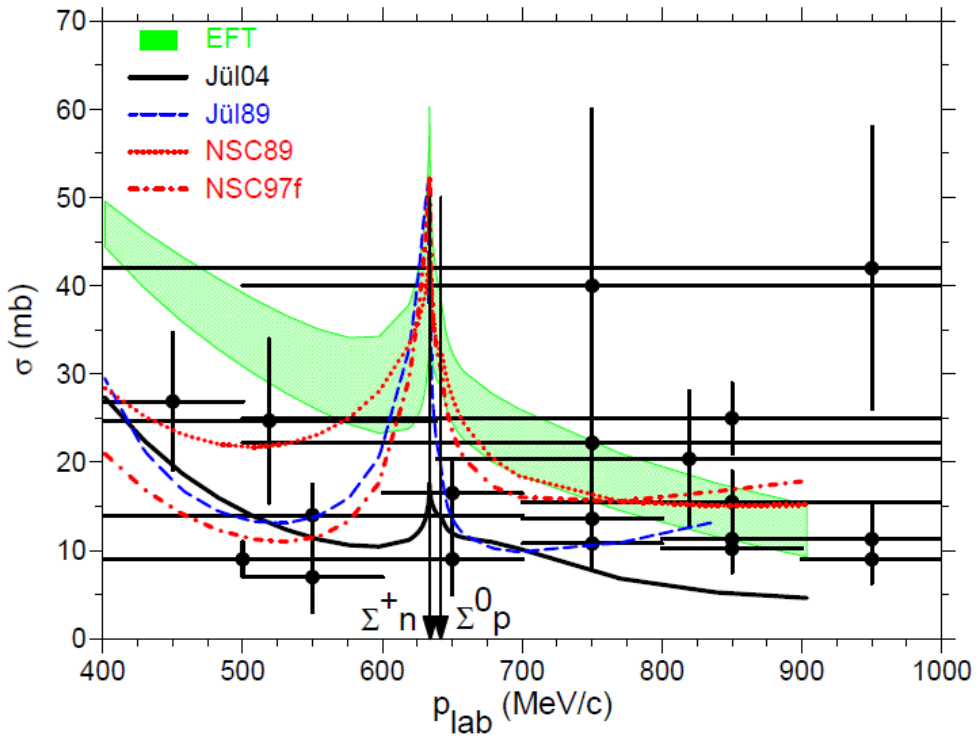

Figure 1.4: Cross sections for elastic $p\Lambda$ scattering. The curves are results from YN models, namely from the Nijmegen YN soft-core potentials NSC97f [34] (dashed curve) and NSC89 [26](dash-dotted curve), and from the Juelich one-boson-exchange models [20] (solid curve). and [21](dashed curve). Results obtained at leading-order chiral EFT [32] [19] are indicated by the grey band. The thresholds for the reactions $p\Lambda \rightarrow N\Sigma$ are indicated by arrows [25].

Experimentally, in principle, the $p\Lambda$ interaction could be studied in the range of interest, i. e. in the vicinity of the $N\Lambda$ thresholds by elastic scattering. In Figure 1.4 all cross sections [38] , to the best of our knowledge, for elastic scattering in a momentum range from 400 MeV/c to 1 GeV/c are collected.

Here the computation of the cross section was done in particle basis so that the $n\Sigma^+$ and $p\Sigma^0$thresholds could be correctly implemented. Partial waves up to $L \leq 2$ have been taken into account. Note that the agreement between data and calculations at low energies (not shown here) is of similar quality for all models.

1.3.2 Experimental Results

The experimental results for the NΣ cusp effect is firstly visible in the Dalitz plots in Figure 1.5, measured by COSY-TOF collaboration. A Dalitz plot is a representation of the transition of an initial state to three particles and also shows the kinematics of the process.

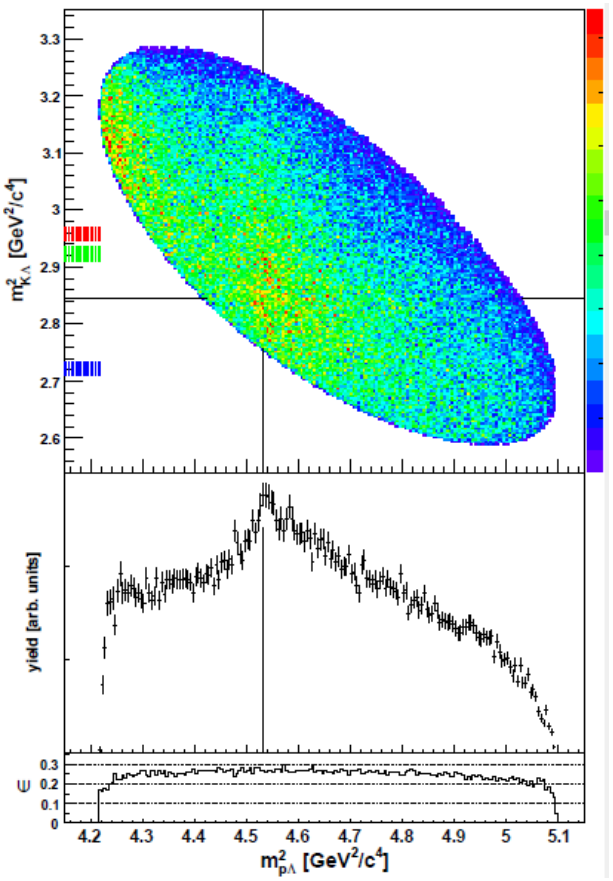

Figure 1.5: Top: The Dalitz plot of the measured data. The black horizontal line indicates the KΣ threshold, the vertical one the NΣ threshold. The red area at the ordinate indicates the mass of the N^* (1720) resonance, the green area indicates the N^* (1710) resonance, and the blue area the N^* (1650) resonance. Middle: The projection on the squared invariant mass pΛ is shown. This projection is corrected by the combined detector and reconstruction efficiency, which is shown in the bottom frame. The $N\Sigma$ threshold is indicated by the black line [9].

In Figure 1.5, the Dalitz plot of the measured data is shown. The black horizontal line indicates the KΣ threshold, the vertical one the NΣ threshold. The red area at the ordinate indicates the mass of the N^* (1720) resonance, the green area indicates the N^* (1710) resonance, and the blue area the N^* (1650) resonance. The projection on the squared invariant mass pΛ is also shown. This projection is corrected by the combined detector and reconstruction efficiency, which is shown in the bottom frame. The $N\Sigma$ threshold is indicated by the black line [9]. In the figure, two dominant structures, which are stretched mainly in the vertical direction, are observed. The first one is located at low pΛ invariant masses and arises from the pΛ final state

interaction [9]. The second structure located at the NΣ threshold has its maximum intensity around $m^2_{K\Lambda} \approx 2.85 GeV^2/c^4$ and extenuates with rising KΛ invariant mass. In Dalitz plot of $m^2_{K\Lambda}$ versus m^2_{pK} again shows a structure with strong intensity variation connected to the NΣ threshold. No structures at the KΣ threshold or near the resonance masses can be detected. [9]

1.3.3 Mass and Width

In Figure 1.6, the pΛ invariant mass spectrum is shown together with the COSY-TOF analysis result [1], according to which the cusp structure appears at a pΛ invariant mass of 2.13 GeV/c^2 and has a width of about 0.02 GeV/c^2

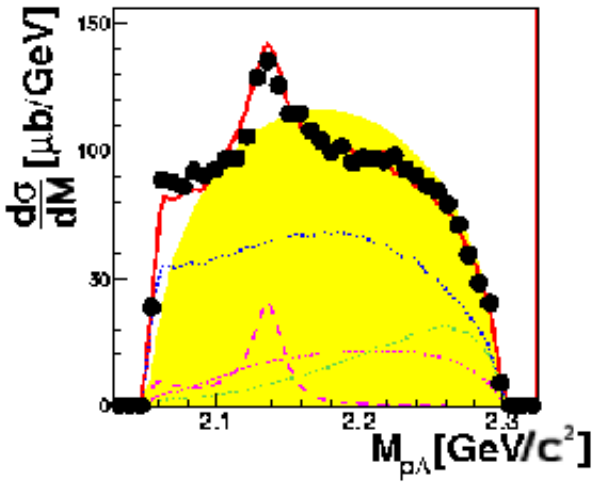

Figure 1.6: Differential distributions of the invariant-mass system of Λ -p measured by the COSY-TOF experiment at beam energy of 2.28 GeV. The shaded areas indicate phase-space distributions, the dotted lines the contributions of N^* resonances, the dashed line the Σ-N cusp effect and the solid line the full MC simulation [1].

1.3.4 Spin Parity

Since the production via these channels happen directly at threshold, the Σ and N are expected to be in a relative s-wave state, which means that the spin-parity of the system is either $J^P = 0^+$ or 1^+ [1]. The resulting pΛ system then may appear in an s-wave state in case of $J^P = 0^+$ or in an s- or d-wave state in case of $J^P = 1^+$, which has also been confirmed through an analysis of the Σ-N cusp done by the COSY-TOF collaboration [1].

1.3.5 Flatté and Breit-Wigner Spectra Function

A possible description of the spectra function of the cups phenomen is given by using a Flatté -like parametrization [6]. The amplitudes A of partial waves are then parametrized by:

$$A = \frac{C\sqrt{\Gamma_{p\Lambda}\,\Gamma_0}}{(M^2 - s - \mathrm{i}(\Gamma_{p\Lambda} + \Gamma_{p\Sigma^0})M)}, \tag{1.1}$$

$$\Gamma_{p\Lambda} = g_{p\Lambda}\, q_{p\Lambda}\ , \tag{1.2}$$

$$\Gamma_{p\Sigma^0} = g_{p\Sigma^0} q_{p\Sigma^0}, \tag{1.3}$$

Above threshold:

$$q_{p\Sigma^0} = \frac{\sqrt{(m^2_{p\Sigma^0} - (m_p + m_{\Sigma^0})^2)(m^2_{p\Sigma^0} - (m_p - m_{\Sigma^0})^2)}}{2m_{p\Sigma^0}}, \tag{1.4}$$

Below threshold:

$$q_{p\Sigma^0} = \mathrm{i}\frac{\sqrt{((m_p + m_{\Sigma^0})^2 - m^2_{p\Sigma^0})(m^2_{p\Sigma^0} - (m_p - m_{\Sigma^0})^2)}}{2m_{p\Sigma^0}}, \tag{1.5}$$

The g and q are coupling constants and cm momenta, respectively, in the corresponding two-body subsystems. For N-Σ the mass value of proton and Σ^0 are used. A crosscheck with the PWA has shown, the the difference for this case are negligible than to usage of the masses of n and Σ^+. The plotting of spectral function of Flatté with specific values of parameters is shown in Appendix C.a, together with functions plotting of relative momentum of Flatté and total width.

If $g_{N\Sigma} \gg g_{N\Lambda}$, we have a very asymmetric distribution with a trailing slope at energies below the cusp and a rapid decline beyond the cusp [6]. The factor Γ_0 is the Branching ratio to the initial channel, which only plays a role in the presence of a resoance, which is not the case for this channel, so it is normally treated as a constant.

If $g_{N\Sigma} \ll g_{N\Lambda}$, then the Flatté distribution approaches a symmetric distribution. The relativistic Breit-Wigner distribution is implemented on Σ-N cusp effect as the cusp is a resonance structure in analogy with the N^* production. The amplitudes A of partial waves are parametrized by:

$$A = \frac{1}{(M^2 - s - \mathrm{i}M\Gamma)}, \tag{1.6}$$

Fitting-parameters are the width Γ and M, the centroid of the peak. The Breit-Wigner distributions are used here solely as a tool to determine the peak positions of the structures seen in the various experiments and to obtain values for the widths that can be compared with each other. They are not meant as a physical interpretation of the data. It is just the simplification for the case, that NΣ coupling in Flatté is very small, so that the cusp shows an sysmmetric shape.

1.4 Scattering Length

The invariant mass distributions of strangeness production allows the interaction of the involved particles to be studied as a function of the relative energy in the range from zero to several hundred MeV. Especially the measurement of the nucleon hyperon missing mass distributions starting from zero interaction energy enables the determination of the nucleon hyperon scattering length [9]. Using this method one can only measure the pΛ scattering length. The strength of the nucleon and hyperon interaction is represented through the scattering length of pΛ and NΣ , which chould be calculated by the coupling constants and threshold mass in the Flatté distribution [6]:

$$a_{N\Sigma} = -\frac{g_{N\Sigma}}{2E_{BW} - i\Gamma_{p\Lambda}} = -\frac{1}{q_{p\Lambda}}\frac{R}{\alpha^2+1}(\alpha + i), \tag{1.7}$$

$$E_{BW} = E - E_{threshold} \tag{1.8}$$

$$\alpha = \frac{2E_{BW}}{\Gamma_{p\Lambda}}, \tag{1.9}$$

$$\Gamma_{p\Lambda} = q_{p\Lambda} * g_{p\Lambda} , \tag{1.10}$$

$g_{N\Sigma}$ and $g_{p\Lambda}$ is the coupling constant for NΣ and pΛ in Flatté -like function and R is $g_{N\Sigma}$ divided by $g_{p\Lambda}$. E is peak position of cusp and $E_{threshold}$ is pole mass($\approx 2132 MeV$), $q_{p\Lambda}$ is relative momentum for pΛ $\approx$ 283.8MeV/c.[1] Since the ratios R and α can be extracted from a study of the near-threshold momentum dependence of the invariantmass spectrum, a determination of the (complex) NΣ scattering length is also feasible.

[1] 1fm $= 5.0677 * 10^{-3} (MeV)^{-3}$

Chapter II

Datasets and Detectors

2.1 Datasets

The datasets used for the PWA analysis of cusp phenomenon are from DISTO and COSY-TOF Collaborations. The aim of a combined analysis approach is to perform a combined analysis of several experimental data sets taken at different experimental facilities. In Table 2.1, the list of these experiments is given.

experiment	E_{Beam} (GeV)	$\sqrt{s}$ (GeV)	$\epsilon_{p + K^+ + \Lambda}$	statistics	polar.
DISTO [27,28]	2.14	2.75	200.44	76982	Y
DISTO [27,28]	2.5	2.87	318.86	80000	Y
DISTO [5,27,28]	2.85	2.98	430.48	182597	Y
COSY-TOF [37]	2.16	2.75	203.69	43662	Y
FOPI [30]	3.1	3.06	508.97	903	N
HADES [14]	3.50	3.18	629.33	213155	N

Table 2.1: List of available statistics of the reaction p+p→p + K^++ Λ obtained by the COSY-TOF , the DISTO , the FOPI and the HADES collaboration. In the list the beam energy and the center-of-mass energy $\sqrt{s}$ (given in GeV), excess energy $\epsilon_{p + K^+ + \Lambda}$ for the p + K^++ Λ production(given in MeV) and the amount of statistics are shown. The data samples, for which a polarized beam respectively target was used, are marked (polar.).

In Table 2.1, the beam energy and the center-of-mass energy $\sqrt{s}$ (given in GeV), excess energy $\epsilon_{p + K^+ + \Lambda}$ for the p + K^++ Λ production(given in MeV) and the amount of statistics are shown. For this work, which focus on the description of $N\Sigma$ cusp effect, the data sample from COSY-TOF at an energy of 2.16 GeV and the data samples form DISTO at 2.14 GeV, 2.5 GeV, and 2.85 GeV were used.

2.2 DISTO

2.2.1 Experimental Setup

The DISTO experiment is a fixed-target experiment of measurement of pp collision for beam energy between 1.6 GeV and 2.85 GeV on SATURNE Accelerator in Saclay, France. The beam intensity has been limited to 1.0 x 10^8 protons/spill. Beam polarizations $\geq$ 70% were available at all the bombarding energies used. [5] A schematic view of the overall layout with typical detected particle tracks is shown in Figure 2.1. The polarized proton beam from the Saturne synchrotron is incident on a liquid hydrogen target placed at the center of a large-gap dipole magnet with a cylindrically symmetric vertical field [5].

Charged products are tracked through position-sensing chambers placed to both sides of the curving beam path. This allows for a good acceptance for small polar angles. Scintillating fiber arrays placed inside the magnet provide track coordinates essential for reconstructing the reaction and decay vertices, which are significantly separated for hyperon production events, as well as fast particle multiplicity information, used for defining a hardware trigger. Multi-wire proportional chambers (MWPCs) located beyond the magnet pole tips measure

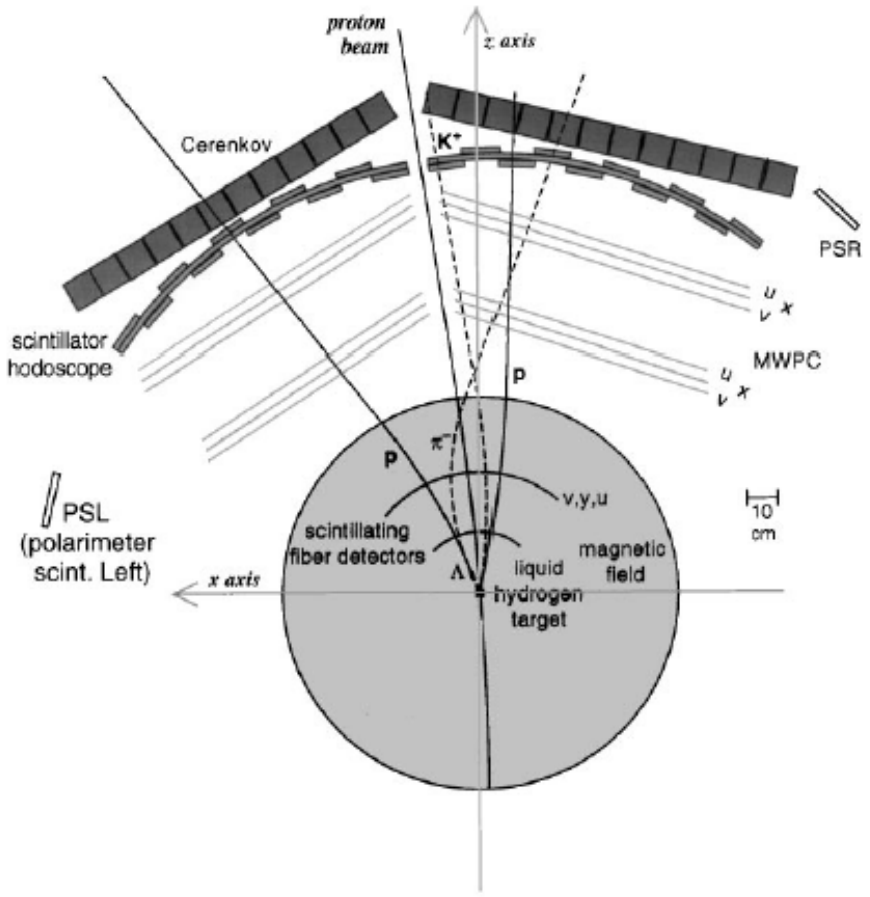

Figure 2.1: Schematic layout of the DISTO experimental apparatus, viewed from above, including simulated trajectories from a pp $\rightarrow$p + K^++ Λ event. The large shaded circle represents the effective field region. PSR and PSL are the two slabs to detect backward scattered protons in the polarimeter.

the exiting particle directions needed for momentum determination. A plastic scintillator hodoscope following the MWPCs also measures charged particle multiplicity for triggering purposes, and provides pulse height and timing information relevant to particle identification for each track. Further particle identification is obtained from the water Cherenkov counter hodoscope at the rear of each detector arm. [5]

All these detectors span a poler angular range in the laboratory frame from a few to to $\approx 48^\circ$ horizontally and $\approx 15.5^\circ$ vertically. Extra plastic scintillating slabs are placed at large angles on each detector arm, beyond the acceptance of the tracking detectors, to aid in coincidence detection of pp elastic scattering events used to monitor the beam polarization. [5]

2.2.2 Events Reconstruction

The DISTO collaboration has its own algorithm [5] like HYP code which succeeds in reconstructing four charged tracks from two displaced vertices and optimizing the reconstruction efficiency for hyperon production pKΛ events. Particle identification can be deduced from the correlation of Cherenkov and/or hodoscope pulse height with the reconstructed particle momentum. The correlations observed for tracks of positive curvature are shown in Figure 2.2. Intense and reasonably separated π^+ and proton groups are seen in the raw data for both Cherenkov and hodoscope counters.The K^+ band falls in the middle, and is revealed clearly only by the addition of conditions on other observables, e.g., by requiring that the event contain proton and π^- tracks characterized by an invariant mass consistent with the mass of the Λ . While the p, K and π groups are not fully resolved in Figure 2.2, unambiguous particle assignments can be made in the vast majority of events by utilizing pulse height information from both Cherenkov and hodoscope detectors, hodoscope time differences among tracks, and kinematic constraints. [5]

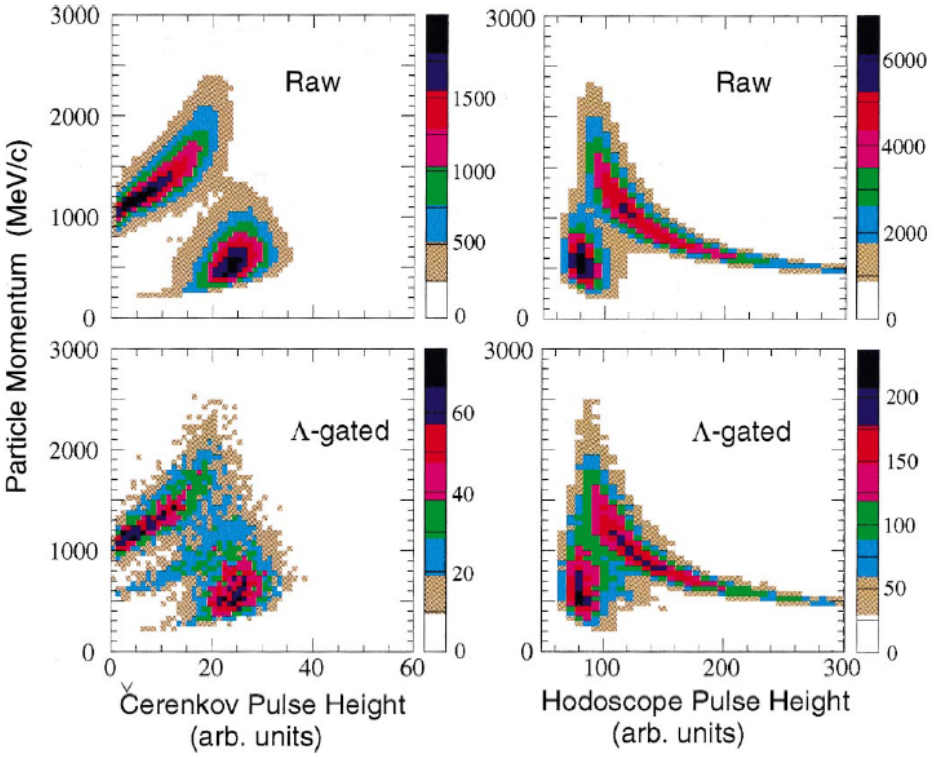

Figure 2.2: Correlations observed between the momentum reconstructed from fits to positive-curvature tracks emerging from the reaction vertex and the corresponding pulse height recorded in the Cherenkov or hodoscope counters. Data from all counters are included in these histograms. The raw spectra in the upper frames are dominated by distinct proton and π^+ groups. A K^+ group of comparable intensity to the others can be seen in the lower frames, after requiring that the tracks from the other vertex give an invariant mass consistent with Λ decay. [5].

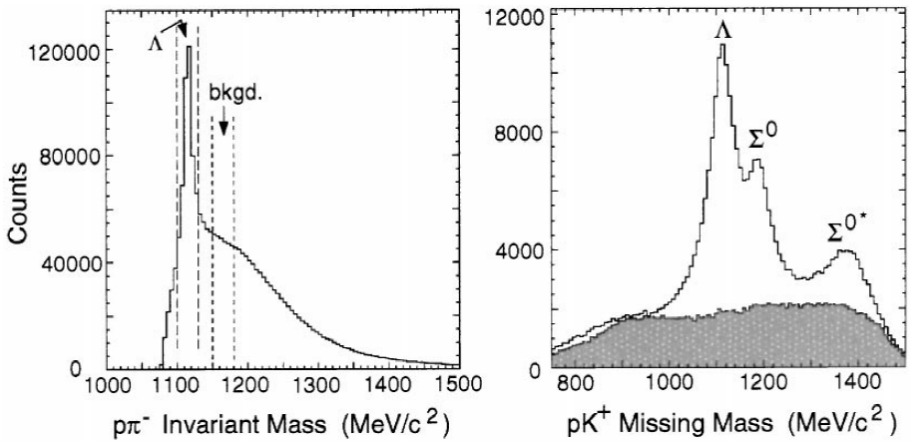

Figure 2.3: Spectra of invariant and missing mass reconstructed, respectively, from the decay daughters and from the reaction products for multi-particle events that pass loose conditions designed to emphasize hyperon production. The missing mass spectra include events which fall within the Λ invariant mass gate shown, or (shaded portion) within the background gate of equal width. [5].

The resolutions obtained in invariant and missing mass reconstructions are illustrated by the spectra for pKY candidate events in Figure 2.3. At the vertex reconstructed from p and π^- tracks, we see the Λ invariant mass peak clearly, with a resolution $\sigma \simeq 5Mev/c^2$. The background in this spectrum arises predominantly from abundant multiple pion ($\pi^+\pi^-$,$\pi^+\pi^0\pi^-$) production processes. Also shown in Figure 2.3 is the spectrum of missing mass reconstructed from p and K^+ tracks, for events falling within either the Λ or the background gates indicated in the invariant mass spectrum. When the background is subtracted, the resulting missing mass spectrum shows very clear peaks corresponding to the direct production of Λ (1116), Σ^0 (1192) and Σ^*(1385). Events between the $\Sigma$and Σ^* peaks are presumably due to continuum pp $\rightarrow$p$K^+\Lambda\ \pi^0$ reactions. [5]

The second frame of Figure 2.4 compares measured and simulated Λ decay distributions relevant to the determination of the Λ 's polarization component along a quantization axis normal to the production plane of the Λ .The relevant variable is the cosine of the daughter proton's emission angle with respect to this quantization axis, deduced in the Λ rest frame. The simulations are based on unpolarized Λ , and they show a symmetric, though not quite isotropic, coverage of the decay phase space. The measured $cos\theta^*$ distribution agrees well with the simulations. [5]

In the case of the p+p$\rightarrow$p + K^++ Λ reaction, a sample $\approx 10^5$ events was acquired at each of bombarding energies. The results obtained will provide a wealth of new information to constrain the mechanism for various exclusive nucleon nucleon reaction channels, especially those involving the production of open or hidden strangeness.

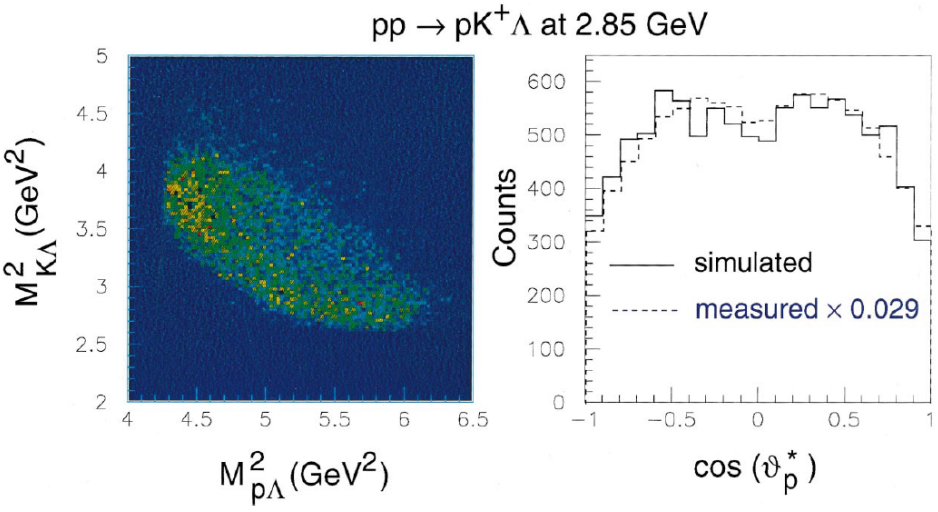

Figure 2.4: Distributions indicating the phase space acceptance of the DISTO spectrometer for exclusive p+p→p + K^++ Λ events at 2.85GeV bombarding energy. On the left is the Dalitz plot for events simulated assuming uniform phase space density, when those events are successfully reconstructed. The events falling beyond the kinematically allowed ellipse result from misidentifications in the event reconstruction. The right-hand frame shows simulated and measured distributions with respect to the daughter proton emission angle within the Λ rest frame. The simulations assumed unpolarized Λ production. It has been scaled by a factor 0.029 to permit direct comparison with the simulation. [5].

2.2.3 Phase Space Comparison

Before fitting the experimental data samples with the BG-PWA, they are compared to the phase-space simulation data.

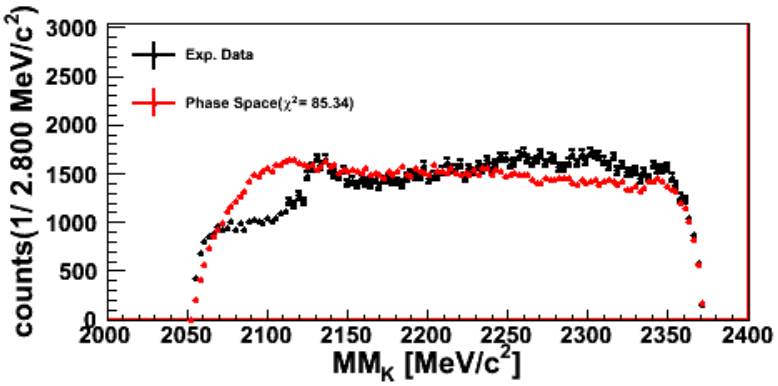

Figure 2.5: Comparison of experimental data (black dots) from the data sample DISTO@2.5 GeV with phase space simulation (red dots). [35]

The resulting spectra are shown in Figure above for DISTO data sample with 2.5GeV [23]. In the missing mass spectrum of K^+ , a peak structure $\approx 2.13 GeV/c^2$ is visible for this dataset. One can see in the figure, the pure phase space simulation (red lines) of p+p→p + K^++ Λ is not sufficient to describe the experimental data (black dots). Even though the non-fitting in the mass region of cusp region is expected, the remaining parts of the spectrum also show discrepancies. There are more plots of phase space comparison of other observables for DISTO@2.5 GeV data sample in Appendix A.b including the missing mass spectra of proton and Λ and various angular distributions in dependence of the CMS angles, the Helicity angles, and the Gottfried-Jackson angles Framework. Due to non-good fitting in these spectra, PWA does not give sufficient description for the experimental data.

2.3 COSY-TOF

2.3.1 Experimental Setup

The COSY-TOF experiment is a fixed target experiment using non-magnetic spectrometer, which is situated at an external beam-line of the accelerator COSY in the research center Juelich. COSY is an oval synchrotron of about 180 m circumference where protons can be accelerated from $0.27 GeV/c$ to $3.7 GeV/c$. The proton beam is characterised by a good momentum precision of $\Delta p/p < 10^{-3}$ and a small emittance. [36]

H^- ions are accelerated up to 40MeV in the cyclotron and then injected into the beamline. At the injection, the negative ions go through a stripfoil that separates the electrons from the protons. Protons are accelerated in the oval ring where bending and focussing magnets

are continously adapted to the beam energy(synchrotron method). A maximum of 2×10^{11} protons are stored in the ring. In the case of a polarised beam, protons with a polarisation of up to 80%-85% can be stored in the synchrotron. For the external experiment COSY-TOF, protons are extracted with a stochastic method capable of extracting the beam slowly over a long period of time in spills of 10^7 to 10^{11} particles/s. The spin is flipped at every spill to minimize any time-dependent asymmetries. [36]

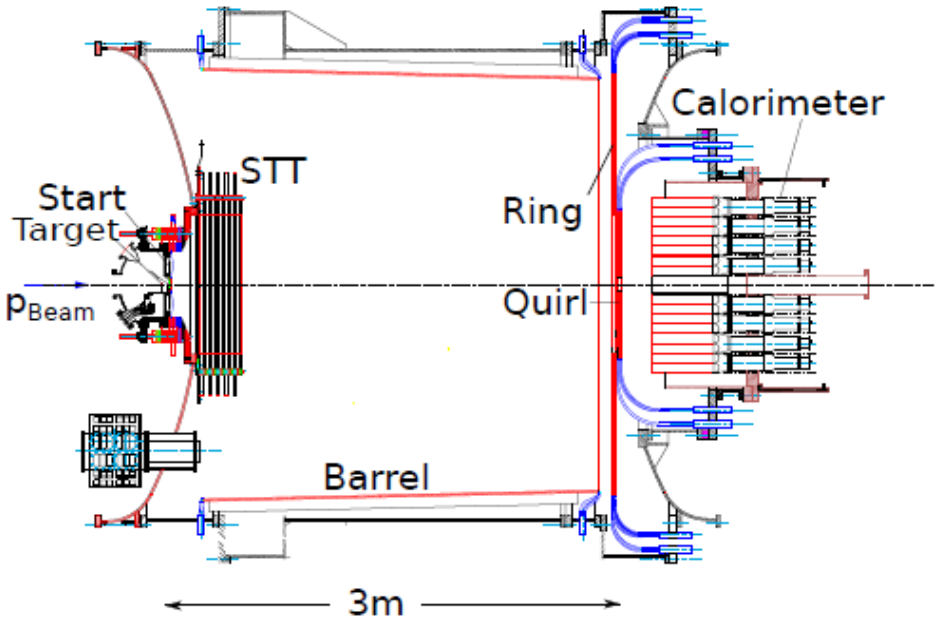

Figure 2.6: Side view of the COSY-TOF spectrometer. In beam direction the start counter (Start), the straw tube tracker (STT), the barrel scintillators, the inner ring (Quirl), the outer ring (Ring), and the Calorimeter are shown. All detectors and the liquid hydrogen target are located inside the vacuum vessel [9].

In Figure 2.6, the start detector system was expressly designed to have a good geometric track reconstruction; the Barrel and the Endcap detectors allow the time-of-flight measurements. The tank is evacuated in order to minimize secondary scattering reactions. COSY-TOF is a $''4\pi$ detector$''$ for all the hyperon production reactions. Even at the maximum beam momentum reached by the COSY accelerator, the total energy is only few hundred MeV above the production threshold; therefore the particles have small transverse momenta and are scattered mainly in the forward direction. [36]

The main detector system is the central straw tube tracker (STT). The STT is placed about 24 cm behind the target inside the vacuum tank. It is fixed in six orientations with an angle of 60° to each other in order to enable 3D track reconstruction. The arrangement of the target and detectors facilitates a volume in the z-direction from the target to the beginning of the straw detector, which is free of any material apart from the start counter and silicon counter. Therefore, a secondary vertex in this volume indicates with highest probability a Λ or a K^o_S

decay. [9] The Stop Detector has also modular design and consists of Quirl, Ring and Barrel. Quirl and Ring together are also referred to as the Endcap. Quirl and Ring together cover continuously the angular rangefrom 0.7° to 24.8°. The Barrel covers an angular range from 24.8° to 76.7°, but in the present configuration the angles larger than 70° are shielded by a steel flange that holds the start detector system. [36]

The trigger is defined by signals of the start counter, the barrel scintillators and the end-cap scintillators. Only when the ADC and TDC signals satisfy certain trigger conditions are the data stored on tapes. In p+p→p + K^++ Λ at least one signal of the start counter and at least 4 hits in the barrel and end-cap are required. Effects that reduce the multiplicity can be: inefficient detector zones, like aluminium cladding; inefficiencies of the detector itself; or particles absorbed in a detector layer. The fact that, near threshold, particles may fly at small angles through the beam hole of the detectors also reduces the multiplicity. [9]

2.3.2 Events Reconstruction

Because of the high granularity of the start detector system, the p+p→p + K^++ Λ events can be fully reconstructed with sufficient precision using only the geometrical information from the hit pattern in the various detector components.For reactions such as p+p→p + K^++ Λ , a secondary vertex also has to be reconstructed. Tracks are reconstructed using different methods for primary and secondary tracks [36]. The event reconstruction starts with a Hough transformation for two dimensional track finding in each of the three STT orientations. Events with 4 reconstructed tracks are selected. These are checked and optimized to match the pKΛ event geometry. [37] For the maximum possible reconstruction precision, a kinematic fit is performed that optimizes the event kinematics with respect to the residuals of the STT's track to wire distances.

This is depicted in Figure 2.7 left. For all events, a longer Λ flight path than 1 cm (black), the event selectio (blue) and also the difference (red) are shown. A minimum of 3 cm flight path in the laboratory system to the secondary vertex is chosen as a threshold. [37] To test the event selection we calculate the four-momenta of p, K and Λ from the initial state four momentum, the reconstructed track directions and momentum conservation. The resulting missing energy is given in Figure 2.7 on the right. All events with a converged kinematic fit and a hyperon flight path longer than 1 cm are shown in black. The above mentioned selection criteria leave the events shown in blue in the event sample. The difference is shown in red. [37]

The Dalitz plot of the selected events not yet corrected for reconstruction efficiency is shown in Figure 2.8 on the left. One sees that the detector has full kinematical acceptance and that the high resolution reveals several structures. In $m^2_{p\Lambda}$ there is a clear cusp at the pΣ^0threshold. The exact peak position and peak shape that will be subject to further studies of the corresponding coupled channel effect. In the projection on $m_{K\Lambda}$ on the bottom right we also find indications for a cusp structure at the KΣ^0threshold. The underlying structure of the Dalitz plot can be explained by final state interactions and N^* resonances. [37]

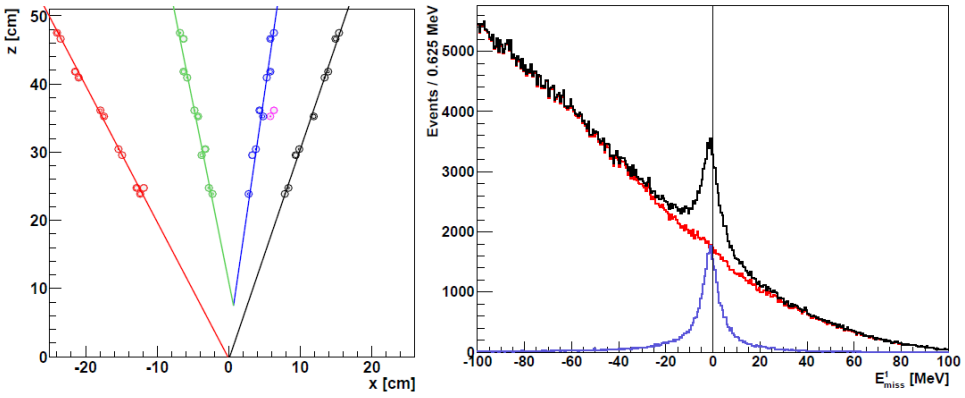

Figure 2.7: Left: An event display of one of three STT orientations. The large circles mark the straw outer diameter and the smaller inner circles mark the measured track to wire distances. Right: The missing energy in the primary vertex before the kinematic fit. [37].

2.3.3 Phase Space Comparison

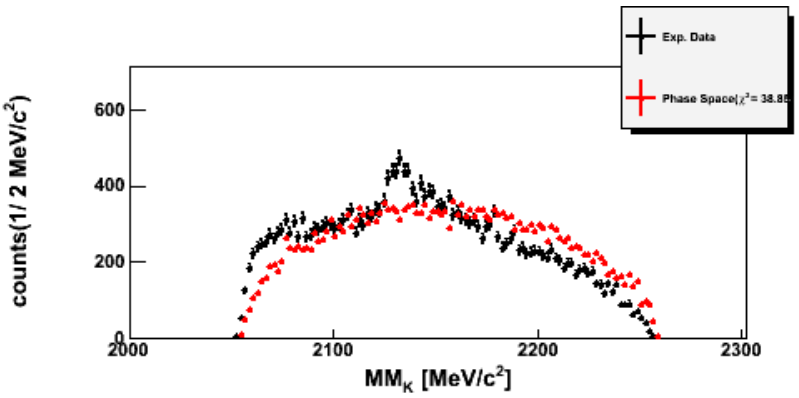

Figure 2.9: Comparison of experimental data (black dots) from the data sample COSY-TOF@2.16 GeV with phase space simulation (red dots). [35]

Also for the COSY-TOF dataset, in the first step the experimental and phase space simulation data sample were directly compare before the BG-PWA fitting procedure. The resulting spectra are shown in Figure 2.9. In the figure, the pure phase space simulation (red lines) of p+p→p + K^++ Λ is also not sufficient to describe the experimental data (black dots). In the missing mass spectrum of K^+ , there is also a peak structure $\approx 2.13 GeV/c^2$ clearly visible for this dataset. This peak is not well described by the phase space simulation(red line), also some other remaining spectrum. Since these fittings fail to describe the experimental data, they give a hint for necessity of BG-PWA analysis. The description of BG-PWA Framwork is shown in Section 3.1. There are more plots of phase space comparison of other observables for DISTO@2.5 GeV data sample in Appendix A.c including the missing mass spectra of proton and Λ and various angular distributions in dependence of the CMS angles, the Helicity angles,

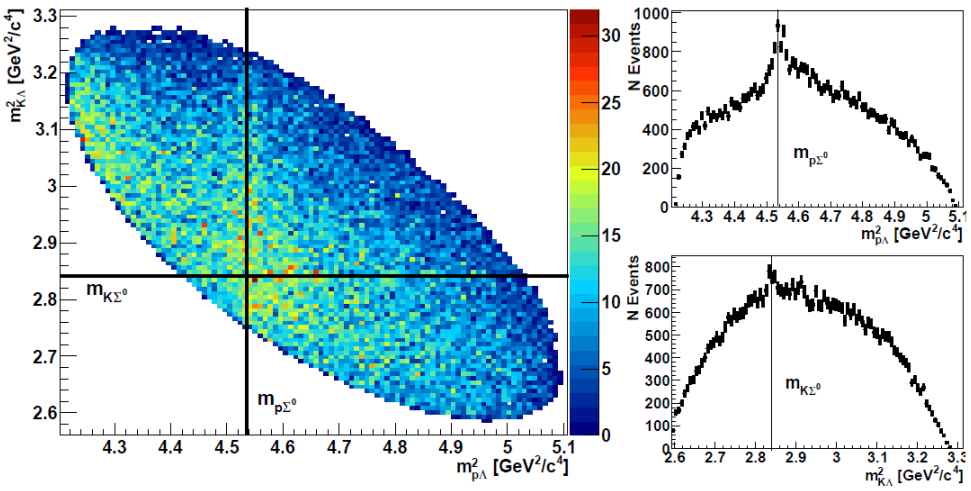

Figure 2.8: The dalitz plot (left). The lines mark the pΣ^0 and KΣ^0 thresholds, respectively. The projections on $m^2_{K\Lambda}$ (top) and $m^2_{p\Lambda}$ (bottom) are also shown on the right. [37].

and the Gottfried-Jackson angles Framework. Due to non-good fitting in these spectra, PWA does not give sufficient description for the experimental data.

Chapter III

The BG-PWA Framework

3.1 Bonn-Gatchina Model

3.1.1 Theoretical Background

The transition waves between the initial state $|i\rangle$ and final state $|f_k\rangle$ in a scattering process have amplitudes $A_{k,n}$, which is developed as following: [30]

$$A_{k,n} := \langle f_k | T_n | i \rangle = \sum_{\alpha,\beta} \langle f_k | \beta \rangle \langle \beta | T_n | \alpha \rangle \langle \alpha | i \rangle = \sum_{\alpha,\beta} Y^{f_k} A_n^{\alpha,\beta} Y^i. \tag{3.1}$$

The indice n represents each production channel of the reaction. The known eigenstates $|\alpha\rangle$ and $|\beta\rangle$ of rotating angular operators together with transion matrix T_n stand for the amplitudes of partial waves $A_n^{\alpha,\beta} := \langle \beta | T_n | \alpha \rangle$. The factor $|A_n|^2$ represents the intensity of the transition $|i,\alpha\rangle \rightarrow |f_k,\beta\rangle$ for n production channel. Here $\alpha = (J,L,S)$ are the quantum numbers of initial states and β are quantum numbers of final states. Y^{f_k} and Y^i could be calculated with the known four momentum initial state $|i\rangle$ and final state $|f_k\rangle$ together wtih the known four momentum eigenstates $|\alpha\rangle$ and $|\beta\rangle$ of corresponding angular operators.

3.1.2 Parametrizations of Cross Sections

The Bonn-Gatchina Partial Wave Analysis (BG-PWA) Framework is a program of a partial wave analysis for data from Baryon-Baryon collision [30]. Here it is used to describe the different channels of reaction p+p→p + K^++ Λ . In the BG-PWA the production differential cross section of final state including three particles with single particle four-momenta $q_{1,2,3}$ is parametrized as in Equation 3.2 [3]

$$d\sigma = \frac{(2\pi)^4 |A|^2}{4|\vec{k}|\sqrt{s}} \mathrm{d}\Phi_3 \left(P, q_1, q_2, q_3\right). \tag{3.2}$$

wherein $\vec{\mathrm{k}}$ is the combined 3-momentum of the initial particles, $\sqrt{s}$ is the center of mass energy of the reaction, $d\Phi_3$ is infinitesimal phase space volume of the final state, which results from a kinematic analysis. A is the total transition amplitude of the considered reaction. The transitional matrix element A is the sum over all trasition waves of one channel of the reaction: $A = \sum A_{k,n}$. The problem is reduced by the amplitudes of partial waves, on which the differential cross section depends, to determine.

To calculate the differential cross section, the amplitudes of partial waves need to be parametrized. For each partial wave, the final state is treated as a two particle system with quantum numbers (S', L', J), thus the quanten number for total system pKΛ is denoted by (S', L', J). One of these two particle system is again a two particles subsystem with quantum numbers (S_2, L_2, J_2). Thus the quantum numbers of final state is $\beta = (S_2, L_2, J_2, S', L', J)$ [30]. The individual channel of p + K^++ Λ production differs only in the corresponding partial waves. BG-PWA parameterized the partial amplitudes generally as follows Equation 3.3:

$$A = \sum_{\alpha} A_{\mathrm{tr}}^{\alpha}(s) Q_{\mu_1..\mu_j}^{\mathrm{in}}(S,L,J) A_{2b}\left(i, S_2, L_2, J_2\right) Q_{\mu_1..\mu_j}^{\mathrm{fin}}(i, S_2, L_2, J_2, S', L', J). \tag{3.3}$$

In Equation 3.3, the factors Q^{in} and Q^{fin} parametrize part of amplitudes of partial waves. These two factors are dependent on the quantum number α of initial state and β of the final state [3]. For all channels they are the same functions but with different allowed quantum numbers α and β in the respective channels. The $A^{\alpha}_{\text{tr}}(s)$ is parametrized in Equation 3.4 [30]:

$$A^{\alpha}_{\text{tr}}(s) = (a^{\alpha}_1 + a^{\alpha}_3)\exp(\mathrm{i}a^{\alpha}_2) \tag{3.4}$$

In Equation 3.4, $A^{\alpha}_{\text{tr}}(s)$ is parametrized by a constant amplitude a^{α}_1, an energy dependent amplitude a^{α}_3 and a phase a^{α}_2. For one beam energy, a^{α}_3 can be set to zero. The $A_{2b}\left(i, S_2, L_2, J_2\right)$ must be selected however for the respective channels with different function parameters. In Section 3.1.2.1 and Section 3.1.2.2 are shown two ways of factor parametrization for $A_{2b}\left(i, S_2, L_2, J_2\right)$ in two particles subsystem pΛ and N^* resonances.
The possible combinations of angular momentum quantum numbers of the initial two proton state $\left(J^P = \frac{1}{2}^-\right)$ are shown in Table 3.1.

J^P	$S_{tot} = 0$	$S_{tot} = 1$
L=0	0^+	1^+
L=1	1^-	$0^-, 1^-, 2^-$
L=2	2^+	$1^+, 2^+, 3^+$
L=3	3^-	$2^-, 3^-, 4^-$

Table 3.1: Possible combinations of the initial system of two proton. The grey shaded combination are forbidden. [30]

However, since the two initial protons are indistinguishable fermions, the total wave function of both particles has to be anti-symmetric which is equivalent to the following condition:

$$(-1)^{L+S+1} = -1. \tag{3.5}$$

Iin Table 3.1 shows all possible combinations of the spin (S), orbital angular momentum (L), and total angular momentum (J) for initial system of two proton. The grey shaded combination are forbidden. Furthermore, the orbital angular momentum is L$<$4, limiting the partial waves to F-wave, which also simply the analysis. [30]

3.1.2.1 Non-Resonant p+p→p + K^++ Λ Production

In the case of non-resonant p+p→p + K^++ Λ production, proton and Λ form a two particle subsystem with the quantum numbers (J_2, L_2, S_2) in Equation 3.3. The re-scattering of proton and Λ are described by modified effective range parametrization of the factor $A^{\beta}_{2b}(S_2, L_2, J_2)$ [30]:

$$A^{\beta}_{2b} = \frac{\sqrt{s_i}}{1 - \frac{1}{2}r^{\beta}q^2 a^{\beta}_{p\Lambda} + \mathrm{i}q a^{\beta}_{p\Lambda}\, q^{2L}/F\left(q, r^{\beta}, L\right)} \tag{3.6}$$

where q is the relative momentum between the baryons in the two particle subsystem and multi index β denotes possible combinations of channels i and quantum numbers S_2, L_2 and J_2. $a^{\beta}_{p\Lambda}$ is the pΛ-scattering length and r^{β} is the effective range of the Λ -p system. F(q,r,L) is the Blatt-Weisskopf factor, which is used for normalization[1].

3.1.2.2 pp $\rightarrow N^*$ $\rightarrow$p + K^++ Λ Production

In case of resonant p+p$\rightarrow$p + K^++ Λ production, the two decay particles are proton and N^* resonance, where N^* resonance decays into KΛ . The BG-PWA takes the N^* as eigen subsystem and KΛ system is treated with intrinsic quanten number (J_2, L_2, S_2) from N^* resonance. To describe A_{2b} of N^* resonances, the relativistic Breit-Wigner formula used in A_{2b} factor is shown in Equation 3.7 [30]:

$$A^{\beta}_{2b} = \frac{1}{(M^2 - s - \mathrm{i}\Gamma M)}, \tag{3.7}$$

with pole mass M and the width Γ of the corresponding resonance. Besides, the masses and widths of the N^* resonances, which has to be provided into BG-PWA are listed in Table 3.2.

Resonance	J^P	Mass (GeV/c^2)	Width (GeV/c^2)	$\Gamma_{K^+\Lambda}/\Gamma_{tot}$ (%)
$N^*(1650)$	$\frac{1}{2}^-$	1.655	0.150	3-11
$N^*(1710)$	$\frac{1}{2}^+$	1.710	0.100	5-25
$N^*(1720)$	$\frac{3}{2}^+$	1.720	0.250	1-15
$N^*(1875)$	$\frac{3}{2}^-$	1.875	0.220	4±2
$N^*(1880)$	$\frac{1}{2}^+$	1.870	0.235	2±1
$N^*(1895)$	$\frac{1}{2}^-$	1.895	0.090	18±5
$N^*(1900)$	$\frac{3}{2}^+$	1.900	0.250	0-10

Table 3.2: N^* resonances included in the Partial Wave Analysis written in the spectroscopic notation with their the mass and the width, taken form [7].

3.1.3 Cusp in BG-PWA

In case of cusp, the two particles in the final state are formed by a K^+ and a Cusp-quasi particle. The parametrization of A_{2b} factor in Equation 3.3 for the cusp-quasi particle is done by a Breit-Wigner or Flatté distributions. A first attempt was performed using relativistic Breit-Wigner parametrization, since the structure seems symmetric. Even though the description of the cusp by relativistic Breit-Wigner parametrizatiooes does not spares a physical motivation, it provides a sufficient check, whether the BG-PWA fitting converges for the experimental data. Flatté parametrization is later implemented, providing more information which may contribute as experimental evidence for theoretical interpretation of NΣ cusp formation.

[1] The Blatt-Weisskopf factor is 1 for $L = 0$ and the explicit form for other partial waves can be found in [3]

Also, additional partial waves - each corresponding to a possible angular momentum state of the NΣ cusp structure - are added to the BG-PWA. Since production via these channels happen directly at threshold the Σ and N are expected to be in a relative s-wave state, which means the spin-parity of the NΣ system is either $J^P = 0^+$ or $J^P = 1^+$. The resulting pΛ system then may appear in an s-wave state in case of $J^P = 0^+$ or in an s- or d-wave state in case of $J^P = 1^+$.

3.1.4 Analysis Method of BG-PWA

As BG-PWA input, it needs measured experimental data. Additionally, a set of phase-space simulation data - filtered for acceptance and efficiency - of the channel p + K^++ Λ has to be provided. Thus the fitting analysis is done just within the acceptance of the corresponding detector system.

The BG-PWA requires proper input values for the fitting procedure, which have to be given. They are the values for the amplitude parametization $a_{1,2,3}$ in Equation 3.4, the mass and width of the N^* resonaces (given in Table 3.2) and the parameters defining the cusp (threshold mass M and coupling strengths for pΛ and NΣ). For NΣ Cusp, the initial threshold mass is set as 2.13 GeV/c^2 and the initial values of two coupling constants are free to set any values.

In the fitting procedure of BG-PWA, the values for the free parameters are determined by the Maximum-LogLikelihood method as best as possible to reproduce experimental cross section. These mass and parameterset for individual partial wave are fitted on an event-by-event base to the experimental data. For each fitting step the total sum of all participating waves is built according to the previously described parametrization. This total sum is weighted with the simulation data sample, to correct for the acceptance and efficiency of the detector. Due to the phase factor in the amplitude parametrization, interference between different transitions of same quantum numbers (J^P) can occur. The program changes the non-fixed values of mass and parameterset step by step to maximize the logarithmic Lokelihood-Function. The obtained loglikelihood value is not suited to tell about the absolut quality of the results, but only be used to compare fitting results of the same dataset.

To quantify the agreement between different simulation models and the experimental data, a χ^2 value can be defined by Equation 3.8 [30].

$$\chi^2 = \sum_{Observables} \sum_{Bins} \frac{(s_{sim} - s_{exp})^2}{{\sigma_{sim}}^2 + {\sigma_{exp}}^2}, \tag{3.8}$$

counts$_{sim}$ and counts$_{exp}$ are the entries of one bin of the histogram of the simulation data and experimental data, respectively. The error value of simulation and experimental data are given by σ_{sim} andσ_{exp}. The sum runs over all bins of the nine histograms of the observables. [30]

To extrapolate the results to the 4π full phase space, additional data samples can be added to PWA fitting procedure. These data samples contains only simulation events, which are not filtered for acceptance and efficiency and represent the isotropic production in the full phase

space for different beam energies. Since theses data samples do not contain experimental events, they do not influence the results of the fitting routine.

A major limitation of the BG-PWA is the uniqueness of the solution. The method is designed that is a local minimum of log-likelihood value found, it is not ensured that the result really represents the best parameters. Furthermore, the solution of PWA also depends on the chosen initial values of the free parameters. It must be checked how stable the solution is under varying the starting values of parameters. These can be checked by a systematic scan under exclusion of one or more resonant production channels, which are 2^n possibilites. In this way, it can be checked whether the full solution is stable under altering choices of initial parameter values through comparison of the 5 best results obtained in the scan. Also, an estimate of the systematical uncertainties can be given using difference of the relative contributions of partial waves in these five best results.

3.1.5 Results - PWA Output

The results of BG-PWA is essentially having a local maximum in the Likelihood Function by parameters modification. Using this method with Montecarlo-Simulation, the main output of the BG-PWA is a list of simulated events, which have been used for the simulation input of the PWA. Each event is assigned with a weighting factor, which gives the contribution of this event to the total yield. From these output events, the differential spectra for the observables are filled event by event scaled by the weighting factor. After PWA, the simulation results are compared with the experimental data.

Beside the weighted data, a list of all included transition waves is also written out with its corresponding relative production contribution. It also allows to extract the relative contribution of a production channel. Besides, the PWA output provides a new parameter list file in the same format like the input parameterset, which contains the resulting fitting values for each parameters. [35]

3.2 PWA without Cusp Channel

As a crosscheck, a fit without the cusp waves was performed for the DISTO@2.5 GeV to ensure that the peak structure could not be described by other channels alone [35]. For this cross check, a BG-PWA was performed including all channels but those for the NΣ Cusp. In the Figure 3.1, the cusp, which is visible in the data, can not be described, while other parts in the K^+ missing mass spectrum are sufficiently described. This means that the cusp can not be explained yet, which was to be expected, as no partial waves parametrizing the cusp in any way in the analysis. Fora description of the peak structure, additional waves, representing the NΣ cusp, are required. In the plots, the PWA results are scaled to the experimental data, so the total integral is the same.

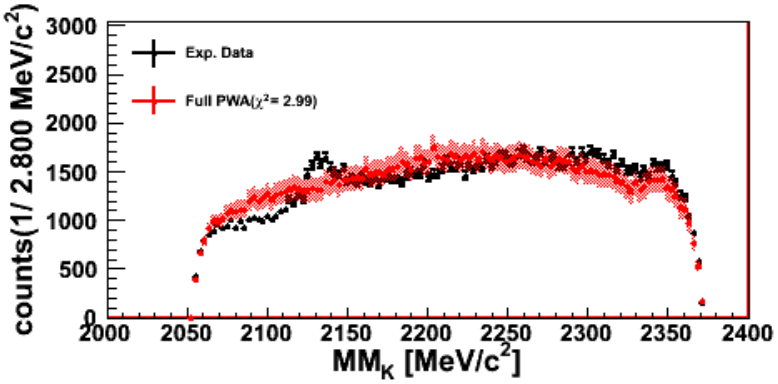

Figure 3.1: Comparison of experimental data (black dots) from the data sample DISTO@2.5 GeV with the results from the Partial Wave Analysis (red dots).. [35]

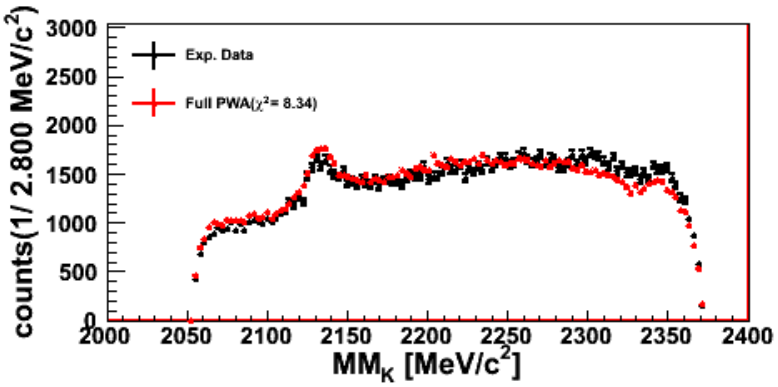

Figure 3.2: Comparison of experimental data (black dots) from the data sample DISTO@2.5 GeV with the results from the Partial Wave Analysis (red dots) in the missing K^+ mass spectrum.The fitting error of PWA is given by the red band. . [35]

3.3 PWA with Breit-Wigner

As described in the Section 3.2, the cusp can not be described without additional waves. The cusp waves are added as other partial waves with amplitudes parametrized by relativistic Breit-Wigner formula in Equation 3.7, since the structure seems symmetric. In accordance with the method described in Section 3.1.3, a total of three additional partial waves each corresponding to a possible angular momentum state $(J^p, L) = (0^+, 0)$, $(J^p, L) = (1^+, 0)$, $(J^p, L) = (1^+, 2)$ for cusp are added to the BG-PWA. The pole mass M is equal to NΣ threshold 2130 MeV/c^2 and the width $\Gamma =$ 20 MeV/c^2. [23].

In Figure 3.2, the BG-PWA result for the DISTO@2.5 GeV sample with a Breit-Wigner parametrization of the cusp-structure is shown in the K^+ missing mass spectra. A total results including all missing mass spectra as well as the various angular distributions in de-

parameter set	A	B	C	D	E
log likelihood	-25365	-25338	-25308	-25247	-25200
$pp \to pK\Lambda$ (direct)	$4,73\%$	$9,98\%$	$11,75\%$	$7,26\%$	$12,93\%$
$pp \to N^* \to pK\Lambda$ (1650)	$7,31\%$	$6,46\%$	$12,24\%$	$9,51\%$	$7,33\%$
$pp \to N^* \to pK\Lambda$ (1710)	$28,86\%$	$23,20\%$	$30,93\%$	$25,50\%$	$19,42\%$
$pp \to N^* \to pK\Lambda$ (1720)	$4,93\%$	$5,55\%$	$5,63\%$	$6,08\%$	0%
$pp \to N^* \to pK\Lambda$ (1875)	$0,21\%$	0%	$0,12\%$	0%	$0,33\%$
$pp \to N^* \to pK\Lambda$ (1880)	$16,43\%$	$15,87\%$	$14,18\%$	$18,23\%$	$9,78\%$
$pp \to N^* \to pK\Lambda$ (1895)	$26,73\%$	$26,98\%$	$11,71\%$	$25,32\%$	$42,56\%$
$pp \to N^* \to pK\Lambda$ (1900)	$0,41\%$	$0,26\%$	0%	0%	0%
$pp \to pK\Sigma \to pK\Lambda$ (S_0^+-Cusp)	$7,65\%$	$7,91\%$	$8,41\%$	$3,69\%$	$5,80\%$
$pp \to pK\Sigma \to pK\Lambda$ (S_1^+-Cusp)	$1,71\%$	$3,00\%$	$2,38\%$	$2,94\%$	$0,61\%$
$pp \to pK\Sigma \to pK\Lambda$ (D_1^+-Cusp)	$0,51\%$	$0,53\%$	$0,68\%$	$0,50\%$	$0,82\%$

Table 3.3: Relative contributions of the different channels according the five best bg-pwa results. A is the full parameter set, in B the $N^*(1875)$ is not included, in C the N^* (1900) is not included, in D both are not included, and in E also the N^* (1720) is not included [23]

pendence of the CMS angles, the Helicity angles, and the Gottfried-Jackson angles are shown in Section A.d. The result sufficiently describes the K^+ missing mass spectra, especially all three cusp waves with their eigen quanten number are added to describe the cusp.

The five best results of the systematical scan are shown in Table 3.3 together with the corresponding log likelihood values [23]. One can see that the inclusion of the $N^*(1720)$, $N^*(1875)$, and $N^*(1900)$ resonances does not strongly alter the quality of the result, which means that these three resonances are not necessary for describing the data set. Furthermore, all five solutions contain significant contributions of the $N^*(1710)$, $N^*(1880)$, and $N^*(1895)$ resonances, which indicates that these N^* resonances may be necessary for the description of the p + K^++ Λ production at the beam energy [23].

Chapter IV

Results and Discussions

4.1 Single Data Analysis

The main work of this chapter is focused on describing the analysis of single dataset. It is the simplest case that only one dataset is processed at one time by PWA.

As mentioned in the former chapters, the NΣ cusp phenomenon can be described by relativistic Breit-Wigner distribution, but it gives no more information to comprehend the formation of cusp. Flatté parametrization, however, treats the cusp as interplay of two coupled channels for pΛ and NΣ and the coupling constant for each production channel together with the threshold mass may provide a physical explanation for formation of cusp.

To implement the Flatté parametrization instead of the relativistic Breit-Wigner distribution, the two coupling constants for pΛ and N$\Sigma$are treated as free parameters, as they are unknown values from theoretical interpretation. Besides, the threshold mass, which is also unknown from theoretical interpretation, is also treated as a free parameter which could be adapted to a new value in the analysis procedure. The starting value for threshold mass is 2.13 GeV according to the analysis of Breit-Wigner distribution. The starting values for two coupling constants are set to 0.01, separately. These values are not from theoretical interpretation, but from experiences that it turns out workable in the beginning attempts.

The PWA analysis procedure is similar to the one, which is used for Breit-Wigner parametrization. The successful descriptions with the experimental results by Breit-Wigner parametrization for cusp in fact provide practical reference values of parametersets for further analysis by using Flatté parametrization. In the following analysis, the starting parameterset for the PWA is usually directly taken from analysis with Breit-Wigner distribution corresponding to different dataset.

After the data are well prepared and all parameters are set properly, the BG-PWA program is started. The quality of fitting can be extracted by the Loglikelihood-values. One can see if the results are converge by checking whether the Loglikelihood-values are positive or negative. In BG-PWA program, the results are getting better and better by modifying the parametersets and the Loglikelihood-values are getting more and more negative.

At the end of PWA analysis, the Loglikelihood-values cannot be more negative any more and a new parameterset is created, where one can check the final values of each parameter. To the interest of cusp phenomenon, the main values have to be checked, are values for coupling constants for pΛ and NΣ and the value of the threshold mass.

In the following subsections, it will show the PWA single data results for DISTO@2.5 GeV, DISTO@2.14 GeV and COSY-TOF@2.16 GeV, separately, including a comparison of the experiemtnal data and the PWA result. Furthermor from the PWA results, the relative strength of the contribution channels as well the spectra for an extrapolation to the full phase space are shown.

4.1.1 DISTO @2.5 GeV

4.1.1.1 Fitting Results

The first probes of Flatté parametrization are conducted on DISTO@2.5 GeV data sample, since there are nice PWA descriptions of this data sample with Breit-Wigner parametrization in Section 3.3. The basic setting of parameters obey the rules in the introduction part of this chapter.

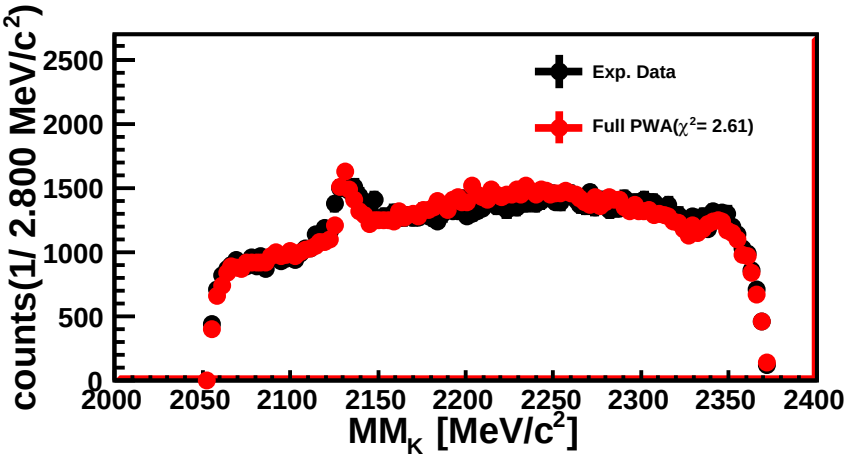

Figure 4.1: Comparison of experimental data (black dots) from the data sample DISTO@2.5 GeV with the results from the Partial Wave Analysis (red dots) in the missing K^+ mass spectrum.The fitting error of PWA is given by the red band.

The final PWA fitting result for the missing mass K^+ spectrum of DISTO@2.5 GeV is given in Figure 4.1. In these plots, the PWA analysis(red dots) results give a nice description to the experimental K^+ missing mass spectra(black dots). The PWA results are scaled to the experimental data points, by normalizing to the same value of the integral of all points. In the Appendix B.a.i, there are PWA plots not only for the K^+ missing mass spectra of DISTO@2.5 GeV data sample, but also for Λ and p missing mass spectrum as well as the various angular distributions in dependence of the CMS angles, the Helicity angles, and the Gottfried-Jackson angles shown. These plots also have to give sufficient descriptions for the experimental data, but minor discrepancies are allowed which is within the systematical error of the PWA procedure.

A significant peak shape in the K^+ missing mass spectrum around 2130 MeV/c^2, which is interpreted as cusp, is visible in the experimental data. In the plots, the cusp as well as the physical background below are all described by the PWA solution with minor discrepancies. Furthermore, the total log likelihood value and reduced χ^2 value Section 3.1.4 for this result are checked. The loglikelihood value is not suited to tell about the absolut quality of the results, but only is used to compare fit results of the same data set. In this case, the log likelihood-value is -15447.8 and χ^2 /ndf(ndf) is 2.61(766). The negative loglikelihood value means PWA process converges, a good fits is possible. The small χ^2 /ndf value indicates a

relatively good fits to the experimental data.

The main interest of the analysis are the cusp related values. For this dataset, the final coupling constants are $g_{N\Sigma} = 1 \times 10^{-6}$ and $g_{p\Lambda} = 4.818 \times 10^{-3}$. The final pole mass is $m_r = 2.1298$ GeV/c^2. The final coupling constant for NΣ is much smaller thant pΛ and the pole mass shifts from 2.13GeV by round 0.2 MeV/c^2. To test the stability of this result, the single data analysis with other dataset is further done.

4.1.1.2 4π-Plots

Besides, by adding 4π simulation data, the events can be extrapolated on the entire solid angle and the 4π extrapolation plotting (Section 3.1.4) can used to visualize the shapes of partial waves by BG-PWA.

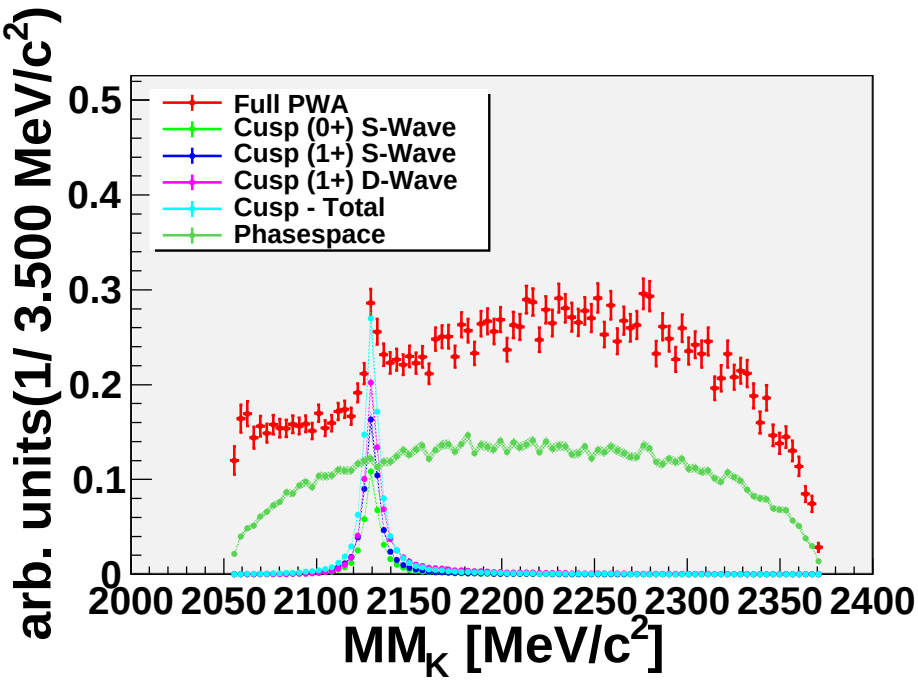

Figure 4.2: Full 4π phase space extrapolation plotting from the data sample DISTO@2.5 GeV in the missing K^+ mass spectrum. It shows Cusp($J^P = 0^+$) S-wave(light green dots), Cusp($J^P = 1^+$) S-wave(blue dots) and Cusp($J^P = 1^+$) D-wave(pink dots). The full PWA(red dots), total cusp waves(light blue dots) and the phase space(green dots) are also shown. The scales of the partial waves are arbitrary.

In the Figure 4.2, the phase-space distribution is given by the dark green curve. The three different posible cusp waves are given by light green (0^+ S-wave), blue (1^+ S-wave) and pink (1^+ D-Wave) dots. The coherent sum of all cusp waves is given by the light blue curve. It can be nicely seen, the shape of the different cups wave do not differ significant for each other and

shows as symmetric structure at NΣ threshold, which plays a major role in description of cusp.

4.1.1.3 Channel Contributions

The relative contributions of direct p + K^++ Λ production and N^* resonances are of great interest, to see which channels are produced at largely and which channels play minor roles.

Channels	Contributions
$pp \to pK\Lambda$ (direct)	$28.3 \pm 5.5\%$
$pp \to N^*(1650) + p \to p + K^+ + \Lambda$	$13.9 \pm 2.6\%$
$pp \to N^*(1710) + p \to p + K^+ + \Lambda$	$25.1 \pm 4.8\%$
$pp \to N^*(1720) + p \to p + K^+ + \Lambda$	$3.5 \pm 0.6\%$
$pp \to N^*(1875) + p \to p + K^+ + \Lambda$	$0.6 \pm 0\%$
$pp \to N^*(1880) + p \to p + K^+ + \Lambda$	$15.2 \pm 2.9\%$
$pp \to N^*(1895) + p \to p + K^+ + \Lambda$	$7.7 \pm 1.6\%$
$pp \to N^*(1900) + p \to p + K^+ + \Lambda$	$1.8 \pm 0.3\%$
$pp \to pK\Sigma \to pK\Lambda$ (S_0^+-Cusp)	$0.4 \pm 0\%$
$pp \to pK\Sigma \to pK\Lambda$ (S_1^+-Cusp)	$3.1 \pm 0.6\%$
$pp \to pK\Sigma \to pK\Lambda$ (D_1^+-Cusp)	$0.4 \pm 0\%$

Table 4.1: Relative contributions of the different channels according the BG-PWA results for DISTO@2.5 GeV. The error corresponds to the fitting error of the partial wave analysis.

In Table 4.1, the realtive strength of all contribution channels are listed with the fitting error, obtained from the PWA. It can be nicely seen, that mainly contributed channels are non-resonant p + K^++ Λ production, $N^*(1650)$, $N^*(1710)$ and $N^*(1880)$. Futhermore the $N^*(1720)$, $N^*(1875)$ and $N^*(1900)$, have negliable contribution for the production. Besides, the significant contributions of the $N^*(1650)$,$N^*(1710)$ and $N^*(1880)$ indicate that these N^* resonances may be necessary for the description of the p + K^++ Λ production. This results shows nice consistency with the results of the Breit-Wigner Parametrizaiton Table 3.3, which give the same trend of the $N^*(1720)$, $N^*(1875)$ and $N^*(1900)$ contribution channels, but with big differences in the non-resonant p + K^++ Λ production, $N^*(1650)$ and$N^*(1895)$ contributions.

4.1.1.4 Systematic Scan of g-value

In Flatté function, coupling constants for pΛ and pΣ influence the shape of cusp and usually it is regarded as one variable, which is ratio of two coupling constants. See Flatté function [6]:

$$A = \frac{C\sqrt{\Gamma_{p\Lambda}\,\Gamma_0}}{(M^2 - s - \mathrm{i}(\Gamma_{p\Lambda} + \Gamma_{p\Sigma^0})M)}, \tag{4.1}$$

$$\Gamma_{p\Lambda} = g_{p\Lambda}\, q_{p\Lambda}\ , \tag{4.2}$$

$$\Gamma_{p\Sigma^0} = g_{p\Sigma^0} q_{p\Sigma^0}, \tag{4.3}$$

The g and q are coupling constants and cm momenta, respectively, more details are in Section 1.3.5.

One one hand, in Flatté Parametrization, $\Gamma_{p\Lambda}$ which locates at numerator plays a role in amplitudes of partial waves and for $\Gamma_{p\Lambda}$ which locates at denominator serves as width part. Since the coupling constant of pΛ gets smaller, the amplitudes and widths of partial waves are reduced. One the other hand, $\Gamma_{p\Sigma}$ locates only at denominator, the real part of its cm momentum plays a role in width and its imaginary part which is below the threshold meets imaginary number i, turning into real values and influencing the amplitudes of partial waves. Since the coupling constant of pΣ gets bigger, the widths of cusp partial waves become bigger and the amplitudes term which locates at denominator will be reduced.

To test if Flatté parametrization is implemented correctly in BG-PWA, a series of analysis of systematic scan of coupling constant g is done. The method is to set the coupling constants as only constants in BG-PWA analysis, by doing 1 iteration [1]. The aim is to find out, what cusp shapes are due to various coupling constants. To get an impression about how these two coupling constants affect the PWA results, a manual variation of the values were performed. (see Table 4.2 for fixed $g_{p\Sigma^0}$ and Table 4.3 for fixed $g_{p\Lambda}$.)

Groups	$g_{p\Sigma}$	$g_{p\Lambda}$	$g_{p\Sigma^0}$ /$g_{p\Lambda}$
1	0.01	0.0144	0.694
2	0.01	0.0100	1.000
3	0.01	0.0064	1.563
4	0.01	0.0025	4

Table 4.2: Various Combinations of Coupling Constants with different $g_{p\Lambda}$ values. $g_{p\Sigma}$ values stay the same.

The Figure 4.3 shows PWA plots of cusp structures in missing mass(pK^+) distribution according to Table 4.2. The PWA results (red line) show that the amplitudes and widths of cusp are reduced with coupling constant of pΛ gets smaller.

The Figure 4.4 shows PWA plots of cusp structures in missing mass(pK^+) distribution according to Table 4.3. The PWA results (red line) show that the amplitudes of cusp are reduced and the widths of cusp are broader with coupling constant of pΛ gets bigger.

Comparing the two groups of results above, the two coupling constants influence the cusp shapes by different ways and this is consistent with mathematic interpreations. Since Breit-Wigner Parametrization has good description of cusp, the symmetric structure of cusp is more

[1] 1 interaction implies, that the values are not changed and of the results, the starting values are used

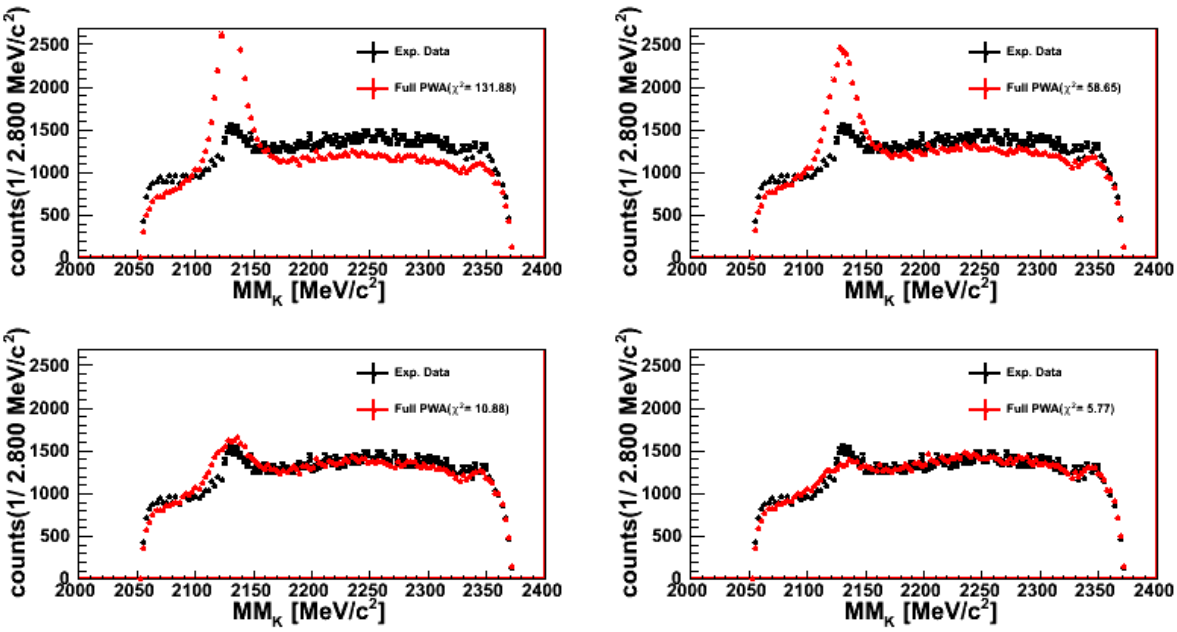

Figure 4.3: Missing mass(p K^+) distribution for the DISTO@2.5 GeV for various groups of various coupling constants. Experimental data are shown as black dots and PWA are red lines.

Groups	$g_{p\Sigma}$	$g_{p\Lambda}$	$g_{p\Sigma^0}$ /$g_{p\Lambda}$
5	0.0025	0.01	0.25
6	0.0064	0.01	0.64
7	0.0144	0.01	1.44
8	0.0225	0.01	2.25

Table 4.3: Various Combinations of Coupling Constants with different $g_{p\Sigma}$ values. $g_{p\Lambda}$ values stay the same.

favored, which indicates that the coupling constant of pΣ is much smaller than that of pΛ . The influence of the coupling values to the amplitude provides further source for ambiguities to the solution. To remove those, a combined analysis is highly required.

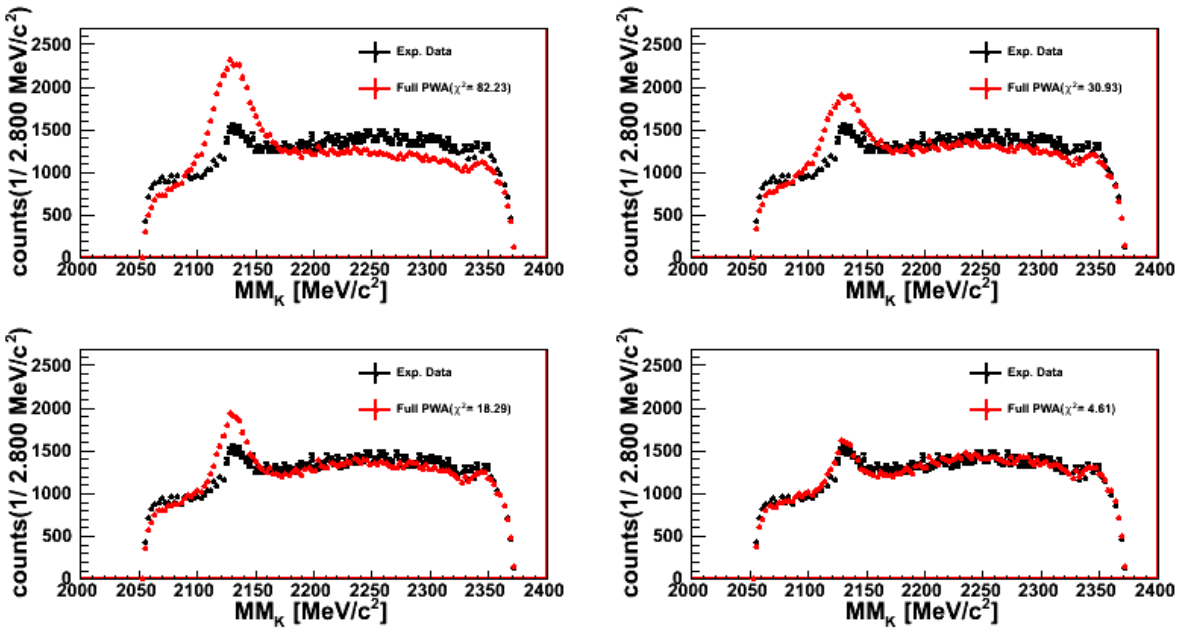

Figure 4.4: Missing mass(p K^+) distribution for the DISTO@2.5 GeV for various groups of various coupling constants. Experimental data are shown as black dots and PWA are red lines.

4.1.2 DISTO @2.14 GeV

4.1.2.1 Fitting Results

To check how PWA works with other data sample with Flatté parametrization, DISTO@2.14 GeV data sample is further used in PWA analysis. The analysis was perfomed like descirbed in Section 4.1.1.

In Figure 4.5, it shows the final PWA fitting result for the missing mass K^+ spectrum of DISTO@2.14 GeV. In these plots, the PWA analysis(red dots) results give a nice description to the experimental K^+ missing mass spectra(black dots). In the Appendix B.a.ii, there are more plots of other observables for DISTO@2.14 GeV data sample including the missing mass spectra of proton and Λ and various angular distributions in dependence of the CMS angles, the Helicity angles, and the Gottfried-Jackson angles Framework. Due to good fitting in these spectra, PWA gives sufficient description for the experimental data.

The cusp in the K^+ missing mass spectrum in this dataset looks different from DISTO @2.5 GeV as well as the physical background below the cusp. In these plots, the cusp as well as the physical background below are all described by the PWA solution with negligible discrepencies. Furthermore, the log likelihood-value χ^2 Section 3.1.4 is -10319.1 and χ^2 /ndf(ndf) is 0.5(644). Compared with DISTO@2.5 GeV, the loglikelihood-value for each dataset is different for it is dependent on the statistics of each dataset. As one can see the χ^2 /ndf value is small, it indicates a relatively good fits to the experimental data.

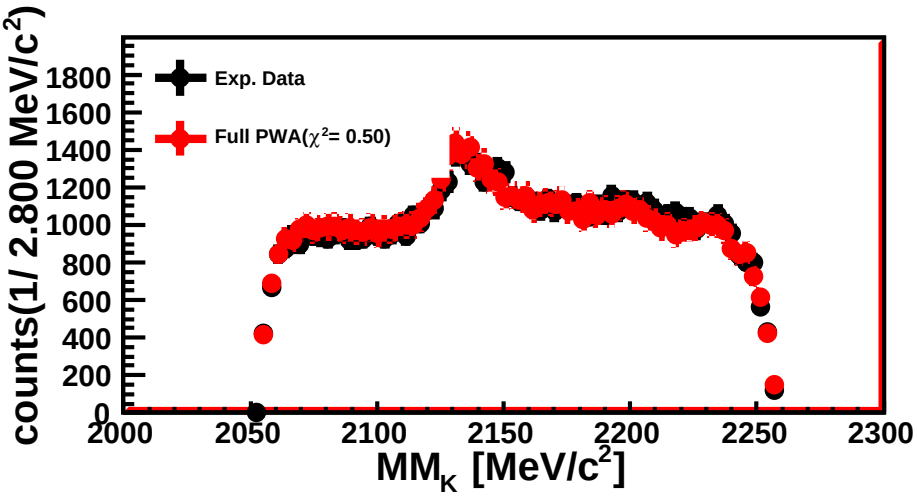

Figure 4.5: Comparison of experimental data (black dots) from the data sample DISTO@2.14 GeV with the results from the Partial Wave Analysis (red dots) in the missing K^+ mass spectrum.The fitting error of PWA is given by the red band.

For the cusp related parameters, the final coupling constants are $g_{N\Sigma} = 1 \times 10^{-3}$ and $g_{p\Lambda} = 1.77 \times 10^{-3}$. The final pole mass is $m_r = 2.13$ GeV/c^2. Comparing with results from DISTO@2.5 GeV, the final coupling constant for NΣ is smaller thant pΛ , but not by that much. Even though the pole mass difference with DISTO@2.5 GeV is minor, the values of coupling constants are not consistent with each other.

4.1.2.2 4π-Plots

In the Figure 4.2, the three different posible cusp waves are given by light green (0^+ S-wave), blue (1^+ S-wave) and pink (1^+ D-Wave) dots. The coherent sum of all cusp waves is given by the light blue curve. It can be nicely seen, the shape of the different cups wave do not differ significant for each other. All of them show peak structure at NΣ threshold, which play a major role for cusp description. The phase-space distribution is given by the dark green curve, which shows isotropic shape.

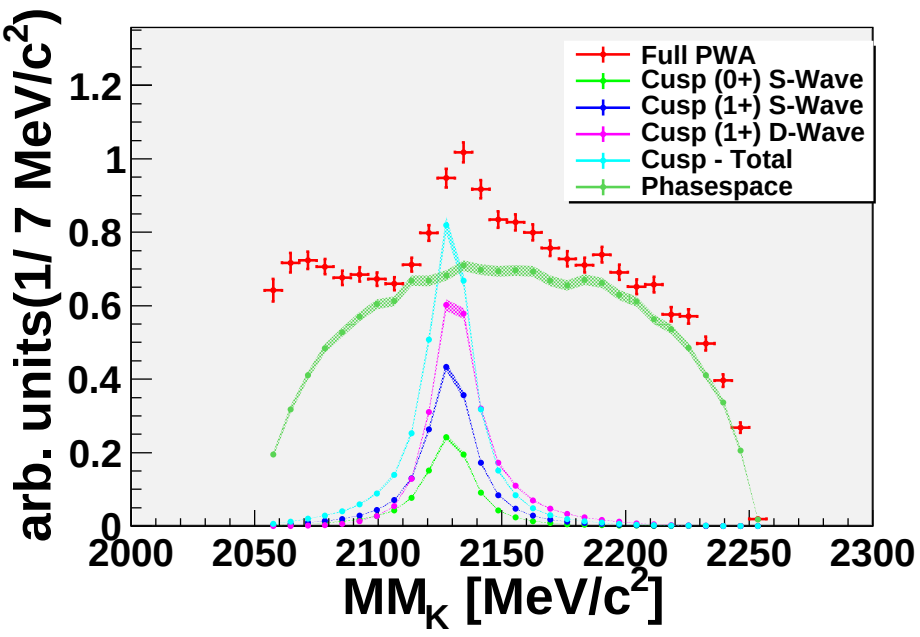

Figure 4.6: Full 4π phase space extrapolation plotting from the data sample DISTO@2.14 GeV in the missing K^+ mass spectrum. It shows Cusp($J^P = 0^+$) S-wave(light green dots), Cusp($J^P = 1^+$) S-wave(blue dots) and Cusp($J^P = 1^+$) D-wave(pink dots). The full PWA(red dots), total cusp waves(light blue dots) and the phase space(green dots) are also shown. The scales of the partial waves are arbitrary.

4.1.2.3 Channel Contributions

Channels	Contributions
$pp \to pK\Lambda$ (direct)	$26.0 \pm 6.6\%$
$pp \to N^*(1650) + p \to p + K^+ + \Lambda$	$6.4 \pm 1.5\%$
$pp \to N^*(1710) + p \to p + K^+ + \Lambda$	$24.7 \pm 6.6\%$
$pp \to N^*(1720) + p \to p + K^+ + \Lambda$	$3.4 \pm 1.0\%$
$pp \to N^*(1875) + p \to p + K^+ + \Lambda$	$0.1 \pm 0\%$
$pp \to N^*(1880) + p \to p + K^+ + \Lambda$	$22.7 \pm 6.1\%$
$pp \to N^*(1895) + p \to p + K^+ + \Lambda$	$14.8 \pm 4.1\%$
$pp \to N^*(1900) + p \to p + K^+ + \Lambda$	$0 \pm 0\%$
$pp \to pK\Sigma \to pK\Lambda$ (S_0^+-Cusp)	$1.2 \pm 0.3\%$
$pp \to pK\Sigma \to pK\Lambda$ (S_1^+-Cusp)	$0.6 \pm 0.1\%$
$pp \to pK\Sigma \to pK\Lambda$ (D_1^+-Cusp)	$0.2 \pm 0\%$

Table 4.4: Relative contributions of the different channels according the bg-pwa results for DISTO@2.14 GeV. The error corresponds to the fitting error of the partial wave analysis.

According to Table 4.4, the realtive strength of all contribution channels are listed with the fitting error, obtained from the PWA. The mainly contributed channels are non-resonant p + K^++ Λ . $N^*(1710)$, $N^*(1880)$ and $N^*(1895)$, which take relative large percentages and it indicate that these N^* 's may be necessary for the description of the p + K^++ Λ production. It is consistent with the conclusion of the results of Breit Wigner Parametrization that $N^*(1720)$, $N^*(1875)$ are not necessary for describing the data set, which is also consistent with Flatté Parametrization for DISTO@2.5 GeV. Compared to DISTO@2.5 GeV results by Flatté Parametrization, the difference is the non-resonant p + K^++ Λ has a large relative contribution and $N^*(1650)$ contributes little in PWA analysis of DISTO@2.14 GeV data. The contributions of N^* resonances using Flatté get some consistency with Breit-Wigner is a good sign. It indicates stability of the PWA analysis to the background below the cusp. The discrepencies might be caused by different cusp parametrization. The DISTO@2.14 GeV data sample does not include $N^*(1900)$, which is limited by initial beam energy.

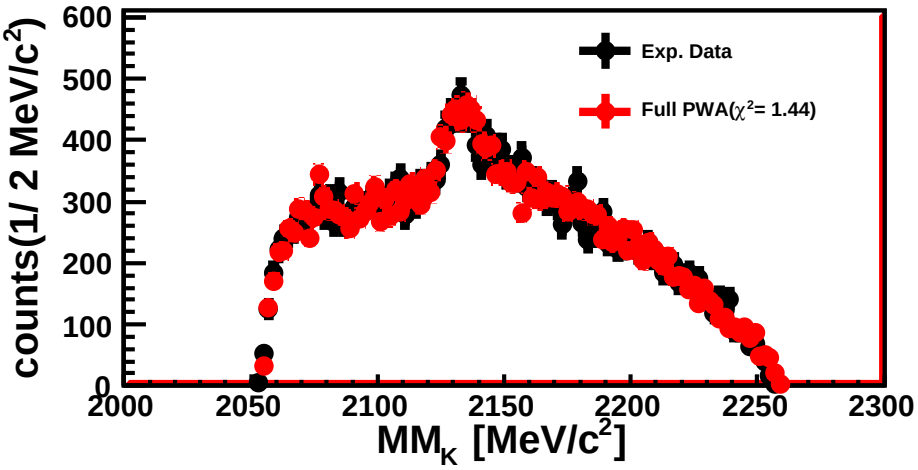

Figure 4.7: Comparison of experimental data (black dots) from the data sample COSY-TOF@2.16 GeV with the results from the Partial Wave Analysis (red dots) in the missing K^+ mass spectrum.The fitting error of PWA is given by the red band.

4.1.3 COSY-TOF@2.16 GeV

4.1.3.1 Fitting Results

The PWA analysis above all implemented on data sample from DISTO Collaborations. Furthermore, It is interesting to see how it works out on data sample from other Collaborations, eg, COSY-TOF.

The final PWA fitting result for the missing mass K^+ spectrum of COSY-TOF@2.16 GeV is given in Figure 4.7. In these plots, the PWA analysis(red dots) results also gives a nice description to the experimental K^+ missing mass spectra(black dots) and in the Appendix B.a.iii, it includes other observables PWA plots for COSY-TOF@2.16 GeV data sample with good fittings. According to all these PWA results, this procedure gives sufficient description for the experimental data. The fitting error is indicated as red band.

In these plots, the cusp as well as the physical background below are all described by the PWA solution with some minor errors. Furthermore, the total log-likelihood-value χ^2 Section 3.1.4 is -2466.5 and χ^2 /ndf(ndf) is 1.44(712). Again, compared with DISTO@2.5 GeV and DISTO @2.14 GeV, the loglikelihood-value for each dataset is different for it is dependent on the statistics of each dataset. As one can see the χ^2 /ndf value is small, it indicates a relatively good fits to the experimental data.

The resulting coupling constants from the PWA fit are are $g_{N\Sigma} = 1 \times 10^{-3}$ and $g_{p\Lambda} = 0.1$. The final pole mass is $m_r = 2.128$ GeV/c^2. Again, the final coupling constant for NΣ is smaller thant pΛ , but is not in a large order. In the case of COSY-TOF@2.16 GeV data sample, the small coupling constant for NΣ (≤ 0.001) is only possibility observed. For DISTO@2.5 GeV and DISTO@2.14 GeV data, the values of coupling constants are showing non-unique solu-

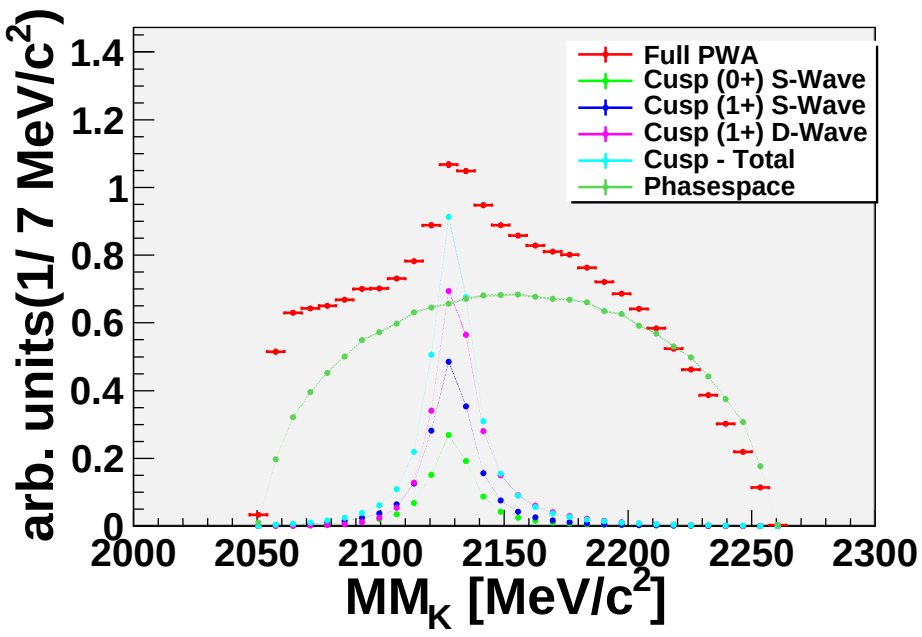

Figure 4.8: Full 4π phase space extrapolation plotting from the data sample COSY-TOF@2.16 GeV in the missing K^+ mass spectrum. It shows Cusp($J^P = 0^+$) S-wave(light green dots), Cusp($J^P = 1^+$) S-wave(blue dots) and Cusp($J^P = 1^+$) D-wave(pink dots). The full PWA(red dots), total cusp waves(light blue dots) and the phase space(green dots) are also shown. The scales of the partial waves are arbitrary.

tions.

4.1.3.2 4π-Plots

In the Figure 4.2, the three different posible cusp waves are given by light green (0^+ S-wave), blue (1^+ S-wave) and pink (1^+ D-Wave) dots. The coherent sum of all cusp waves is given by the light blue curve. Is can be nicely seen, the shape of the different cups wave do not differ significant for each other. Besides, all of them show peak structure at NΣ threshold. The phase-space distribution is given by the dark green curve, which shows isotropic shape.

4.1.3.3 Channel Contributions

In Table 4.5, the realtive strength of all contribution channels are listed with the fitting error, obtained from the PWA. In can be nicely seen, that mainly contributed channels are non-resonant p + K^++ Λ production, $N^*(1650)$ and $N^*(1720)$. For COSY-TOF beam energy range, high N^* resonances are excluded. The non-resonant p + K^++ Λ production channel contributes especially most, which is consistent with DISTO @2.14 GeV, but disagree with DISTO @2.5 GeV. The reason might be their different beam energy region. Besides, then N^*

Channels	Contributions
$pp \to pK\Lambda$ (direct)	$34.1 \pm 4.2\%$
$pp \to N^*(1650) + p \to p + K^+ + \Lambda$	$29.4 \pm 3.3\%$
$pp \to N^*(1710) + p \to p + K^+ + \Lambda$	$9.4 \pm 1.3\%$
$pp \to N^*(1720) + p \to p + K^+ + \Lambda$	$15.6 \pm 1.7\%$
$pp \to N^*(1875) + p \to p + K^+ + \Lambda$	$0 \pm 0\%$
$pp \to N^*(1880) + p \to p + K^+ + \Lambda$	$0 \pm 0\%$
$pp \to N^*(1895) + p \to p + K^+ + \Lambda$	$0 \pm 0\%$
$pp \to N^*(1900) + p \to p + K^+ + \Lambda$	$0 \pm 0\%$
$pp \to pK\Sigma \to pK\Lambda$ (S_0^+-Cusp)	$1.4 \pm 0\%$
$pp \to pK\Sigma \to pK\Lambda$ (S_1^+-Cusp)	$7.7 \pm 0.8\%$
$pp \to pK\Sigma \to pK\Lambda$ (D_1^+-Cusp)	$2.4 \pm 0.4\%$

Table 4.5: Relative contributions of the different channels according the BG-PWA results. The error corresponds to the fitting error of the partial wave analysis.

(1650) also plays a big role for description of experiment data sets.

4.1.3.4 Systematic Scan

Like it was shown for all single analysis, ambiguities can not be ruled out if only one beam beam energy sample is analyzed. To get an impression for the ambiguities, a scan for the inclusion of N^* resonances was performed based on the solution extract for COSY-TOF@2.16 GeV data sample. For this reason different N^* resonance were disabled.

In Table 4.6, the results for all eight combinations are given. It can be seen, that also the contribution of the further channel differ quite a lot between the solutions. The quality parameter loglikelihood value can be used to exclude several of these solutions. Just solution A(111) and D(011) provided comparable value for the Loglike. Especially the solution with any N^* resonance H(000) can be ruled out completely.

Comparing the contributions of the two best solution A(111) and D(011) it is a quite unexpected, that a solution, which does not include $N^*(1650)$, provided good solution, since a this solution is expected to have a non negligible contribution. Furthermore it can be seen, that also the contribution of the further channel differ quite a lot between the solution.

A possible explanation for this behaviour is that it shows the difficulty of making quantitative statements about the reaction using only one data set at a single energy, while in principle the systematical scan is useful to get a handle on systematical uncertainties of the analysis and to check the stability of the result. The ambiguity also means that it is not expected for further systematical scans for other single energy BG-PWA result to yield much useful information. For this reason a combined analysis is required, which is expected to pin down the contribution more accurate.

Channels	A(111)	B(110)	C(101)	D(011)
Loglike.	-2466.495	-1714.123	-829.739	-2601.013
$pK\Lambda$ (direct)	$36.55 \pm 6.60\%$	$42.13 \pm 7.61\%$	$47.72 \pm 8.63\%$	$53.81 \pm 9.65\%$
$N^*(1650)$	$24.87 \pm 4.57\%$	$28.43 \pm 5.08\%$	$31.98 \pm 5.58\%$	0.00 %
$N^*(1710)L$	$22.84 \pm 4.06\%$	$26.40 \pm 4.60\%$	0.00 %	$27.41 \pm 5.1\%$
$N^*(1720)$	$13.20 \pm 2.64\%$	0.00 %	$17.26 \pm 3.05\%$	$13.20 \pm 2.53\%$
$pK\Sigma$ (S_0^+-Cusp)	$1.52 \pm 0.51\%$	$2.03 \pm 0.51\%$	$2.03 \pm 0.51\%$	$5.1 \pm 0\%$
$pK\Sigma$ (S_1^+-Cusp)	$0.51 \pm 0\%$	$0.51 \pm 0\%$	$1.01 \pm 0\%$	$4.06 \pm 0.51\%$
$pK\Sigma$ (D_1^+-Cusp)	$0.2 \pm 0\%$	$0.2 \pm 0\%$	$0.2 \pm 0\%$	$0.2 \pm 0\%$
%	E(001)	F(010)	G(100)	H(000)
Loglike.	-2507.594	-1263.895	-2499.875	-746.184
$pK\Lambda$ (direct)	$66 \pm 12\%$	$58.89 \pm 10.66\%$	$54.82 \pm 9.61\%$	$74.21 \pm 15.2\%$
$N^*(1650)$	0.00%	0.00%	$39.01 \pm 7.11\%$	0.00%
$N^*(1710)$	0.00%	$37.06 \pm 6.60\%$	0.00%	0.00%
$N^*(1720)$	$22 \pm 4\%$	0.00%	0.00%	0.00%
$pK\Sigma$ (S_0^+-Cusp)	$3.05 \pm 0.51\%$	$2.54 \pm 0.51\%$	$1.52 \pm 0\%$	$9.8 \pm 2.1\%$
$pK\Sigma$ (S_1^+-Cusp)	$8.12 \pm 1.52\%$	$1.01 \pm 0\%$	$3.55 \pm 0.51\%$	$6.6 \pm 1.02\%$
$pK\Sigma$ (D_1^+-Cusp)	$0.2 \pm 0\%$	$0.2 \pm 0\%$	$0.2 \pm 0\%$	$0.2 \pm 0\%$

Table 4.6: Loglike values and relative contribution for the different parameters set of the systematical scan are listen. Each set contains a different set of N^* resonance.

4.1.4 Summary of Single Data Analysis

First of all, the PWA analysis give a nice agreement with experimental data for various datases, especilly it can be seen, that the cusp can be description by a Flatté parametrizied wave. The fitting results of BG-PWA converges with negative Log-likelihood value and small χ^2 /ndf values.

Secondly, it can be seen that the PWA results obtained for a single energy are not unique between several data sets. If one changes the starting values of parameters, the results can also turn out to be many possibilities. This gives the clear hint for ambiguities of final results. It is one reason that why it requires combined analysis. The results ambiguity also means that it is not expected for further systematical scans for other single energy BG-PWA result to yield much useful information. However, even though the systematical scan is useful to get a handle on systematical uncertainties of the analysis and to check the stability of the result, it shows the difficulty of making quantitative statements about the reaction using only one data set at a single energy.

As for cusp structure, one point of view is that, since the symmetric Breit-Wigner parametrization already gives a good explanation of the experimental data. Thus it is expected the $g_{\lambda p} \gg g_{\sigma p}$, which would lead to a symmetric structure of the flatté function. But the different results are derived from analysis for separate different dataset.

These three datasets all include NΣ cusp effect in the missing K^+ spectra, and all of them are

taken under the similar experiment process: pp $\rightarrow$p + K^++ Λ . Even though the experiments are taken place at different collaborations and envionments, the physical background under the cusp is described well by PWA for each dataset and Flatté is like Breit-Wigner , working as parametrizaion function which has nothing to do with the beam energy. So a unique solution is forwarded. As introduced in the introduction chapter, the coupling constants have scaling behaviour. However, the threshold mass values are different and there is no clear tendency for coupling constants, neither.

To solve this, an idea of combined data analysis is proposed. The combined data analysis will be explained in the next chapter.

4.2 Combined Data Analysis

In the single data analysis, it was shown, that there is no unique solution derived the ambiguities appear for the ratio of the contributing channels. However, more than one data sample is used and processed by PWA at same time, one can reduce ambiguieties, if there is only one solution is not sure. In this way, it reduces the ambiguities appear for single data analysis and get one solution workable for all datasets included. This method is called combined data analysis.

In combined data analysis, if more than one data sample is used, the data samples are fitted parallel, which means, that the parameters are optimized to explained all data samples, so there is only one solution for all datasets and this solution should fit all datasets well. At the same time the parallel fitting assure, that different detector acceptance and efficiency for different spectrometers and beam energies are not mixed. The Log-likelihood values for each samples are determined separately and added up afterwards. [35] A combined analysis of data sets at differing energy on one hand can get rid of most of this ambiguity in the PWA description. On the other hand, a further systematical scan is expected to be of great use since most of the results ambiguity can then be eliminated.

As the parameter set should contain all possible production channels, it is mainly taken from the parameter set in the single data analysis, which describes the data sets with highest beam energy among all data sets included to make sure all possible production channels are included. The starting value for threshold mass is 2.13 GeV according to the single data analysis of Flatté distribution. The starting values for two coupling constants are set to 0.01, separately, at the beginning of attempts.

The combined analyis was done in steps. Firstly only two sample were analysed (Section 4.2.1), followed by adding one (Section 4.2.2) and two (Section 4.2.3) further data sample. This steps were done to analyze the influence of the different data set to the results.

4.2.1 DISTO @2.5 GeV+DISTO @2.14 GeV

At the beginning, to perform the combined data analysis, the two data sets DISTO@2.14 GeV and DISTO@2.5 GeV are fitted together. From single data analysis for DISTO@2.5 GeV and DISTO@2.14 GeV by Flatté Parametrization separately, there are more than one option of initial coupling constants before PWA. But it also shows that the initial coupling constants of 0.01 for both $N\Sigma$ and $p\Lambda$ are workable for each of two DISTOdata sets. So they are set to these values and let them run freely. Also, the amplitude parameterset of DISTO@2.5 GeV, which is with higher beam energy, is used for the combined data analysis.

4.2.1.1 Fitting Results

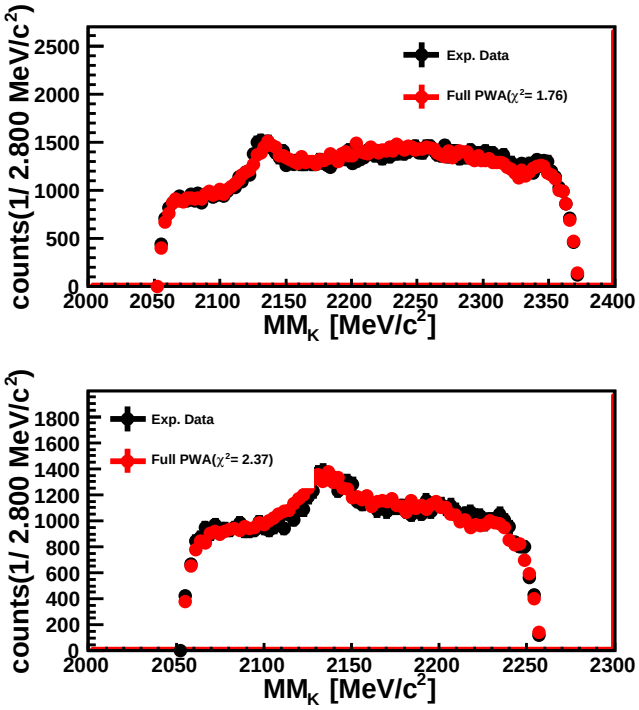

Figure 4.9: Comparison of experimental data (black dots) from the data sample DISTO@2.5 GeV and DISTO@2.14 GeV with the results from the Partial Wave Analysis (red dots) in the missing K^+ mass spectrum.The fitting error of PWA is given by the red band.

The final PWA fitting results for the missing mass K^+ spectrum of DISTO@2.5 GeV and DISTO@2.14 GeV are given in Figure 4.9. In these plots, the PWA analysis(red dots) results give a nice description to the experimental K^+ missing mass spectra(black dots). The PWA results are scaled to the experimental data points, by normalizing to the same value of the integral of all points. In the Appendix B.b.i, the Λ and p missing mass spectrum as well as the various angular distributions in dependence of the CMS angles, the Helicity angles, and the Gottfried-Jackson angles are shown. These plots also have to give sufficient descriptions for

the experimental data, but minor discrepancies are allowed which is within the systematical error of the PWA procedure. In the plots, the cusp as well as the physical background below are all described by the PWA solution with minor discrepancies.

The main interest of the analysis are the cusp related values. For this dataset, the final coupling constants are $g_{N\Sigma} = 1 \times 10^{-6}$ and $g_{p\Lambda} = 0.135$. In fact, it is not unique solution. It is one of the reason to include more data samples into combined data analysis.

4.2.1.2 4π-Plots

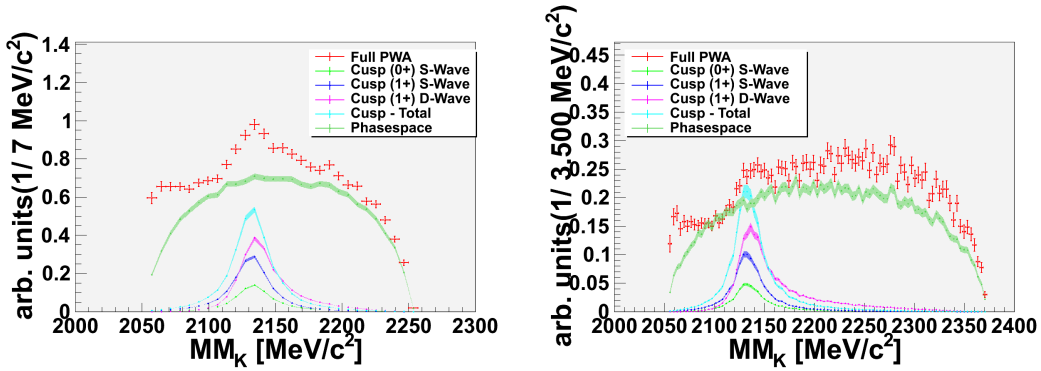

Figure 4.10: Full 4π phase space extrapolation plotting from the data sample DISTO@2.14 GeV(left), DISTO@2.5 GeV in the missing K^+ mass spectrum. It shows Cusp($J^P = 0^+$) S-wave(light green dots), Cusp($J^P = 1^+$) S-wave(blue dots) and Cusp($J^P = 1^+$) D-wave(pink dots). The full PWA(red dots), total cusp waves(light blue dots) and the phase space(green dots) are also shown. The scales of the partial waves are arbitrary.

In the Figure 4.10 for each data sample, the phase-space distribution is given by the dark green curve. The three different posible cusp waves are given by light green (0^+ S-wave), blue (1^+ S-wave) and pink (1^+ D-Wave) dots. The coherent sum of all cusp waves is given by the light blue curve. They all show peak structures at NΣ threshold, which play a major role for cusp description. In total, the coherent sum of all cusp waves (light blue curve) shows a peak structure around NΣ threshold. The scales of the partial waves are arbitrary.

4.2.1.3 Channel Contributions

Furthermore, the total log likelihood value and reduced χ^2 for this result are listed, which indicates the quality of pwa analysis results. And the relative contributions of direct p + K^++ Λ production and N^* resonances are also listed in the table Table 4.7.

According to Table 4.7, the realtive strength of all contribution channels are listed with the fitting error, obtained from the PWA. It can be nicely seen, that mainly contributed channels are non-resonant p + K^++ Λ production, $N^*(1650)$, $N^*(1710)$ for DISTO@2.14 GeV

parameter set	DISTO@2.14 GeV	DISTO@2.5 GeV
log likelihood	-15130.5	-9892.484
χ^2 /ndf(ndf)	3.7146(644)	3.0767(766)
$pp \to pK\Lambda$ (direct)	$24.8 \pm 6.6\%$	$21.3 \pm 4.2\%$
$pp \to N^*(1650) + p \to p + K^+ + \Lambda$	$20.9 \pm 5.6\%$	$10.3 \pm 1.9\%$
$pp \to N^*(1710) + p \to p + K^+ + \Lambda$	$26.8 \pm 7.1\%$	$31.7 \pm 6.1\%$
$pp \to N^*(1720) + p \to p + K^+ + \Lambda$	$1.9 \pm 0.5\%$	$2.8 \pm 0.6\%$
$pp \to N^*(1875) + p \to p + K^+ + \Lambda$	$0.3 \pm 0\%$	$1.1 \pm 0.3\%$
$pp \to N^*(1880) + p \to p + K^+ + \Lambda$	$4.5 \pm 1.0\%$	$11.6 \pm 2.3\%$
$pp \to N^*(1895) + p \to p + K^+ + \Lambda$	$3.9 \pm 1.0\%$	$9.0 \pm 1.6\%$
$pp \to N^*(1900) + p \to p + K^+ + \Lambda$	$0.6 \pm 0\%$	$1.3 \pm 0.3\%$
$pp \to pK\Sigma \to pK\Lambda$ (S_0^+-Cusp)	$2.4 \pm 0.5\%$	$0.8 \pm 0\%$
$pp \to pK\Sigma \to pK\Lambda$ (S_1^+-Cusp)	$12.8 \pm 3.6\%$	$9.2 \pm 1.6\%$
$pp \to pK\Sigma \to pK\Lambda$ (D_1^+-Cusp)	$0.9 \pm 0\%$	$0.9 \pm 0.3\%$

Table 4.7: Relative contributions of the different channels according the bg-pwa results for DISTO@2.5 GeV and DISTO@2.14 GeV . The error correspond to the fitting error of the partial wave analysis and the normalization to 100%.

and it is inconsistent with single data analysis with minor contribution of $N^*(1650)$. For DISTO@2.14 GeV, other channels contribute little. The mainly contributed channels for DISTO@2.5 GeV are non-resonant p + K^++ Λ production and $N^*(1710)$, but with less contributions of $N^*(1650)$ and higher contributions of $N^*(1880)$ comparing to DISTO@2.14 GeV. Still, the $N^*(1720)$, $N^*(1875)$ and $N^*(1900)$, have negliable contribution for the production for both data samples.

4.2.2 DISTO@2.5 GeV+DISTO@2.14 GeV+COSY-TOF@2.16 GeV

It was already shown in Section 4.2.1, that a combined analysis of just the DISTO sample give the expected result. To stabilize this results, that combined analysis including also the COSY-TOF@2.16 GeV were included. This is an important step, since data samples are from different experiments, which include e.g. different angular acceptance of the detectors.

4.2.2.1 Fitting Results

As a starting point, the parameter set from the single analysis for DISTOsamples @2.5 GeV were used, since it is a solution for the highest beam energy among the three datasets and it turns out good fitting already for two datasets analysis. The starting values are chosen as stated in the introduction of this chapter. Setting the two coupling constants equally is the idear that one can not tell which value will becomes smaller or higher.

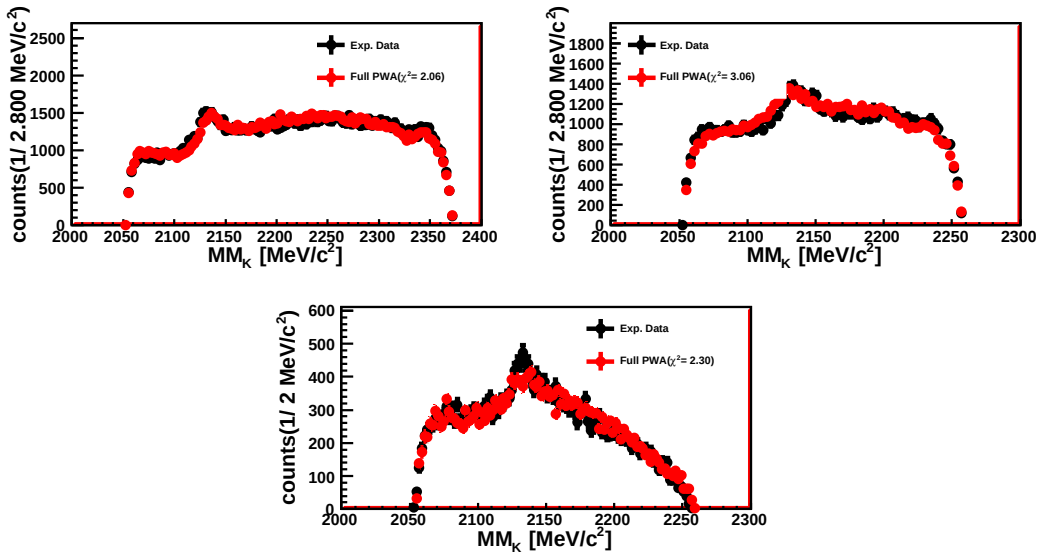

Figure 4.11: Comparison of experimental data (black dots) from the data sample DISTO@2.5 GeV, DISTO@2.14 GeV and COSY-TOF@2.16 GeV with the results from the Partial Wave Analysis (red dots) in the missing K^+ mass spectrum.The fitting error of PWA is given by the red band.

The final PWA fitting results for the missing mass K^+ spectrum of DISTO @2.5 GeV, DISTO @2.14 GeV and COSY-TOF@2.16 GeV are given in Figure 4.11. In these plots, the PWA analysis(red dots) results give a nice description to the experimental K^+ missing mass spectra(black dots). The PWA results are scaled to the experimental data points, by normalizing to the same value of the integral of all points. In the Appendix B.b.ii, there are PWA plots not only for the K^+ missing mass spectra, but also for Λ and p missing mass spectrum as well as the various angular distributions in dependence of the CMS angles, the Helicity angles, and the Gottfried-Jackson angles shown. In the plots, the cusp as well as the physical background

below are all described by the PWA solution with minor discrepancies. The cusp related values are given later in Section 4.2.2.4.

4.2.2.2 4π-Plots

The 4Pi-Plotting is to extrapolate the results to the full phase space by adding additional data samples to PWA fitting procedure.

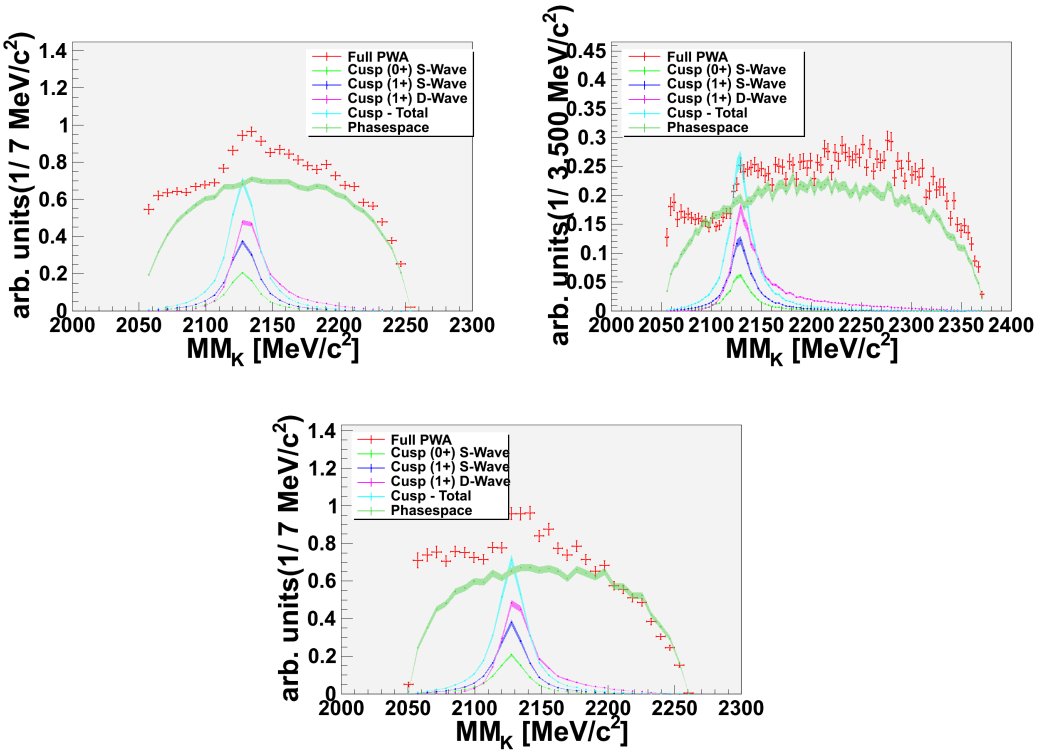

Figure 4.12: Full 4π phase space extrapolation plotting from the data sample DISTO@2.14 GeV(left), DISTO@2.5 GeV and COSY-TOF @2.16 GeV in the missing K^+ mass spectrum. It shows Cusp($J^P = 0^+$) S-wave(light green dots), Cusp($J^P = 1^+$) S-wave(blue dots) and Cusp($J^P = 1^+$) D-wave(pink dots). The full PWA(red dots), total cusp waves(light blue dots) and the phase space(green dots) are also shown. The scales of the partial waves are arbitrary.

In the Figure 4.12 for each data sample, the phase-space distribution is given by the dark green curve. The three different posible cusp waves are given by light green (0^+ S-wave), blue (1^+ S-wave) and pink (1^+ D-Wave) dots. The coherent sum of all cusp waves is given by the light blue curve. Is can be nicely seen, the shape of the different cups wave do not differ significant for each other and they all show peak structures at NΣ threshold, which play a major role for cusp description.

4.2.2.3 Systematic Scan

As stated in Section 3.1.4, the solution of PWA also depends on the chosen initial values of the free parameters. It must be checked how stable the solution is under varying the starting values of parameters. These can be checked by a systematic scan under exclusion of one or more resonant production channels. In this way, it can be checked whether the full solution is stable under altering choices of initial parameter values through comparison of the 5 best results obtained in the scan. A systematical scan was performed for the combined analysis of the DISTO @2.5 GeV,DISTO@2.14 GeV and COSY-TOF@2.16 GeV data sets. In Table 4.8, the best five solutions are show, together with the list of included solution.

parameter set	A	B	C	D	E
Loglike value for sample	-27303.851	-27133.55	-26996.392	-26940.7	-26935.597
$pK\Lambda$ (direct)	x	x	x	x	x
N^* (1650)	x	x	x	x	x
N^* (1710)	x	x	x	x	x
N^* (1720)	x	x	x	x	-
N^* (1875)	x	-	x	-	x
N^* (1880)	x	x	x	x	x
N^* (1895)	x	x	x	x	x
N^* (1900)	x	x	-	-	x
$pK\Sigma$ (S_0^+-Cusp)	x	x	x	x	x
$pK\Sigma$ (S_1^+-Cusp)	x	x	x	x	x
$pK\Sigma$ (D_1^+-Cusp)	x	x	x	x	x

Table 4.8: Inclusion table for the best five parameters set of the systematical scan of the PWA for the combined analysis with the flatté parametrization. In the the Loglike value is given. An included channel in a parameter set is indicated by an x and excluded channel by an -.

In Table 4.8, one can see in details that the inclusion of the $N^*(1720)$, $N^*(1875)$, and $N^*(1900)$ resonances does not strongly alter the quality of the result, which means that these three resonances are not necessary for describing the data set. The details of systematical results are shown in Section B.b.ii.i.

Interestingly, the five best solutions for this combined systematical scans correspond to the same subsets of N^*resonances as the five best solutions for the systematical scan done with Breit-Wigner in Table 3.3, i.e. for the combined analysis one can also describe the data sets without inclusion of the $N^*(1720)$, $N^*(1875)$, and $N^*(1900)$ resonances. This shows that the BG-PWA is actually capable to find good solutions for multiple data sets which are consistent with each other even if the analyses are conducted independently.

4.2.2.4 Channel Contributions

Furthermore, the relative Contribution from the mean value of the five best solutions for the different contribution channels the combined analysis with flatté parametrization for the DISTO @2.5 GeV,DISTO@2.14 GeV and COSY-TOF@2.16 GeV with errors are also given.

	DI@2.5 GeV	DI@2.14 GeV	CO@2.16 GeV
$pK\Lambda$ (direct)	$23.10 \pm 4.33 \pm 1.94\%$	$23.05 \pm 4.21 \pm 1.89\%$	$23.96 \pm 4.46 \pm 2.00\%$
$N^*(1650)$	$13.57 \pm 2.49 \pm 1.12\%$	$25.16 \pm 4.53 \pm 2.03\%$	$26.52 \pm 4.67 \pm 2.10\%$
$N^*(1710)$	$27.34 \pm 5.12 \pm 2.29\%$	$25.79 \pm 4.53 \pm 2.03\%$	$22.64 \pm 4.06 \pm 1.82\%$
$N^*(1720)$	$3.61 \pm 0.66 \pm 0.33\%$	$2.53 \pm 0.42 \pm 0.21\%$	$2.64 \pm 0.41 \pm 0.20\%$
$N^*(1875)$	$0.61 \pm 0.13 \pm 0.09\%$	$0.15 \pm 0.13 \pm 0.13\%$	$0.31 \pm 0 \pm 0\%$
$N^*(1880)$	$10.29 \pm 1.72 \pm 0.79\%$	$4.31 \pm 0.63 \pm 0.30\%$	$4.06 \pm 0.61 \pm 0.29\%$
$N^*(1895)$	$10.43 \pm 1.97 \pm 0.89\%$	$5.48 \pm 0.95 \pm 0.43\%$	$4.37 \pm 0.82 \pm 0.38\%$
$N^*(1900)$	$1.57 \pm 0.26 \pm 0.16\%$	$0.73 \pm 0.11 \pm 0.11\%$	$0.71 \pm 0.10 \pm 0.10\%$
$pK\Sigma$ (S_0^+-Cusp)	$1.59 \pm 0.33 \pm 0.15\%$	$1.90 \pm 0.42 \pm 0.21\%$	$2.23 \pm 0.41 \pm 0.20\%$
$pK\Sigma$ (S_1^+-Cusp)	$7.34 \pm 1.31 \pm 0.59\%$	$10.65 \pm 1.79 \pm 0.81\%$	$12.38 \pm 2.05 \pm 0.92\%$
$pK\Sigma$ (D_1^+-Cusp)	$0.2 \pm 0 \pm 0\%$	$0.2 \pm 0 \pm 0\%$	$0.2 \pm 0 \pm 0\%$

Table 4.9: Relative Contribution from the mean value of the five best solutions for the different contribution channels the combined analysis with flatté parametrization for the DISTO @2.5 GeV,DISTO@2.14 GeV and COSY-TOF@2.16 GeV. And errors are average fitting error and the standard deviation of the results from the five best solutions.

According to Table 4.9, the realtive strength from the mean value of the five best solutions for the different contribution channels with the standard deviation of the results from the scan. It can be nicely seen, that mainly contributed channels for all three datasets are non-resonant p + K^++ Λ production and $N^*(1710)$. The $N^*(1650)$ is a mainly contributed channel, but not in case of DISTO @2.5 GeV. For DISTO@2.14 GeV and COSY-TOF@2.16 GeV, their mainly contributed channels are the same and take quite large percentage. However, for the DISTO @2.5 GeV, the $N^*(1650)$, $N^*(1880)$ and $N^*(1895)$ also takes non-negligible percentages. What is in common for all three datasets are that $N^*(1720)$, $N^*(1875)$, and $N^*(1900)$ contribute quite small, which also indicate they are not necessary for describing the data set. This conclusion is always consistent with any analysis that performed. All systematic error is below 10%. Base on these solutions, including all possible channels, a systematical scan, which varies the combined of included N^* resonance war performed.

The cusp related values from five best solutions with their systematic errors are shown in Table 4.10.

Systematical Scan	$g_{N\Sigma}$	$g_{p\Lambda}$
A	$0.1 \pm 0.01 \times 10^{-2}$	$13.6 \pm 0.10 \times 10^{-2}$
B	$0.1 \pm 0.01 \times 10^{-2}$	$13.1 \pm 0.09 \times 10^{-2}$
C	$0.1 \pm 0.01 \times 10^{-2}$	$12.5 \pm 0.11 \times 10^{-2}$
D	$0.1 \pm 0.01 \times 10^{-2}$	$12.4 \pm 0.09 \times 10^{-2}$
E	$0.1 \pm 0.01 \times 10^{-2}$	$12.6 \pm 0.11 \times 10^{-2}$

Table 4.10: Coupling constants for the best five parameters set of the systematical scan of the PWA for the combined analysis with the flatté parametrization.

The result show also a sufficient description for these sample with very small value for $g_{p\Sigma^0}$, with which the cusp turns out to symmetric shape. These values are consistent with com-

bined data analysis Section 4.2.1, which is not much surprising, since it is only one solution has benn found for COSY-TOF@2.16 GeV, in which the coupling constants for pΣ^0 is quite small. However, such small $g_{p\Sigma^0}$ also shows small coupling strength, but the cusp, which as interpreted causing by two channel interaction, is clearly visible in the experimental data. It raises the question that if the coupling constant for pΣ^0 is truly so small. In Section 4.2.3, there is new results found for four-data combined analysis.

The coupling constants for pΛ and NΣ can be calulated using functions in Appendix A.e that $g_{N\Sigma} = 0.1 \pm 0.01 \times 10^{-2} \pm 0.0045$ and $g_{p\Lambda} = 12.8 \pm 0.10 \times 10^{-2} \pm 0.045$ with the first error from the propagated errror of the signle systematic fitting and second error from the standard deviation of the five values. The calculated scattering length for NΣ (Section 1.4) is $a_{N\Sigma} \approx (5.88 \times 10^{-4} - i0.535 \times 10^{-2}) fm$. One reason for this small value may be due to the small coupling constants of NΣ . The combined data analysis is also capable of adding more data samples. So there is one with four data samples are shown as following.

4.2.3 DISTO@2.5 GeV+DISTO@2.14 GeV+COSY-TOF@2.14 GeV+DISTO@2.85 GeV

4.2.3.1 Fitting Results

Since the PWA provides a solution, which reproduces very nicely the experimental data of the three data sample DISTO@2.5 GeV+DISTO@2.14 GeV+COSY-TOF@2.16 GeV, in the last step, the DISTO sample with the higherst energy DISTO@2.85 GeV was added. In this final fitting all data set, which have a visible cusp structure are fitted in parallel. As a starting point, the parameter set from the single analysis for DISTOsamples @2.85 GeV were used. The initial coupling constants and threshold mass are set as the same as before.

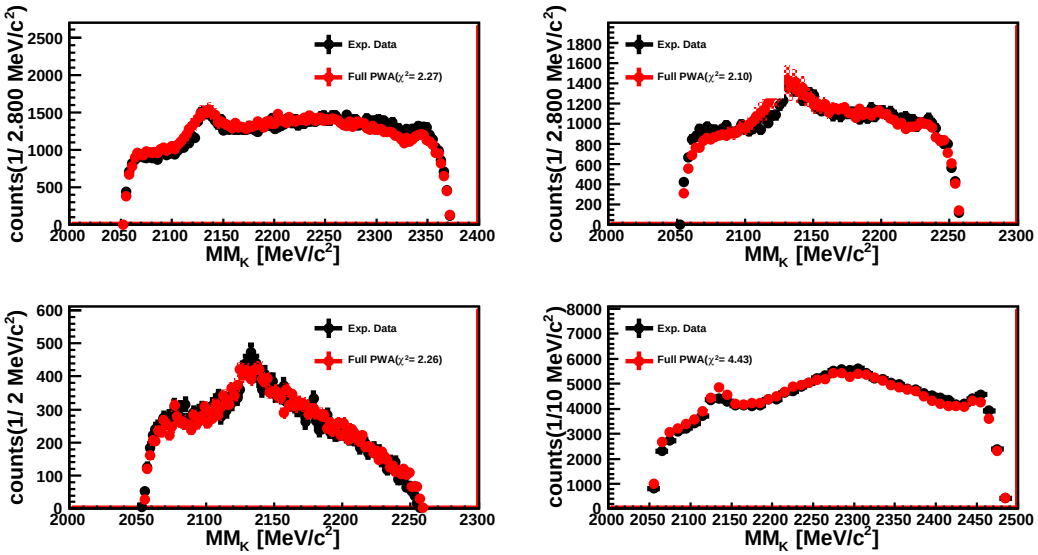

Figure 4.13: Comparison of experimental data (black dots) from the data sample DISTO@2.5 GeV, DISTO@2.14 GeV, COSY-TOF@2.16 GeV and DISTO@2.85 GeV with the results from the Partial Wave Analysis (red dots) in the missing K^+ mass spectrum.The fitting error of PWA is given by the red band.

The final PWA fitting results for the missing mass K^+ spectrum of DISTO @2.5 GeV, DISTO @2.14 GeV, COSY-TOF@2.16 GeV and DISTO@2.85 GeV are given in Figure 4.13. In these plots, the PWA analysis(red dots) results give a nice description to the experimental K^+ missing mass spectra(black dots). The PWA results are scaled to the experimental data points, by normalizing to the same value of the integral of all points. In the Appendix B.b.iii, there are PWA plots not only for the K^+ missing mass spectra, but also for Λ and p missing mass spectrum as well as the various angular distributions in dependence of the CMS angles, the Helicity angles, and the Gottfried-Jackson angles shown. In the plots, the cusp as well as the physical background below are all described by the PWA solution with minor discrepancies.The cusp related values are given later in Section 4.2.3.4.

4.2.3.2 4π-Plots

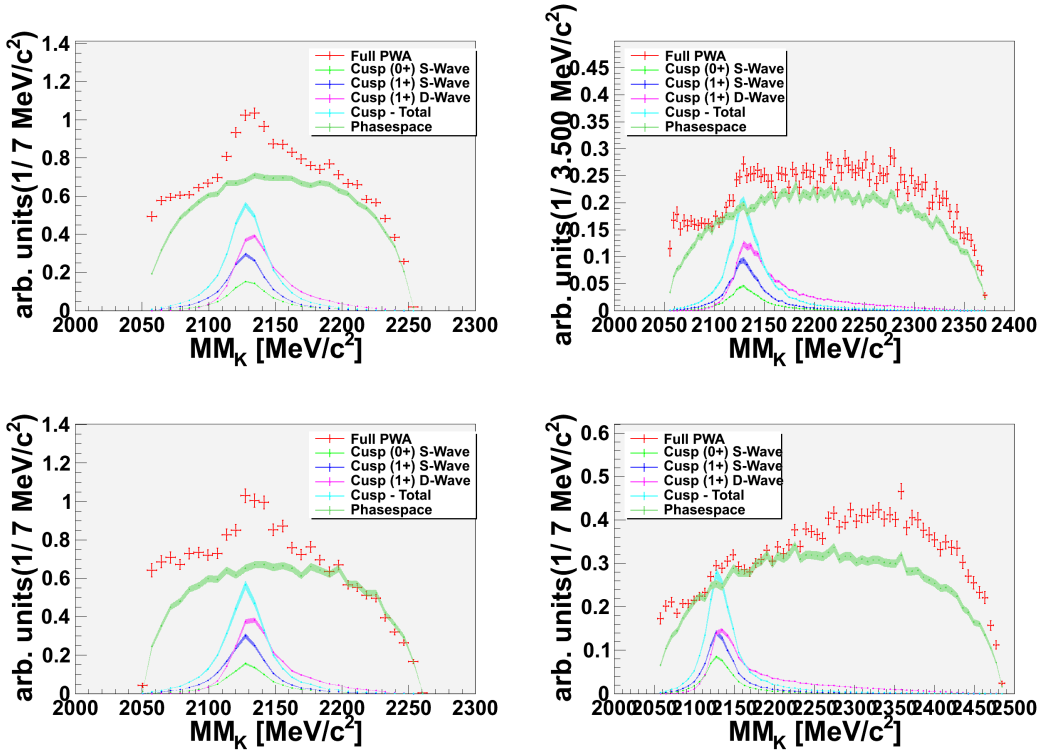

Figure 4.14: Full 4π phase space extrapolation plotting from the data sample DISTO@2.14 GeV(left), DISTO@2.5 GeV ,COSY-TOF @2.16 GeV and DISTO@2.85 GeV in the missing K^+ mass spectrum. It shows Cusp($J^P = 0^+$) S-wave(light green dots), Cusp($J^P = 1^+$) S-wave(blue dots) and Cusp($J^P = 1^+$) D-wave(pink dots). The full PWA(red dots), total cusp waves(light blue dots) and the phase space(green dots) are also shown. The scales of the partial waves are arbitrary.. For cusp, the Flatté Parametrization is used.

In the Figure 4.14 for each data sample, the phase-space distribution is given by the dark green curve. The three different posible cusp waves are given by light green (0^+ S-wave), blue (1^+ S-wave) and pink (1^+ D-Wave) dots. The coherent sum of all cusp waves is given by the light blue curve. Is can be nicely seen, the shape of the different cups wave do not differ significant for each other and they all show peak structures at NΣ threshold, which play a major role for cusp description.

4.2.3.3 Systematic Scan

Furthermore, the relative Contribution from the mean value of the five best solutions for the different contribution channels the combined analysis with flatté parametrization for the DISTO@2.85 GeV, DISTO @2.5 GeV,DISTO@2.14 GeV and COSY-TOF@2.16 GeV with errors are the standard deviation of the results from the scan are also given.

parameter set	A	B	C	D	E
Loglike value for sample	-63296.418	-63442.202	-63114.128	-63013.038	-62700.441
$pK\Lambda$ (direct)	x	x	x	x	x
$N^*(1650)$	x	x	x	x	x
$N^*(1710)$	x	x	x	x	x
$N^*(1720)$	x	x	-	-	x
$N^*(1875)$	x	x	x	x	-
$N^*(1880)$	x	x	x	x	x
$N^*(1895)$	x	x	x	x	x
$N^*(1900)$	x	-	x	-	-
$pK\Sigma$ (S_0^+-Cusp)	x	x	x	x	x
$pK\Sigma$ (S_1^+-Cusp)	x	x	x	x	x
$pK\Sigma$ (D_1^+-Cusp)	x	x	x	x	x

Table 4.11: Inclusion table for the best five parameters set of the systematical scan of the PWA for the combined analysis with the flatté parametrization. In the the Loglike value and the reduced χ^2 value are given. An included channel in a parameter set is indicated by an x and excluded channel by an -.

In Table 4.8, one can see in details that the inclusion of the $N^*(1720)$, $N^*(1875)$, and $N^*(1900)$ resonances does not strongly alter the quality of the result, which means that these three resonances are not necessary for describing the data set, which is always consistent with other analysis. The details of systematical results are shown in Section B.b.ii.i.

4.2.3.4 Channel Contributions

Furthermore, the relative Contribution from the mean value of the five best solutions for the different contribution channels the combined analysis with flatté parametrization for the DISTO@2.85 GeV, DISTO@2.5 GeV, DISTO@2.14 GeV and COSY-TOF@2.16 GeV with errors are also given.

According to Table 4.12, the realtive strength from the mean value of the five best solutions for the different contribution channels with the standard deviation of the results from the scan. It can be nicely seen, that mainly contributed channels for all four datasets are non-resonant p + K^+ + Λ production and $N^*(1710)$. The $N^*(1650)$ is a mainly contributed channel, but not in case of DISTO@2.5 GeV and DISTO@2.85 GeV. For DISTO@2.14 GeV and COSY-TOF@2.16 GeV, their mainly contributed channels are still the same and take quite large percentage. However, for the DISTO@2.5 GeV, the $N^*(1650)$, $N^*(1880)$ and $N^*(1895)$ also takes non-negligible percentages. Still, what is in common for all three datasets are that $N^*(1720)$, $N^*(1875)$, and $N^*(1900)$ contribute quite small, which also indicate they are not necessary for describing the data set. It is shown here that for DISTO@2.5 GeV and DISTO@2.85 GeV, the channel contributions share the same trend and DISTO@2.14 GeV and COSY-TOF@2.16 GeV looks similar. It might be caused by initial beam energy. The consistency in channel contirbutions shows the stability of PWA analysis by having the trend for relative channel production percentages that one can follow. Base on these solutions, in-

	DI@2.85 GeV	DI@2.5 GeV
$pK\Lambda$ (direct)	$20.88 \pm 4.24 \pm 1.90\%$	$24.39 \pm 4.53 \pm 2.02\%$
$N^*(1650)$	$9.77 \pm 1.97 \pm 0.88\%$	$14.30 \pm 2.68 \pm 1.20\%$
$N^*(1710)$	$24.24 \pm 4.91 \pm 2.20\%$	$27.67 \pm 5.18 \pm 2.32\%$
$N^*(1720)$	$2.17 \pm 0.47 \pm 0.27\%$	$1.90 \pm 0.39 \pm 0.23\%$
$N^*(1875)$	$2.20 \pm 0.42 \pm 0.21\%$	$1.18 \pm 0.26 \pm 0.13\%$
$N^*(1880)$	$15.02 \pm 3.15 \pm 1.41\%$	$10.03 \pm 1.90 \pm 0.85\%$
$N^*(1895)$	$17.05 \pm 3.41 \pm 1.53\%$	$9.38 \pm 1.71 \pm 0.77\%$
$N^*(1900)$	$0.88 \pm 0.21 \pm 0.15\%$	$0.66 \pm 0.13 \pm 0.09\%$
$pK\Sigma$ (S_0^+-Cusp)	$0.3 \pm 0 \pm 0\%$	$0.99 \pm 0 \pm 0\%$
$pK\Sigma$ (S_1^+-Cusp)	$6.87 \pm 1.39 \pm 0.63\%$	$9.44 \pm 0 \pm 0\%$
$pK\Sigma$ (D_1^+-Cusp)	$0.2 \pm 0 \pm 0\%$	$0.2 \pm 0 \pm 0\%$
	DI@2.14 GeV	CO@2.16 GeV
$pK\Lambda$ (direct)	$26.00 \pm 4.53 \pm 2.03\%$	$24.47 \pm 4.37 \pm 1.96\%$
$N^*(1650)$	$25.68 \pm 4.42 \pm 1.98\%$	$26.40 \pm 4.57 \pm 2.05\%$
$N^*(1710)$	$23.90 \pm 4.21 \pm 1.88\%$	$22.85 \pm 4.00 \pm 1.78\%$
$N^*(1720)$	$1.37 \pm 0.32 \pm 0.18\%$	$1.42 \pm 0.31 \pm 0.18\%$
$N^*(1875)$	$0.42 \pm 0 \pm 0\%$	$1.22 \pm 0.10 \pm 0.10\%$
$N^*(1880)$	$4.00 \pm 0.53 \pm 0.24\%$	$2.84 \pm 0.41 \pm 0.20\%$
$N^*(1895)$	$4.16 \pm 0.63 \pm 0.30\%$	$2.94 \pm 0.41 \pm 0.20\%$
$N^*(1900)$	$0.32 \pm 0 \pm 0\%$	$0.61 \pm 0 \pm 0\%$
$pK\Sigma$ (S_0^+-Cusp)	$0.95 \pm 0 \pm 0\%$	$0.92 \pm 0 \pm 0\%$
$pK\Sigma$ (S_1^+-Cusp)	$12.82 \pm 2.21 \pm 1.00\%$	$15.33 \pm 2.54 \pm 1.15\%$
$pK\Sigma$ (D_1^+-Cusp)	$0.2 \pm 0 \pm 0\%$	$0.2 \pm 0 \pm 0\%$

Table 4.12: Relative Contribution from the mean value of the five best solutions for the different contribution channels the combined analysis with flatté parametrization for the DISTO2.85 GeV, DISTO@2.5 GeV, DISTO@2.14 GeV and COSY-TOF@2.16 GeV. And errors are average fitting error and the standard deviation of the results from the five best solutions.

cluding all possible channels, a systematical scan, which varies the combined of included N^* resonance war performed. All systematic error is below 10%.

The cusp related values from five best solutions with their systematic errors are shown in Table 4.13.

The two coupling constants values are in compatiable order and it is quite different from the results of three data analysis with quite small NΣ coupling constants. As later probes turn out, if one changes the starting values of coupling constants, the similar results with three data samples can also appear. The temporary conclusion is, even for combined data analysis, there is still ambiguities in the values of coupling constants that can not be eliminated. One way to solve might be calculating the scattering length of NΣ interaction by using the values of coupling constants in Flatté and compare the the theoretical expectations to rule out possibilities.

Systematical Scan	$g_{N\Sigma}$	$g_{p\Lambda}$	$m_r(GeV/c^2)$
A	$1.55 \pm 0.08 \times 10^{-2}$	$0.302 \pm 0.003 \times 10^{-2}$	2.130 ± 0.006
B	$1.67 \pm 0.07 \times 10^{-2}$	$0.428 \pm 0.001 \times 10^{-2}$	2.131 ± 0.007
C	$1.58 \pm 0.06 \times 10^{-2}$	$0.431 \pm 0.002 \times 10^{-2}$	2.130 ± 0.006
D	$1.67 \pm 0.07 \times 10^{-2}$	$0.427 \pm 0.002 \times 10^{-2}$	2.127 ± 0.007
E	$1.57 \pm 0.07 \times 10^{-2}$	$0.310 \pm 0.002 \times 10^{-2}$	2.131 ± 0.007

Table 4.13: Coupling constants for the best five parameters set of the systematical scan of the PWA for the combined analysis with the flatté parametrization.

The coupling constants for pΛ and NΣ can be calulated using functions in Appendix A.e that $g_{N\Sigma} = 2.61 \pm 0.07 \times 10^{-2} \pm 0.031$, $g_{p\Lambda} = 0.380 \pm 0.002 \times 10^{-2} \pm 0.006$ and the threshold mass $m_r = 2.1298 \pm 0.0066 \pm 0.0030(GeV/c^2)$ with the first error from the propagated errror of the signle systematic fitting and second error from the standard deviation of the five values. The calculated scattering length for NΣ (Section 1.4) is $a_{N\Sigma} \approx (0.637 - i0.1453)fm$. In this time, the coupling constant for NΣ is larger than pΛ .

4.2.4 Summary of Combined Data Analysis

First of all, the combined data analysis of PWA analysis give a nice agreement with experimental data, especially can reproduce quite nicely with a Flatté -like paramtezied Cusp waves. The fitting results of BG-PWA converges with negative Log-likelihood value and small χ^2 /ndf values.

Secondly, as one point of view is that, since the symmetric Breit-Wigner parametrization already gives a good explanation of the experimental data, so it is expected the $g_{p\Lambda} \gg g_{N\Sigma}$, which would lead to a symmetric structure of the flatté function. But there is still ambiguities in the values of coupling constants that can not be eliminated. One way to solve is to use combined data analysis.

The realtive strength of all contribution channels are listed with the fitting error, obtained from the PWA. It can be nicely seen, that all datasets are that $N^*(1720)$, $N^*(1875)$, and $N^*(1900)$ contribute quite small, which also indicate they are not necessary for describing the data set. It is shown here that for DISTO@2.5 GeV and DISTO@2.85 GeV, the channel contributions share the same trend and DISTO@2.14 GeV and COSY-TOF@2.16 GeV looks similar. It might be caused by initial beam energy. The consistency in channel contirbutions shows the stability of PWA analysis by having the trend for relative channel production percentages that one can follow. All systematic error is below 10%.

The scattering length for NΣ can be calculated as $\approx (5.88 \times 10^{-4} - i0.535 \times 10^{-2})fm$ for three data analysis of DISTO@2.5 GeV,DISTO@2.14 GeV and COSY-TOF@2.16 GeV. One reason for this small value may be due to the small coupling constants of pΣ . By adding another data sample DISTO@2.85 GeV to the combined data analysis, it is $\approx (0.637 - i0.1453)fm$. In this time, the coupling constant for NΣ is larger than pΛ .

Chapter V

Summary and Outlook

5.1 Summary

The present work is dedicated to the PWA analysis of the exclusive events of proton proton experiment from various collaborations. The main work is focused on describing the NΣ cusp phenomenon, which appears in the experimental data, by using Flatté paramaterization on BG-PWA Framework. From theoretical interpretation, it could be a cusp structure due to (and at) the opening of the NΣ threshold and then would be a signal for an inelastic virtual state or due to a bound pΣ^0or nΣ^+ state, i. e. a deuteron-like but unstable bound state. In the latter case the peak of the cross section has to be below the NΣ threshold. In principle, it could also be a pΛ resonance above the NΣ threshold.

The first part of work is single data analysis, only one data sample is analyzed each time. The PWA analysis give a nice agreement with experimental data for various datases, especially the cusp phnomenon is parametrized by Flatté parametrization. Besides, the shape of cusp partial waves with quamtum number $J^P = 0^+$ or 1^+ and contributions of various production channels are also checked. Additonally, A sysmetic scan of different possibilites of combinations for pΛ and NΣ coupling constants is done to crosscheck if Flatté parametrization is implemented correctly. And to rule out ambiguities of the results, a scan for the inclusion of N^* resonances was performed based on the solution extract for COSY-TOF@2.16 GeV data sample.

However, it can be seen that the PWA results obtained for a single energy are not unique between several data sets. The results ambiguity also means that it is not expected for further systematical scans for other single energy BG-PWA result to yield much useful information. Even though the systematical scan is useful to get a handle on systematical uncertainties of the analysis and to check the stability of the result, it shows the difficulty of making quantitative statements about the reaction using only one data set at a single energy.

The second part of work is combined data analysis, to rule out the ambiguities appear for single data analysis. It was done for two datasets, three datasets and four datasets, separately. The PWA analysis also give a nice agreement with experimental data, especially the cusp phnomenon is parametrized by Flatté parametrization, with minor discrepancies. The sysmetic scan of N^* resonances have a high consistency, which shows the stability of

PWA results. The realtive strength of all contribution channels shows that all datasets are that $N^*(1720)$, $N^*(1875)$, and $N^*(1900)$ contribute quite small, which also indicate they are not necessary for describing the data set. It is shown here that for DISTO @2.5 GeV and DISTO @2.85 GeV, the channel contributions share the same trend and DISTO@2.14 GeV and COSY-TOF@2.16 GeV looks similar. The consistency in channel contirbutions shows the stability of PWA analysis by having the trend for relative channel production percentages that one can follow. All systematic errors are below 10%. The scattering length for NΣ can be calculated as $\approx (5.88\times10^{-4} - i0.535\times10^{-2})fm$ for three data analysis. One reason for this small value may be due to the small coupling constants of pΣ . It is $\approx (0.637 - i0.1453)fm$ for four data samples. In this time, the coupling constant for NΣ is larger than pΛ .

5.2 Outlook

The NΣ cusp phenomenon was at the beginning analyzed with Breit-Wigner parametrization, which indicates that the cusp has symmetric shape. In Flatté parametrization, this means the coupling constant for NΣ is quite smaller than pΛ . This result proves itself in BG-PWA analysis in this work. However, many probes also show it is not the unique solution up to now.

What is quite interesting is that the calculation of scattering length of NΣ interaction, whose results could be compared with many theoretical results calculated from various theoretical models. And it may help to distinguish the proper coupling constants for pΛ and NΣ in Flatté parametrization, which also leads to the physical explanation of the NΣ cusp phenomenon. The next steps for an analysis would be, for example adding further data samples of HADES and FOPI to check for consitency in of the N^* contributions.

Appendix A

A.a The Observables

Before fitting the experimental data samples with the BG-PWA, they are compared to the phase-space simulation data. In order to allow a comparison of the experimental and the simulated data, a set of observables is needed, which describes the kinematics of the reaction process. The missing mass spectrum for particles proton, Λ and K^+ is expected to be consistent with the invarianct mass spectrum of two-particle-subsystem (Λ ,K^+), (p,K^+) and (p,Λ), which are directly determined by their each total four momentum. It is true if data are refitted [23]. Since the reaction events fulfill the energy and momentum conservation, it is not necessary to plot the invariant and missing mass spectra at the same time. So only missimg mass spectrums are shown later in the following chapters.

Besides, to provide more information of kinematics of particles detected, the center-of-mass angle in Figure A.1, the Helicity angle in Figure A.2 and the Gottfried-Jackson angle frameworks in Figure A.3 are used as the second kind of plots in the results. The shown mass distributions and angles observables together give a full description of the reaction and offer a good evidence for comparision of experimental results with theoretical predictions.

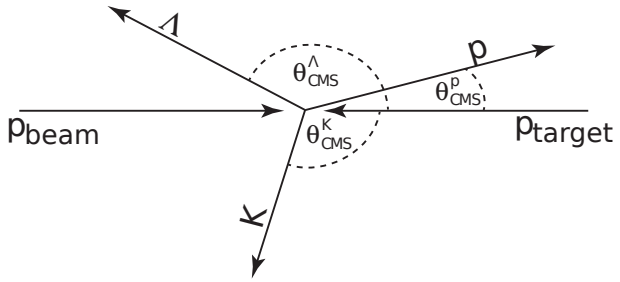

Figure A.1: Schematic of Center of Mass Angle. Center of Mass Angle: Angle between primary proton as the final state particle in the rest frame of the initial protons.

The center of mass angle spectrum shows the distribution of the polar angle of one of the three particle in the center of mass reference frame of the two initial protons. In the case of an isotropic production, it is independent from the different production mechanisms.

In reactions with three particles in the final state, the Helicity angle θ^{RFBC}_{AB} is defined as the angle between the particles A and B in the Helicity frame of the particles B and C.

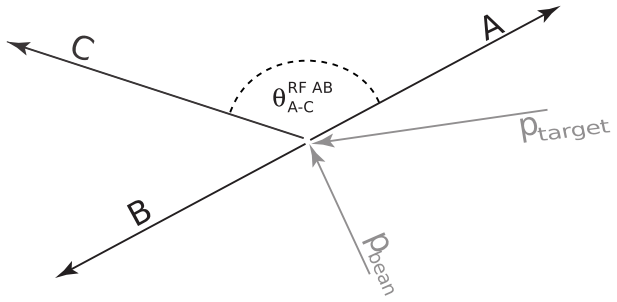

Figure A.2: Schematic of Helicity Angle. Center of Mass Angle: Helicity angle Θ^{RFAB}_{A-C} between particle A and B in the reference system of particles A and B.

This frame is defined as the Lorentz frame in which the center of mass of the particles B and C is at rest [10]. Since the Helicity angle is defined by the three final state particles, it is in fact a special projection of the Dalitz plot. In this representation, the non-resonant production channel of p + K^++ Λ shows a completely flat behaviour in all three distributions. On the contrary, the production channel via intermediate resonances show clear asymmetric structures. The resonances only show a flat behaviour in the distribution in the reference system of its decay particles. This is based on the assumption of an isotropic decay of those resonances.

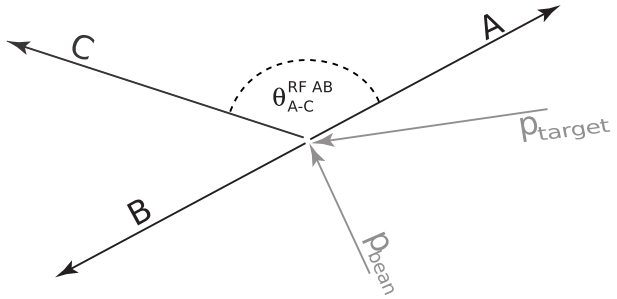

Figure A.3: Schematic of Gottfried Jackson. Gottfried Jackson angle Θ^{RFAB}_{A-p} between particle A and the initial proton in the Reference System of particles A and B.

The Gottfried-Jackson angle $\theta^{RFAB}_{A,Be}$ is defined as the angle between the particle A and the incoming proton in the Jackson frame of the particles A and B, which is the same like the Helicity frame of the particles A and B. This angle connects the exit and entrance channel and carries information, which are not accessible by a Dalitz plot analysis. The utility of the Jackson angle, according to the OBE, reduces the three particle production process to a '2→2' production mechanism happening in the Vertex B in the Feynman diagrams in Figure 1.3. Thus the angular distribution can give information about the relative angular momentum involved [10].

A.b Phase Space Comparison-DISTO

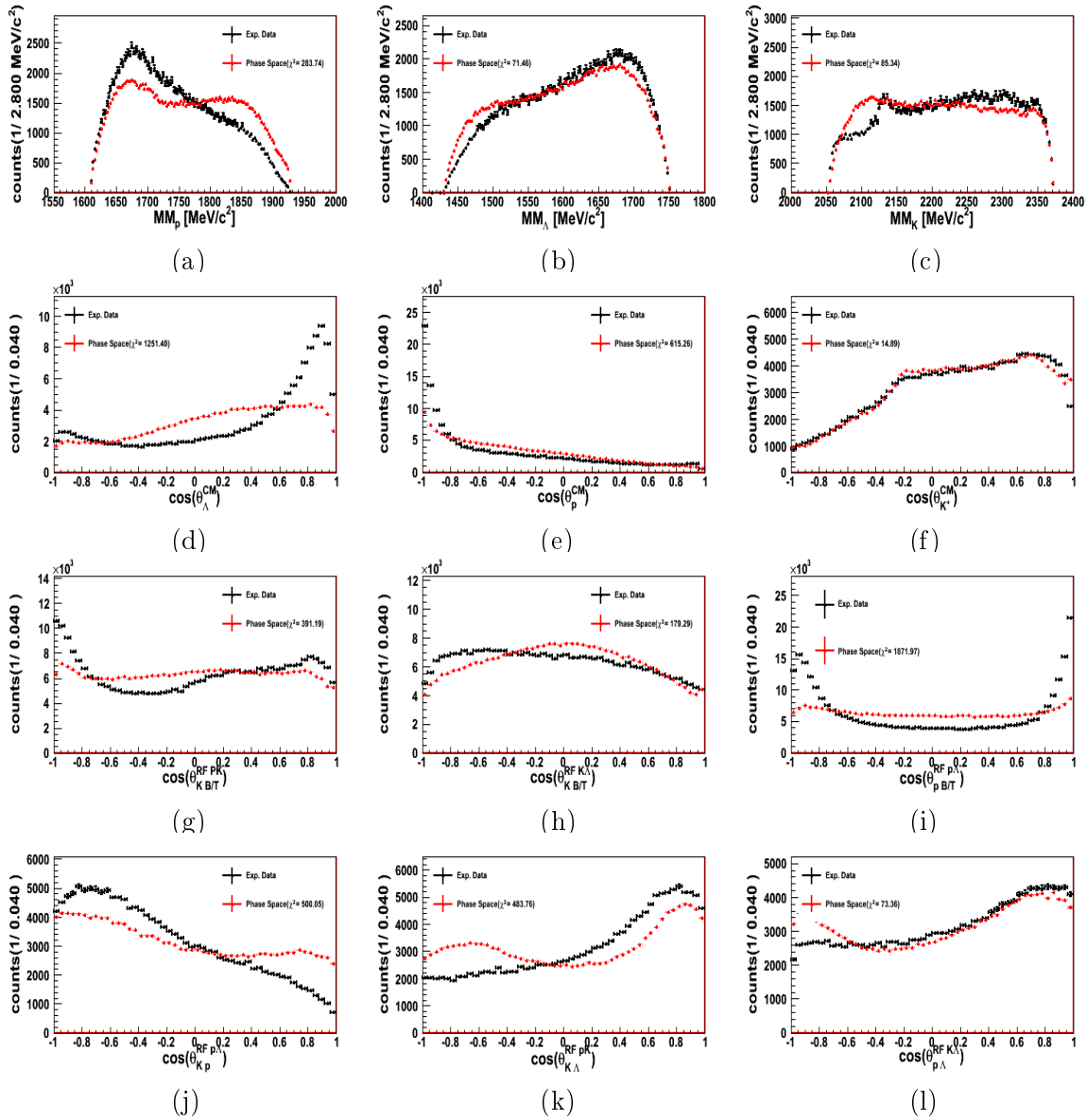

Figure A.4: Comparison of experimental data (black dots) from the data sample DISTO@unit2.5GeV with phase space simulation (red dots). The plot show the Missing Mass MM_p (a), MM_λ(b) and MM_K (c), the Center-of-mass distribution ($cos\left(\theta_{cms,X}\right)$) of the Λ (d), Proton (e) and Kaon (f), the Gottfried-Jackson distributioncos $\left(\theta^{RFpK}_{KB/T}\right)$ (g),cos $\left(\theta^{RFK\lambda}_{KB/T}\right)$ (h),cos $\left(\theta^{RFp\Lambda}_{pB/T}\right)$ (f) and the Helicity angles cos $\left(\theta^{RFp\lambda}_{Kp}\right)$ (j),cos $\left(\theta^{RFpK}_{K\lambda}\right)$ (k) cos $\left(\theta^{RFK\lambda}_{K\lambda}\right)$ (l).

A.c Phase Space Comparison-COSY-TOF

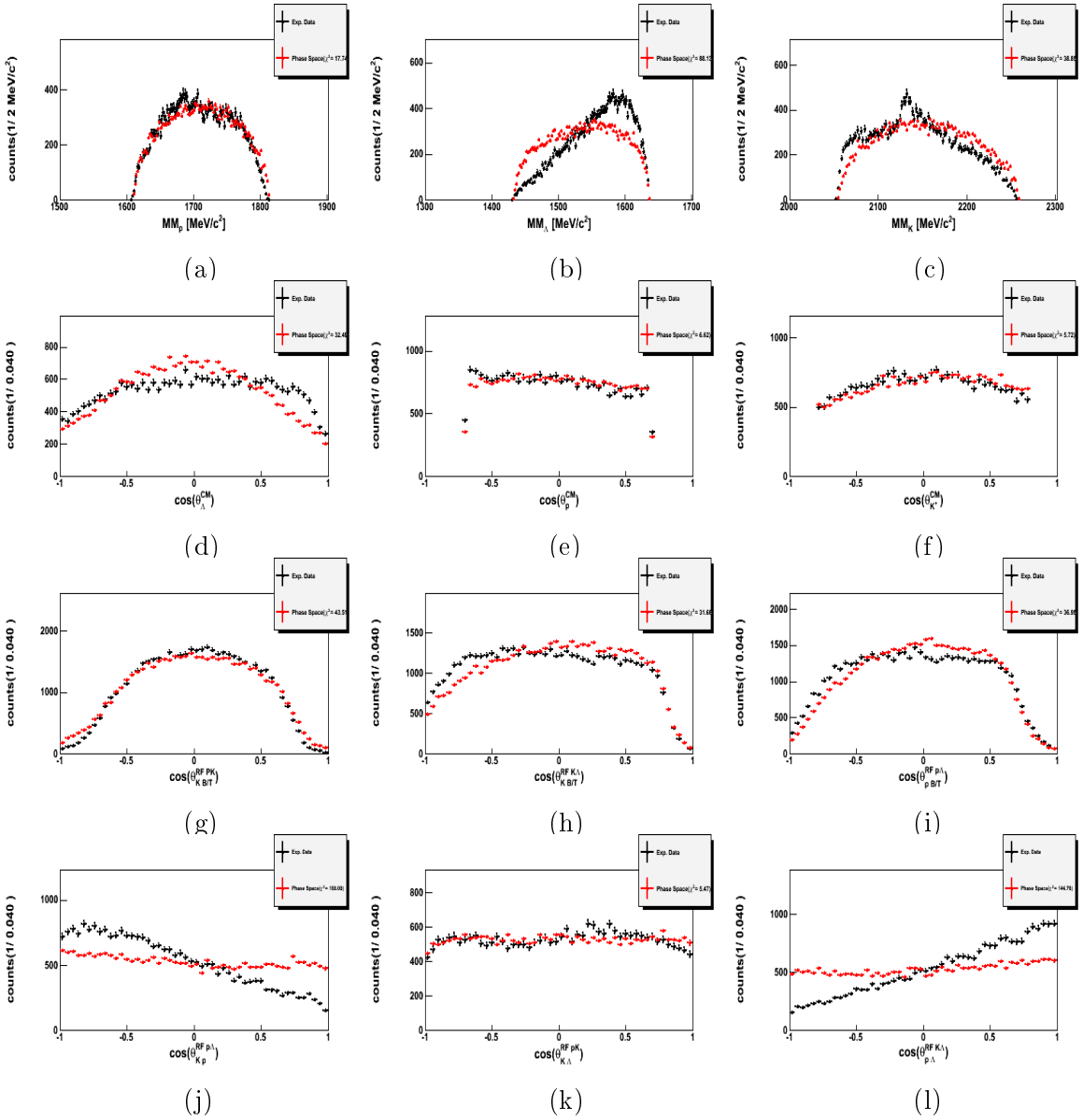

Figure A.5: Comparison of experimental data (black dots) from the data sample COSY-TOF 2.16 GeV with phase space simulation (red dots). The plot show the Missing Mass MM_p (a), MM_λ(b) and MM_K (c), the Center-of-mass distribution ($cos\left(\theta_{cms,X}\right)$) of the Λ (d), Proton (e) and Kaon (f), the Gottfried-Jackson distributioncos $\left(\theta^{RFpK}_{KB/T}\right)$ (g),cos $\left(\theta^{RFK\lambda}_{KB/T}\right)$ (h),cos $\left(\theta^{RFp\Lambda}_{pB/T}\right)$ (f) and the Helicity angles cos $\left(\theta^{RFp\lambda}_{Kp}\right)$ (j),cos $\left(\theta^{RFpK}_{K\lambda}\right)$ (k) cos $\left(\theta^{RFK\lambda}_{K\lambda}\right)$ (l).

There are hard cuts in the spectrum for COSY-TOF@2.16 GeV. There is a difference in the description of the trigger efficiency in the simulation framework compared to the exper-

iment [15], so in the certain region the angular distribution can not be described by PWA. To allow a proper description of the experimental data by the PWA, the region is not taken into account for the analysis. In detail the following cuts are applied: $|cos\theta_{p,cms} < 0.7|$ and $|cos\theta_{K,cms} < 0.7|$

A.d PWA with Breit-Wigner

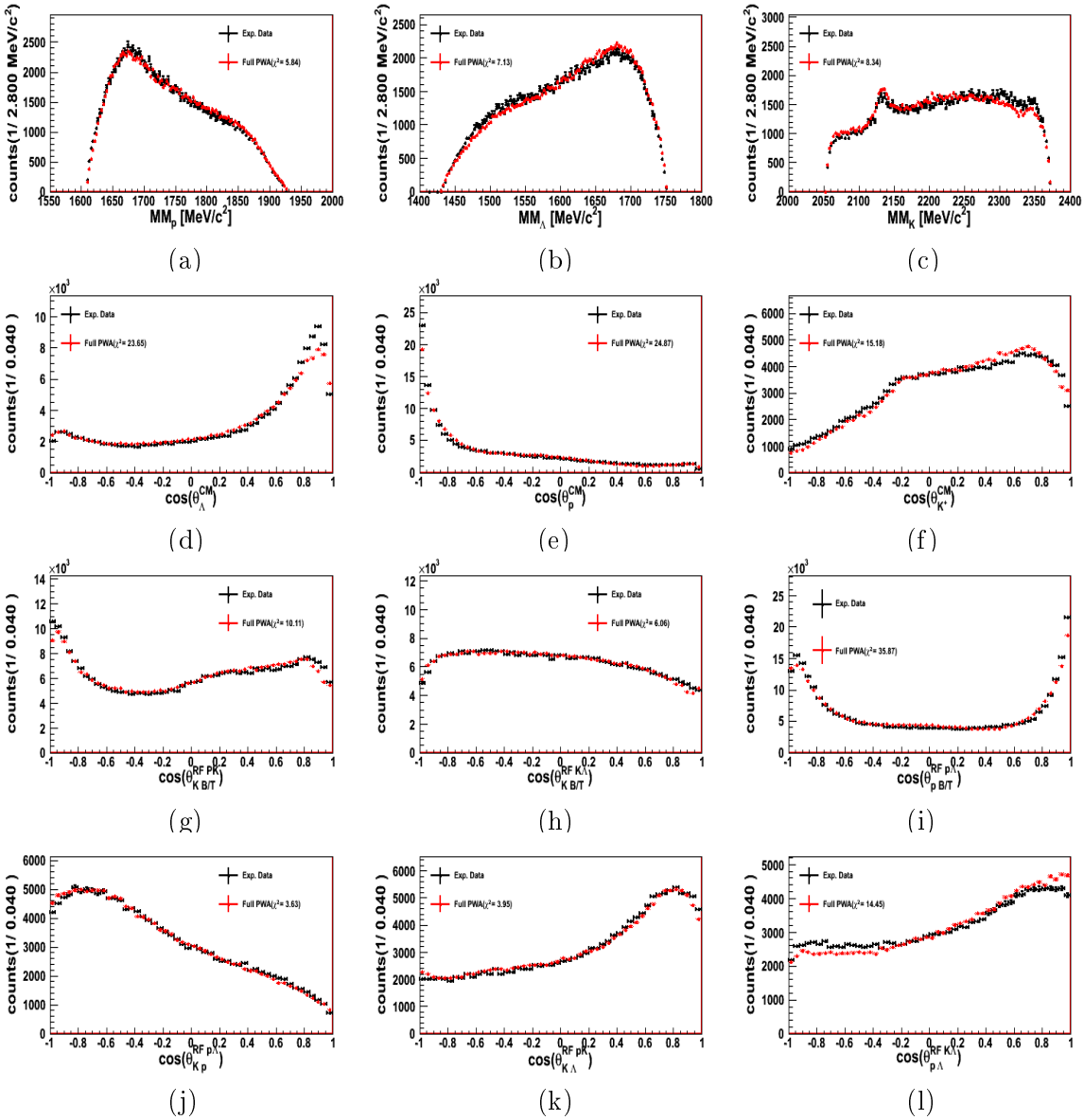

Figure A.6: Comparison of experimental data (black dots) from the data sample DISTO@2.5 GeV with the results from the Partial Wave Analysis (red dots).. Results are obtained from fitting the single data set. The plot show the Missing Mass MM_p (a), MM_λ(b) and MM_K (c), the Center-of-mass distribution ($cos\left(\theta_{cms,X}\right)$) of the Λ (d), Proton (e) and Kaon (f), the Gottfried-Jackson distributioncos $\left(\theta^{RFpK}_{KB/T}\right)$ (g),cos $\left(\theta^{RFK\lambda}_{KB/T}\right)$ (h),cos $\left(\theta^{RFp\Lambda}_{pB/T}\right)$ (f) and the Helicity angles cos $\left(\theta^{RFp\lambda}_{Kp}\right)$ (j),cos $\left(\theta^{RFpK}_{K\lambda}\right)$ (k) cos $\left(\theta^{RFK\lambda}_{K\lambda}\right)$ (l).

A.e g-value

Systematical Scan	g
A	$a + \Delta a$
B	$b + \Delta b$
C	$c + \Delta c$
D	$d + \Delta d$
E	$e + \Delta e$

Table A.1: Coupling constants for the best five parameters set of the systematical scan of the PWA for the combined analysis.

$$g = \overline{g} \pm \sigma_{sys} \pm \Delta_{fitting} \tag{A.1}$$

$$\overline{g} = \frac{\sum a + b + c + d + e}{5} \tag{A.2}$$

$$\Delta_{fitting} = \frac{\sqrt{\Delta a^2 + \Delta b^2 + \Delta c^2 + \Delta d^2 + \Delta e^2}}{5} \tag{A.3}$$

σ_{sys} is average systematic fitting errors.

Appendix B

B.a Single Data Analysis

B.a.i DISTO @2.5 GeV

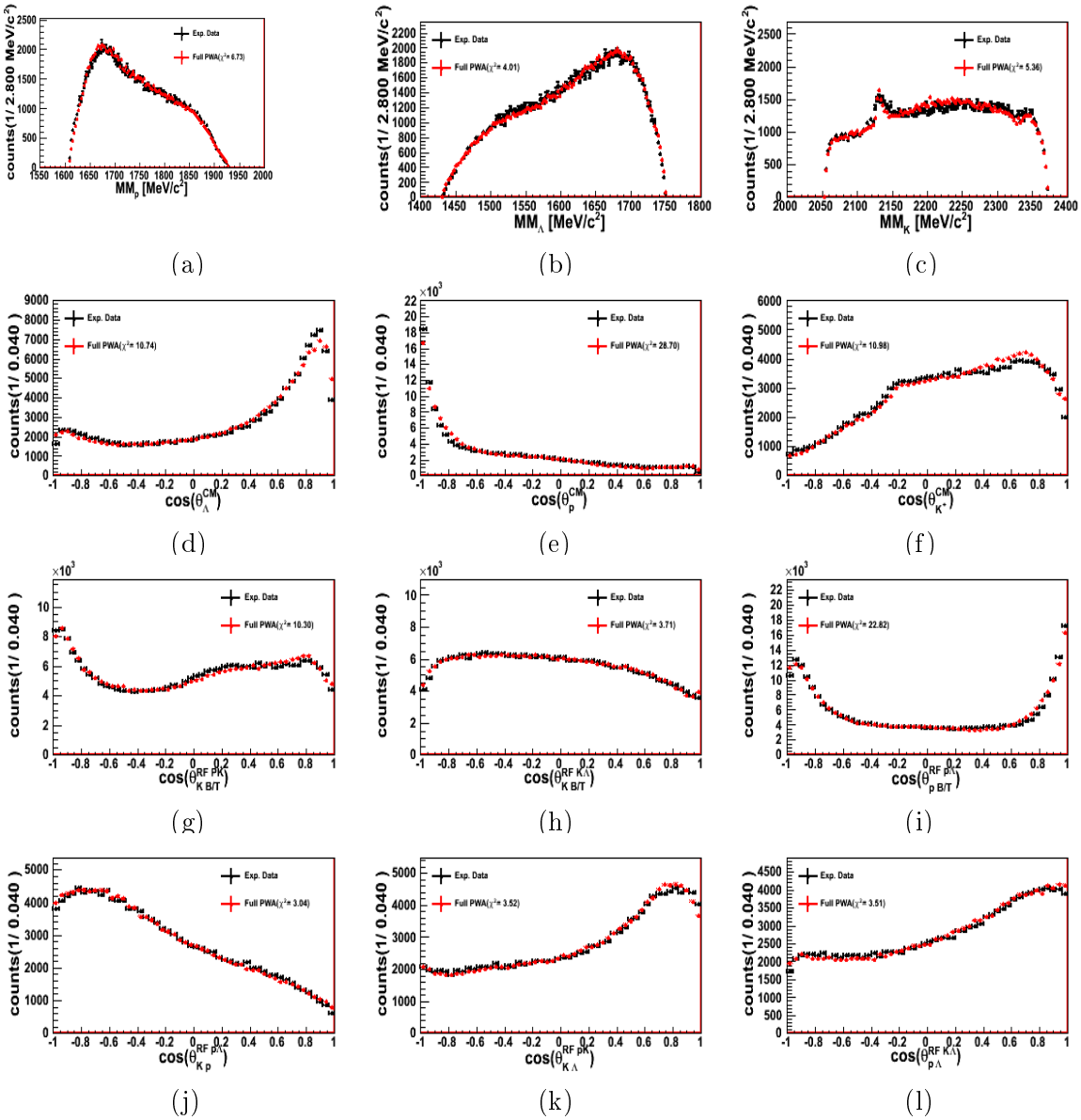

Figure B.1: Comparison of experimental data (black dots) from the data sample DISTO@2.5 GeV with the results from the Partial Wave Analysis (red dots).. Results are obtained from fitting the single data set. The plot show the Missing Mass MM_p (a), MM_λ(b) and MM_K (c), the Center-of-mass distribution ($cos\left(\theta_{cms,X}\right)$) of the Λ (d), Proton (e) and Kaon (f), the Gottfried-Jackson distributioncos $\left(\theta^{RFpK}_{KB/T}\right)$ (g),cos $\left(\theta^{RFK\lambda}_{KB/T}\right)$ (h),cos $\left(\theta^{RFp\Lambda}_{pB/T}\right)$

B.a.ii DISTO @2.14 GeV

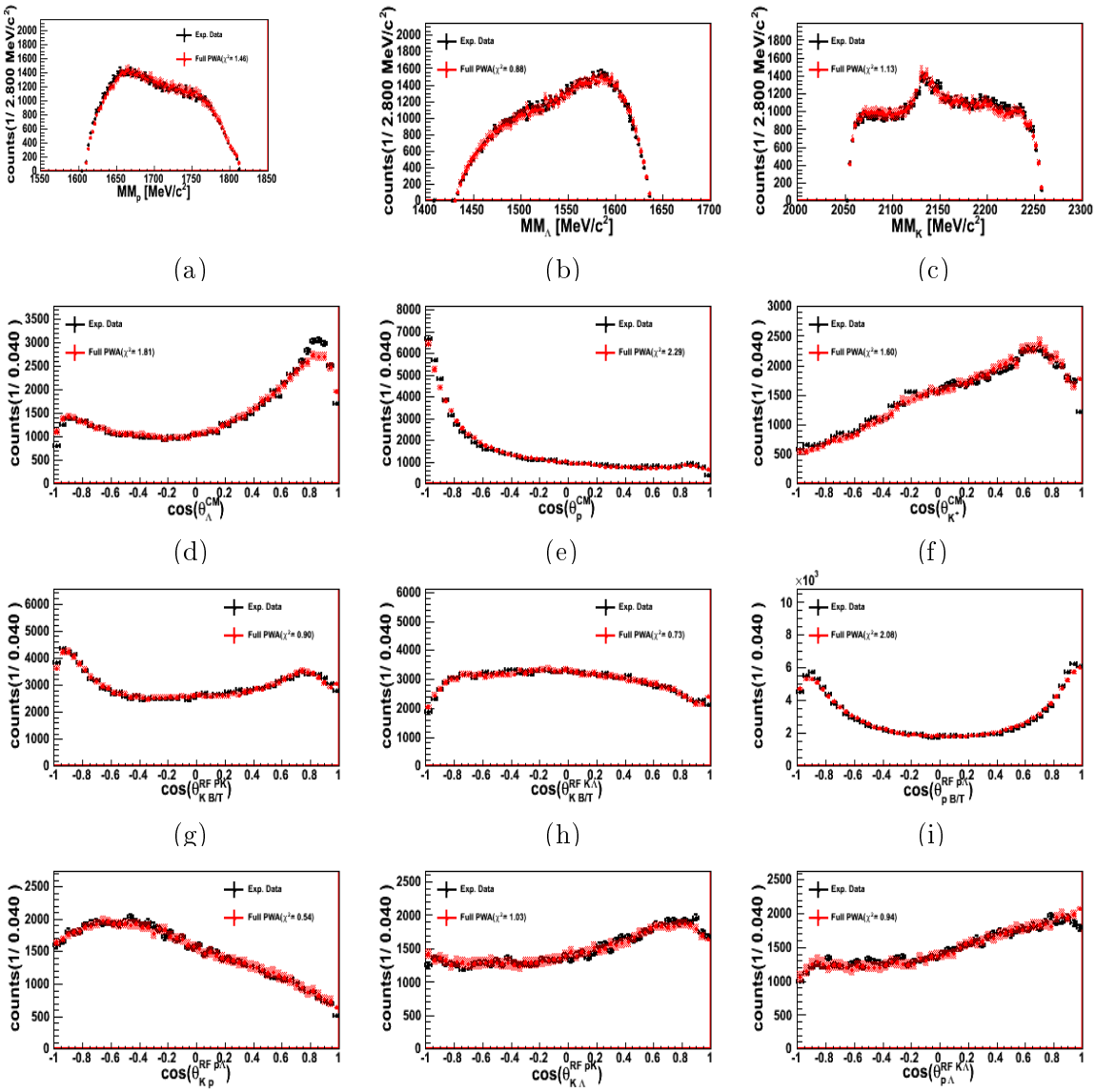

Figure B.2: Comparison of experimental data (black dots) from the data sample DISTO@2.14 GeV with the results from the Partial Wave Analysis (red dots).. Results are obtained from fitting the single data set. The plot show the Missing Mass MM_p (a), MM_λ(b) and MM_K (c), the Center-of-mass distribution ($cos\left(\theta_{cms,X}\right)$) of the Λ (d), Proton (e) and Kaon (f), the Gottfried-Jackson distributioncos $\left(\theta^{RFpK}_{KB/T}\right)$ (g),cos $\left(\theta^{RFK\lambda}_{KB/T}\right)$ (h),cos $\left(\theta^{RFp\Lambda}_{pB/T}\right)$ (f) and the Helicity angles cos $\left(\theta^{RFp\lambda}_{Kp}\right)$ (j),cos $\left(\theta^{RFpK}_{K\lambda}\right)$ (k) cos $\left(\theta^{RFK\lambda}_{K\lambda}\right)$ (l).

B.a.iii COSY-TOF @2.16 GeV

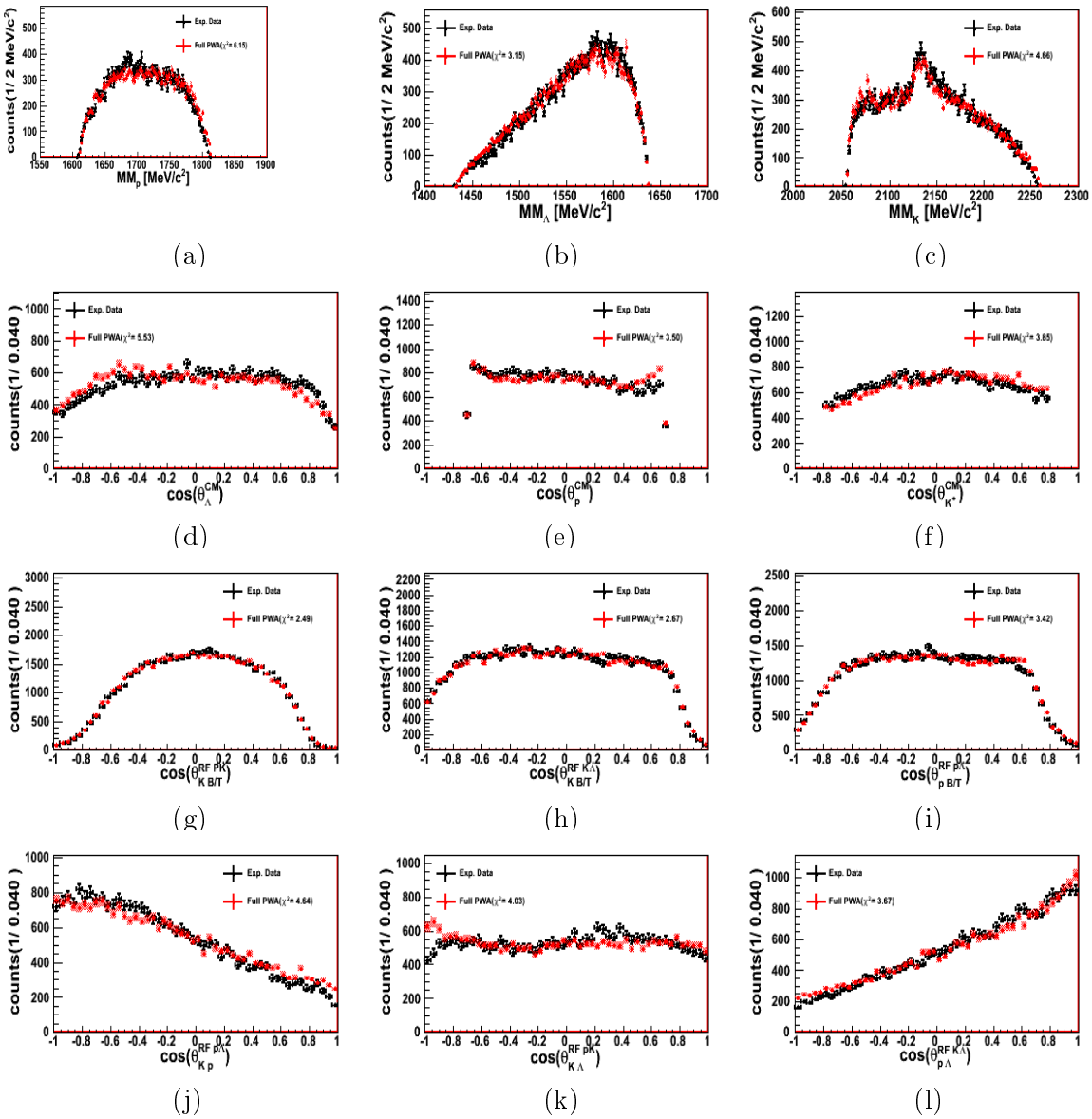

Figure B.3: Comparison of experimental data (black dots) from the data sample COSY-TOF@2.16 GeV with the results from the Partial Wave Analysis (red dots).. Results are obtained from fitting the single data set. The plot show the Missing Mass MM_p (a), MM_λ(b) and MM_K (c), the Center-of-mass distribution ($cos\left(\theta_{cms,X}\right)$) of the Λ (d), Proton (e) and Kaon (f), the Gottfried-Jackson distributioncos $\left(\theta^{RFpK}_{KB/T}\right)$ (g),cos $\left(\theta^{RFK\lambda}_{KB/T}\right)$ (h),cos $\left(\theta^{RFp\Lambda}_{pB/T}\right)$ (f) and the Helicity angles cos $\left(\theta^{RFp\lambda}_{Kp}\right)$ (j),cos $\left(\theta^{RFpK}_{K\lambda}\right)$ (k) cos $\left(\theta^{RFK\lambda}_{K\lambda}\right)$ (l).

B.b Combined Data Analysis

B.b.i DISTO @2.5 GeV+DISTO @2.14 GeV

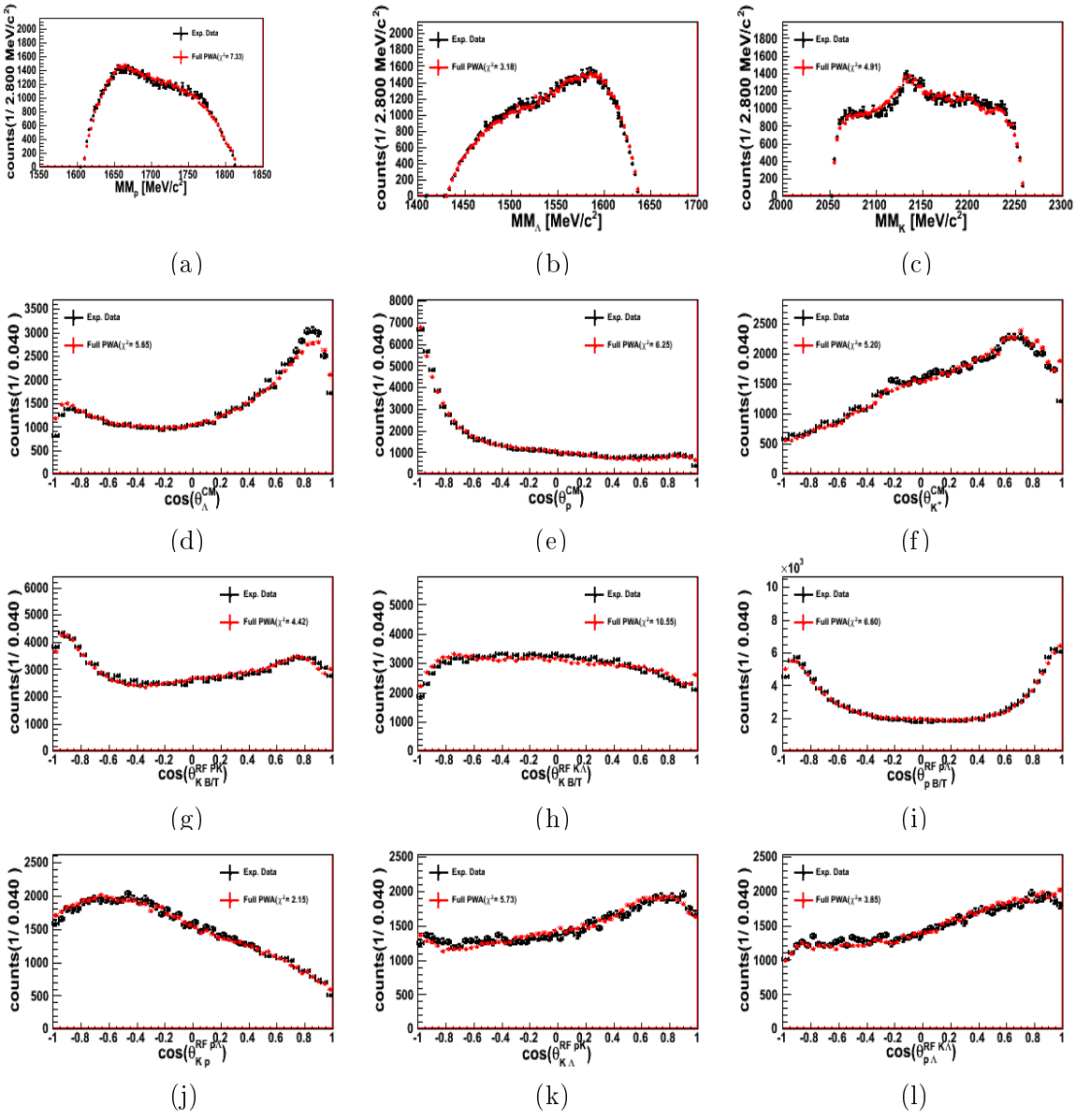

Figure B.4: Comparison of experimental data (black dots) from the data sample DISTO@2.14 GeV with the results from the Partial Wave Analysis (red dots).. Results are obtained from fitting the single data set. The plot show the Missing Mass MM_p (a), MM_λ(b) and MM_K (c), the Center-of-mass distribution ($cos\left(\theta_{cms,X}\right)$) of the Λ (d), Proton (e) and Kaon (f), the Gottfried-Jackson distributioncos $\left(\theta^{RFpK}_{KB/T}\right)$ (g),cos $\left(\theta^{RFK\lambda}_{KB/T}\right)$ (h),cos $\left(\theta^{RFp\Lambda}_{pB/T}\right)$ (f) and the Helicity angles cos $\left(\theta^{RFp\lambda}_{Kp}\right)$ (j),cos $\left(\theta^{RFpK}_{K\lambda}\right)$ (k) cos $\left(\theta^{RFK\lambda}_{K\lambda}\right)$ (l).

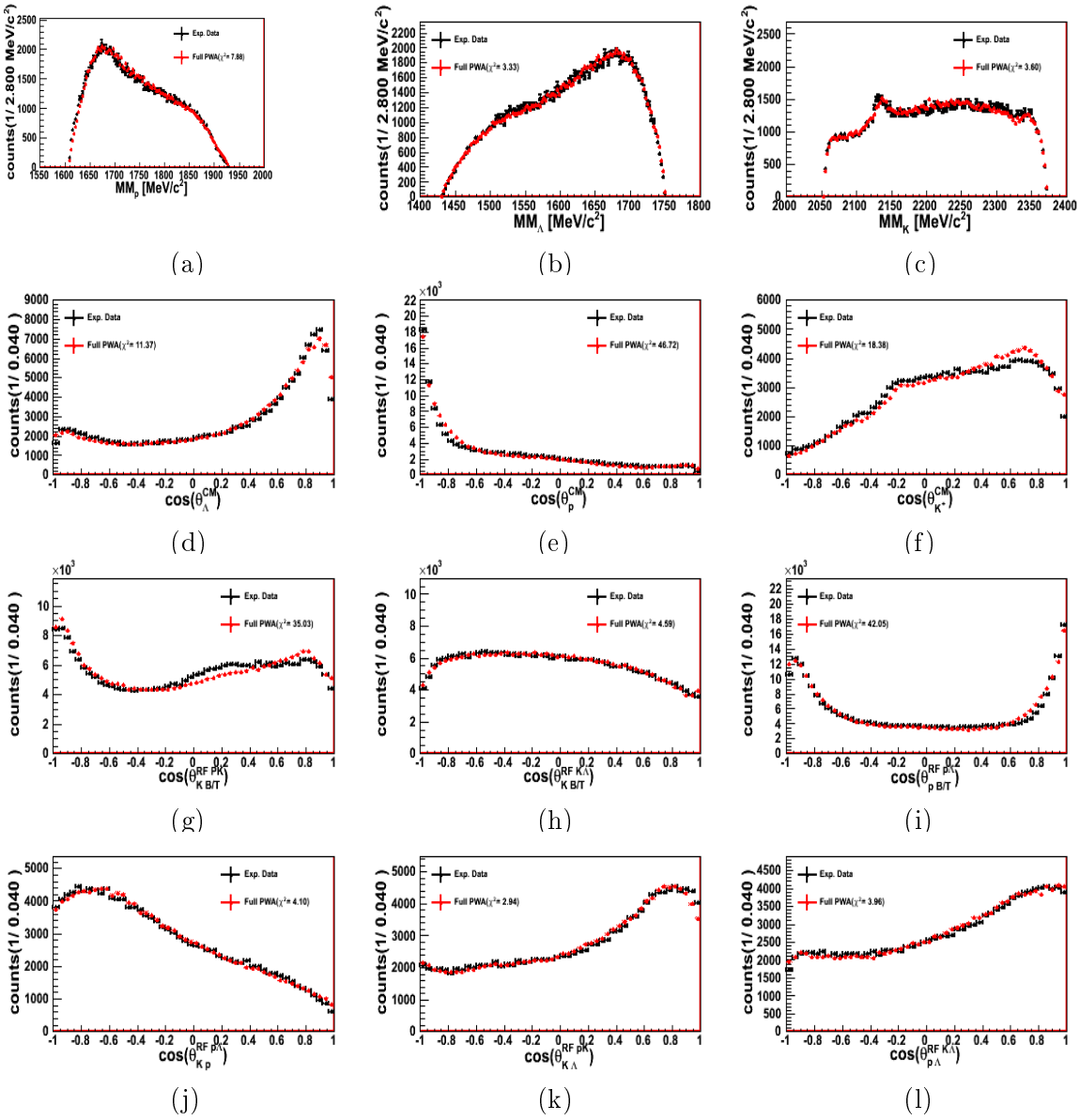

Figure B.5: Comparison of experimental data (black dots) from the data sample DISTO@2.5 GeV with the results from the Partial Wave Analysis (red dots).. Results are obtained from fitting the single data set. The plot show the Missing Mass MM_p (a), MM_λ(b) and MM_K (c), the Center-of-mass distribution ($cos\left(\theta_{cms,X}\right)$) of the Λ (d), Proton (e) and Kaon (f), the Gottfried-Jackson distributioncos $\left(\theta^{RFpK}_{KB/T}\right)$ (g),cos $\left(\theta^{RFK\lambda}_{KB/T}\right)$ (h),cos $\left(\theta^{RFp\Lambda}_{pB/T}\right)$ (f) and the Helicity angles cos $\left(\theta^{RFp\lambda}_{Kp}\right)$ (j),cos $\left(\theta^{RFpK}_{K\lambda}\right)$ (k) cos $\left(\theta^{RFK\lambda}_{K\lambda}\right)$ (l).

B.b.ii DISTO @2.5 GeV+DISTO @2.14 GeV+COSY-TOF @2.14 GeV

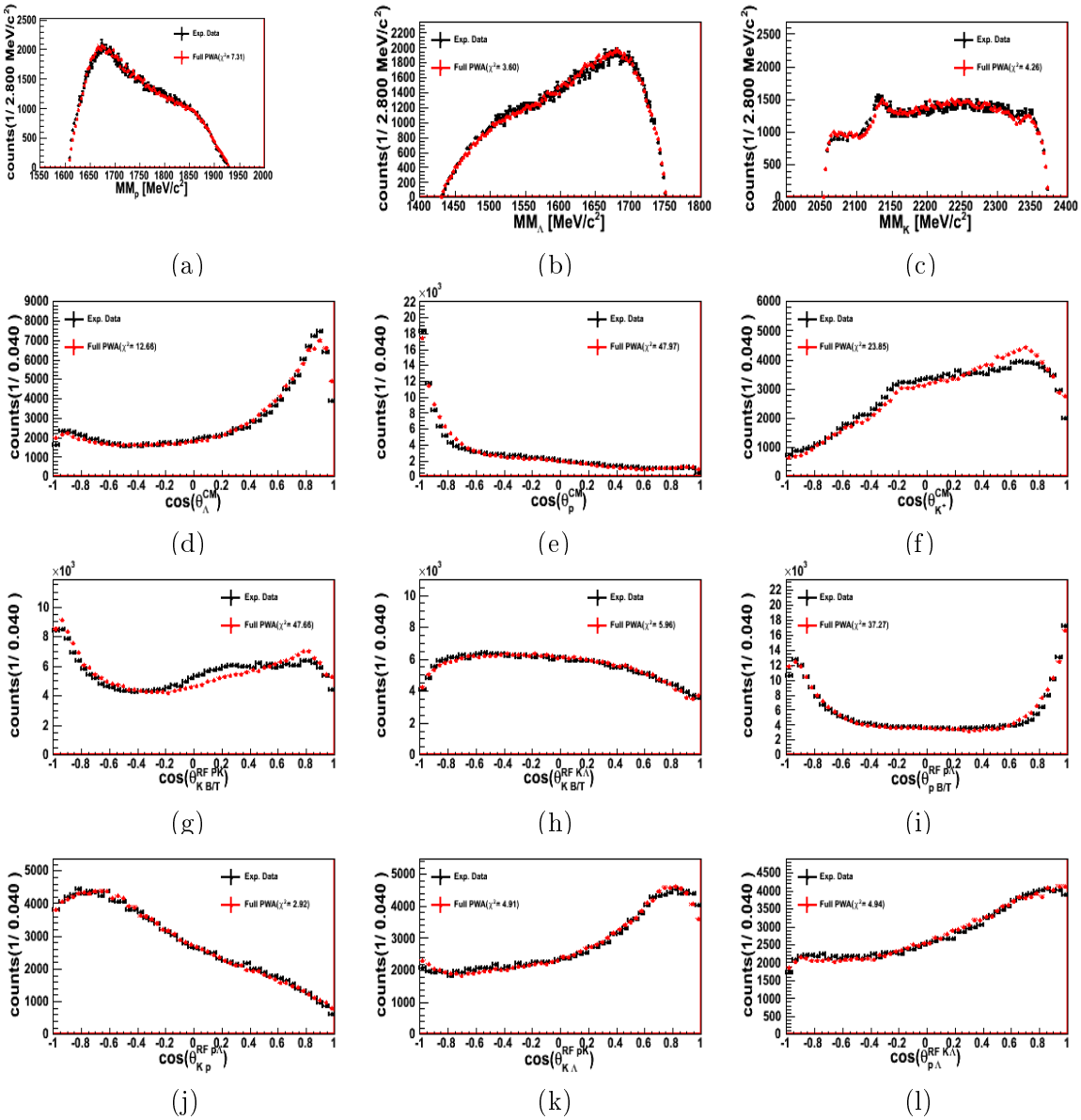

Figure B.6: Comparison of experimental data (black dots) from the data sample DISTO@2.5 GeV with the results from the Partial Wave Analysis (red dots).. Results are obtained from fitting the single data set. The plot show the Missing Mass MM_p (a), MM_λ(b) and MM_K (c), the Center-of-mass distribution ($cos\left(\theta_{cms,X}\right)$) of the Λ (d), Proton (e) and Kaon (f), the Gottfried-Jackson distributioncos $\left(\theta^{RFpK}_{KB/T}\right)$ (g),cos $\left(\theta^{RFK\lambda}_{KB/T}\right)$ (h),cos $\left(\theta^{RFp\Lambda}_{pB/T}\right)$ (f) and the Helicity angles cos $\left(\theta^{RFp\lambda}_{Kp}\right)$ (j),cos $\left(\theta^{RFpK}_{K\lambda}\right)$ (k) cos $\left(\theta^{RFK\lambda}_{K\lambda}\right)$ (l).

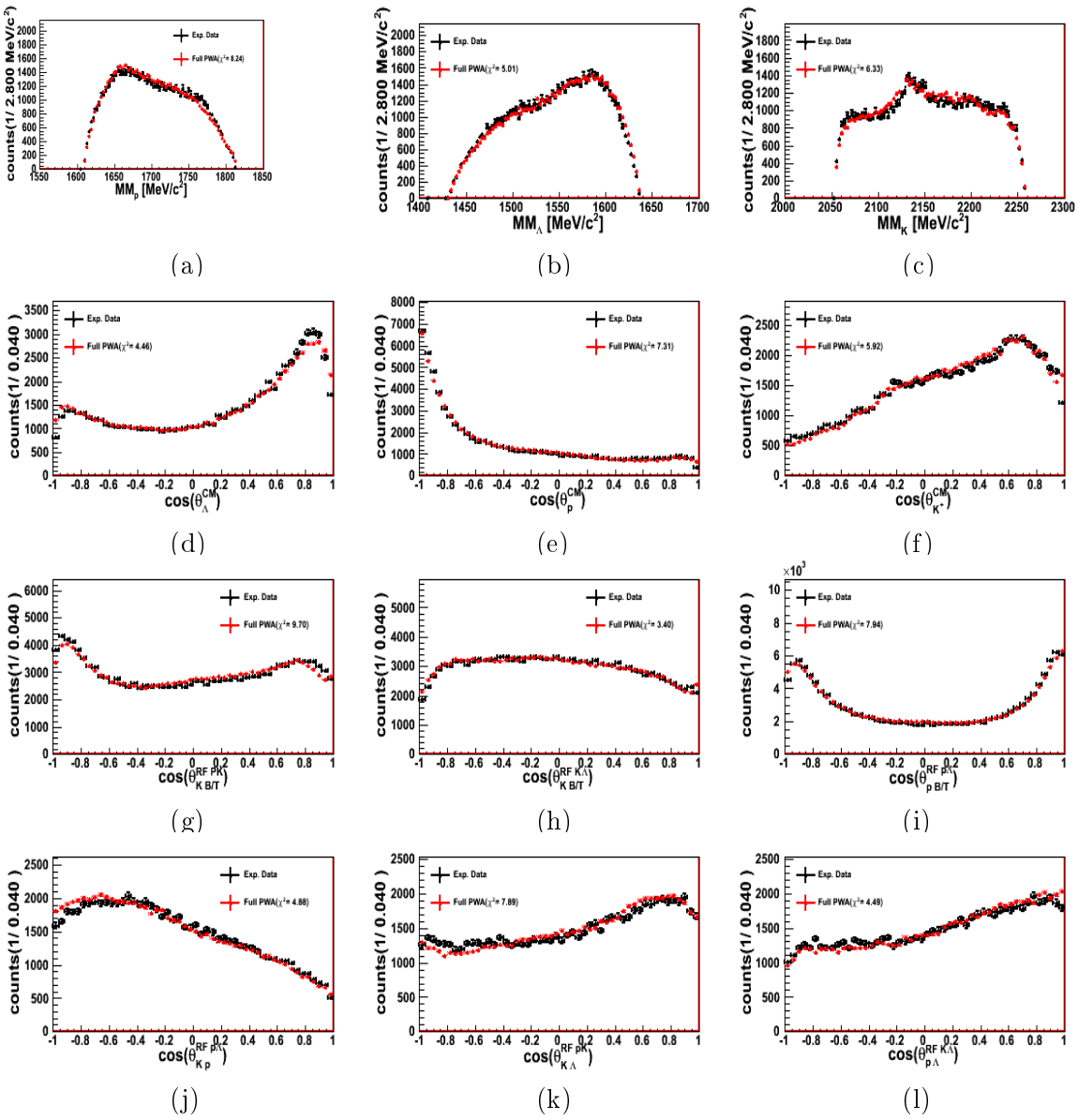

Figure B.7: Comparison of experimental data (black dots) from the data sample DISTO@2.14 GeV with the results from the Partial Wave Analysis (red dots).. Results are obtained from fitting the single data set. The plot show the Missing Mass MM_p (a), MM_λ(b) and MM_K (c), the Center-of-mass distribution ($cos\left(\theta_{cms,X}\right)$) of the Λ (d), Proton (e) and Kaon (f), the Gottfried-Jackson distributioncos $\left(\theta^{RFpK}_{KB/T}\right)$ (g),cos $\left(\theta^{RFK\lambda}_{KB/T}\right)$ (h),cos $\left(\theta^{RFp\Lambda}_{pB/T}\right)$ (f) and the Helicity angles cos $\left(\theta^{RFp\lambda}_{Kp}\right)$ (j),cos $\left(\theta^{RFpK}_{K\lambda}\right)$ (k) cos $\left(\theta^{RFK\lambda}_{K\lambda}\right)$ (l).

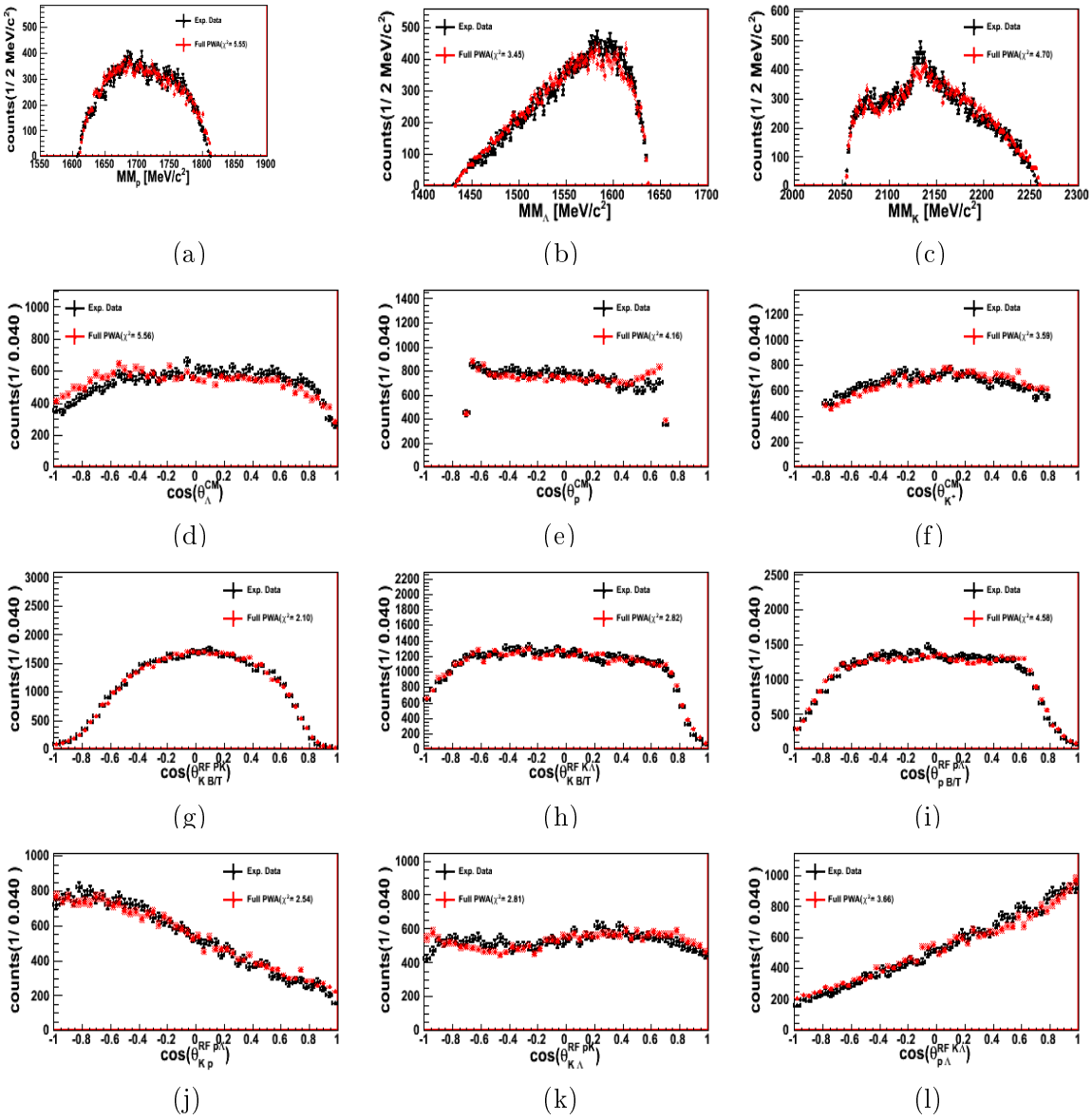

Figure B.8: Comparison of experimental data (black dots) from the data sample COSY-TOF@2.16 GeV with the results from the Partial Wave Analysis (red dots).. Results are obtained from fitting the single data set. The plot show the Missing Mass MM_p (a), MM_λ(b) and MM_K (c), the Center-of-mass distribution ($cos\left(\theta_{cms,X}\right)$) of the Λ (d), Proton (e) and Kaon (f), the Gottfried-Jackson distributioncos $\left(\theta^{RFpK}_{KB/T}\right)$ (g),cos $\left(\theta^{RFK\lambda}_{KB/T}\right)$ (h),cos $\left(\theta^{RFp\Lambda}_{pB/T}\right)$ (f) and the Helicity angles cos $\left(\theta^{RFp\lambda}_{Kp}\right)$ (j),cos $\left(\theta^{RFpK}_{K\lambda}\right)$ (k) cos $\left(\theta^{RFK\lambda}_{K\lambda}\right)$ (l).

B.b.ii.i Systematic Scan

parameter set	A	B	C	D	E
$pK\Lambda$ (direct)	$23.86 \pm 4.06\%$	$23.35 \pm 4.06\%$	$23.35 \pm 4.06\%$	$24.37 \pm 4.57\%$	$24.87 \pm 4.57\%$
$N^*(1650)$	$21.83 \pm 4.06\%$	$27.41 \pm 4.57\%$	$28.43 \pm 5.08\%$	$27.92 \pm 5.08\%$	$27.0 \pm 4.57\%$
$N^*(1710)$	$25.38 \pm 4.57\%$	$21.81 \pm 3.55\%$	$21.83 \pm 4.06\%$	$21.83 \pm 4.06\%$	$22.34 \pm 4.06\%$
$N^*(1720)$	$3.05 \pm 0.51\%$	$3.55 \pm 0.51\%$	$3.05 \pm 0.51\%$	$3.55 \pm 0.51\%$	-
$N^*(1875)$	$0.51 \pm 0\%$	-	$0.51 \pm 0\%$	-	$0.52 \pm 0\%$
$N^*(1880)$	$4.06 \pm 0.51\%$	$4.06 \pm 0.51\%$	$3.55 \pm 0.51\%$	$3.55 \pm 0.51\%$	$5.08 \pm 1.02\%$
$N^*(1895)$	$4.06 \pm 0.51\%$	$4.57 \pm 1.02\%$	$5.08 \pm 1.02\%$	$3.05 \pm 0.51\%$	$5.08 \pm 1.02\%$
$N^*(1900)$	$1.52 \pm 0.51\%$	$1.02 \pm 0\%$	-	-	$1.02 \pm 0\%$
S_0^+-Cusp	$2.54 \pm 0.51\%$	$2.54 \pm 0.51\%$	$2.03 \pm 0.51\%$	$2.54 \pm 0.51\%$	$1.52 \pm 0\%$
S_1^+-Cusp	$12.18 \pm 2.03\%$	$12.69 \pm 2.03\%$	$12.18 \pm 2.03\%$	$12.18 \pm 2.13\%$	$12.69 \pm 2.03\%$
D_1^+-Cusp	$0.1 \pm 0\%$	$0.2 \pm 0\%$	$0.2 \pm 0\%$	$0.2 \pm 0\%$	$0.2 \pm 0\%$

Table B.1: Contribtuion of the included channels in the COSY-TOF@2.16 GeV sample for five parameters set of the systematical scan of the PWA for the combined analysis with the flatté parametrization.

parameter set	A	B	C	D	E
$pK\Lambda$ (direct)	$26.32 \pm 4.74\%$	$25.26 \pm 4.21\%$	$24.74 \pm 4.21\%$	$26.32 \pm 4.74\%$	$26.32 \pm 4.74\%$
$N^*(1650)$	$20.53 \pm 3.68\%$	$25.79 \pm 4.74\%$	$26.84 \pm 4.74\%$	$26.84 \pm 4.74\%$	$25.79 \pm 4.74\%$
$N^*(1710)$	$25.26 \pm 4.74\%$	$22.11 \pm 3.68\%$	$22.63 \pm 4.21\%$	$22.63 \pm 4.21\%$	$22.63 \pm 4.21\%$
$N^*(1720)$	$2.63 \pm 0.53\%$	$3.16 \pm 0.53\%$	$3.16 \pm 0.53\%$	$3.68 \pm 0.53\%$	-
$N^*(1875)$	$0.53 \pm 0\%$	-	$0.2 \pm 0\%$	-	$0.53 \pm 0\%$
$N^*(1880)$	$4.21 \pm 0.53\%$	$4.21 \pm 0.53\%$	$4.21 \pm 0.53\%$	$3.68 \pm 0.53\%$	$5.26 \pm 1.05\%$
$N^*(1895)$	$4.74 \pm 1.05\%$	$5.79 \pm 1.05\%$	$6.32 \pm 1.05\%$	$4.21 \pm 0.53\%$	$6.32 \pm 1.05\%$
$N^*(1900)$	$1.55 \pm 0.53\%$	$1.05 \pm 0\%$	-	-	$1.05 \pm 0\%$
S_0^+-Cusp	$2.63 \pm 0.53\%$	$2.11 \pm 0.53\%$	$1.58 \pm 0.53\%$	$2.11 \pm 0.53\%$	$1.05 \pm 0\%$
S_1^+-Cusp	$11.58 \pm 2.1\%$	$10.53 \pm 1.58\%$	$10.1 \pm 1.58\%$	$10.53 \pm 1.58\%$	$10.53 \pm 2.11\%$
D_1^+-Cusp	$0.2 \pm 0\%$	$0.2 \pm 0\%$	$0.2 \pm 0\%$	$0.2 \pm 0\%$	$0.2 \pm \%$

Table B.2: Contribtuion of the included channels in the DISTO@2.14 GeV sample for five parameters set of the systematical scan of the PWA for the combined analysis with the flatté parametrization.

parameter set	A	B	C	D	E
$pK\Lambda$ (direct)	$22.95 \pm 4.26\%$	$22.40 \pm 4.26\%$	$22.62 \pm 4.26\%$	$23.93 \pm 4.59\%$	$23.61 \pm 4.26\%$
$N^*(1650)$	$10.49 \pm 1.97\%$	$14.10 \pm 2.62\%$	$14.75 \pm 2.62\%$	$14.43 \pm 2.62\%$	$14.10 \pm 2.62\%$
$N^*(1710)$	$29.51 \pm 5.57\%$	$26.56 \pm 4.92\%$	$27.21 \pm 4.92\%$	$27.87 \pm 5.25\%$	$25.57 \pm 4.92\%$
$N^*(1720)$	$3.93 \pm 0.66\%$	$4.26 \pm 0.66\%$	$4.59 \pm 0.98\%$	$5.25 \pm 0.98\%$	-
$N^*(1875)$	$1.3 \pm 0.33\%$	-	$0.66 \pm 0\%$	-	$1.1 \pm 0.33\%$
$N^*(1880)$	$10.3 \pm 1.97\%$	$9.84 \pm 1.97\%$	$9.51 \pm 1.64\%$	$9.51 \pm 1.64\%$	$12.3 \pm 2.30\%$
$N^*(1895)$	$9.18 \pm 1.64\%$	$10.82 \pm 1.97\%$	$11.48 \pm 2.30\%$	$8.85 \pm 1.64\%$	$11.80 \pm 2.30\%$
$N^*(1900)$	$3.28 \pm 0.66\%$	$2.30 \pm 0.33\%$	-	-	$2.30 \pm 0.33\%$
S_0^+-Cusp	$1.97 \pm 0.33\%$	$1.97 \pm 0.33\%$	$1.64 \pm 0.33\%$	$1.64 \pm 0.33\%$	$1.31 \pm 0.33\%$
S_1^+-Cusp	$6.89 \pm 1.31\%$	$7.54 \pm 1.31\%$	$7.21 \pm 1.31\%$	$7.54 \pm 1.31\%$	$7.54 \pm 1.31\%$
D_1^+-Cusp	$0.2 \pm 0\%$	$0.2 \pm 0\%$	$0.2 \pm 0\%$	$0.2 \pm 0\%$	$0.2 \pm 0\%$

Table B.3: Contribtuion of the included channels in the DISTO@2.5 GeV sample for five parameters set of the systematical scan of the PWA for the combined analysis with the flatté parametrization.

B.b.iii DISTO @2.5 GeV+DISTO @2.14 GeV+COSY-TOF @2.14 GeV+DISTO @2.85 GeV

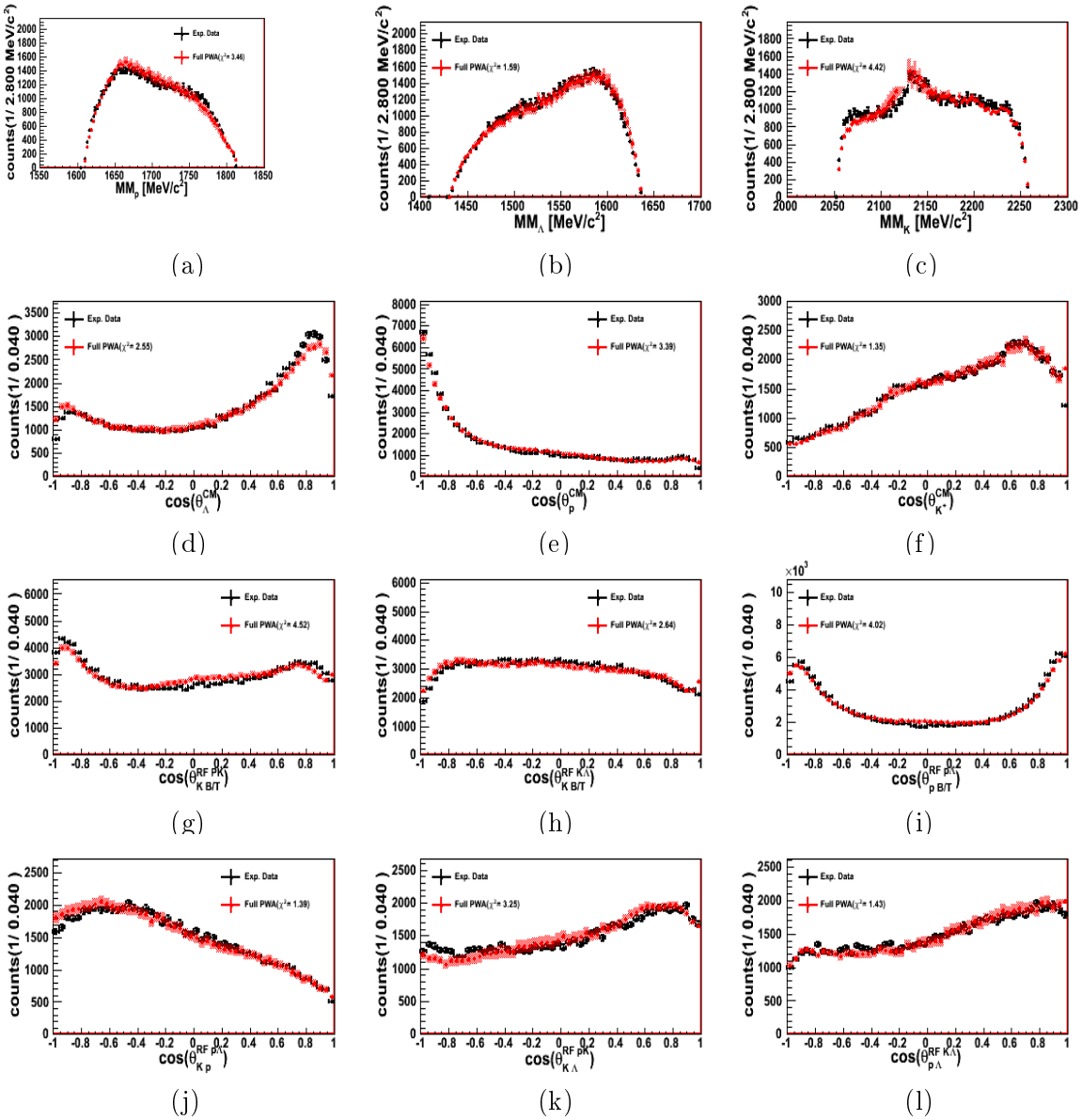

Figure B.9: Comparison of experimental data (black dots) from the data sample DISTO@2.14 GeV with the results from the Partial Wave Analysis (red dots).. Results are obtained from fitting the single data set. The plot show the Missing Mass MM_p (a), MM_λ(b) and MM_K (c), the Center-of-mass distribution ($cos\left(\theta_{cms,X}\right)$) of the Λ (d), Proton (e) and Kaon (f), the Gottfried-Jackson distributioncos $\left(\theta^{RFpK}_{KB/T}\right)$ (g),cos $\left(\theta^{RFK\lambda}_{KB/T}\right)$ (h),cos $\left(\theta^{RFp\Lambda}_{pB/T}\right)$ (f) and the Helicity angles cos $\left(\theta^{RFp\lambda}_{Kp}\right)$ (j),cos $\left(\theta^{RFpK}_{K\lambda}\right)$ (k) cos $\left(\theta^{RFK\lambda}_{K\lambda}\right)$ (l).

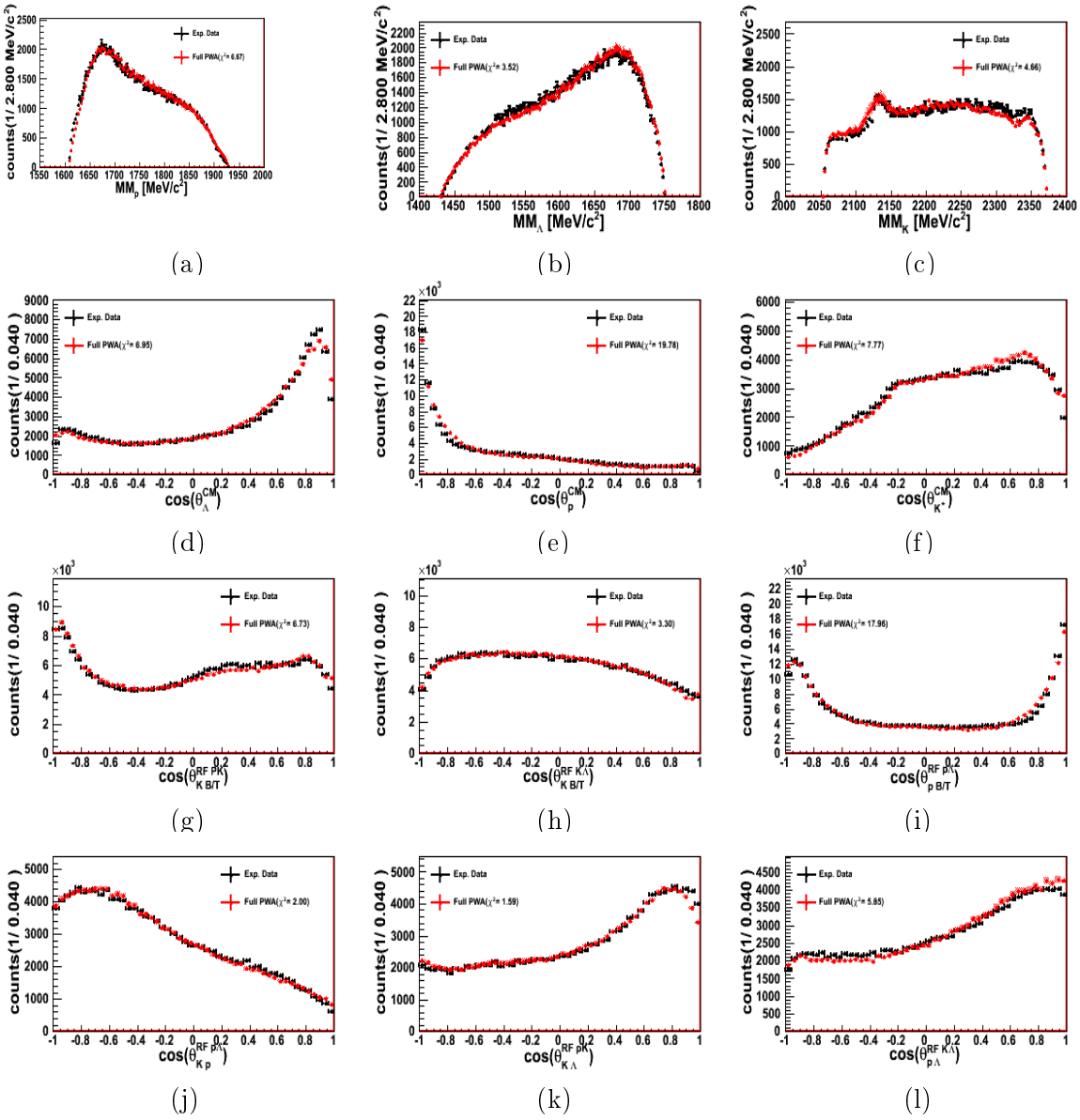

Figure B.10: Comparison of experimental data (black dots) from the data sample DISTO@2.5 GeV with the results from the Partial Wave Analysis (red dots).. Results are obtained from fitting the single data set. The plot show the Missing Mass MM_p (a), MM_λ(b) and MM_K (c), the Center-of-mass distribution ($cos\left(\theta_{cms,X}\right)$) of the Λ (d), Proton (e) and Kaon (f), the Gottfried-Jackson distributioncos $\left(\theta^{RFpK}_{KB/T}\right)$ (g),cos $\left(\theta^{RFK\lambda}_{KB/T}\right)$ (h),cos $\left(\theta^{RFp\Lambda}_{pB/T}\right)$ (f) and the Helicity angles cos $\left(\theta^{RFp\lambda}_{Kp}\right)$ (j),cos $\left(\theta^{RFpK}_{K\lambda}\right)$ (k) cos $\left(\theta^{RFK\lambda}_{K\lambda}\right)$ (l).

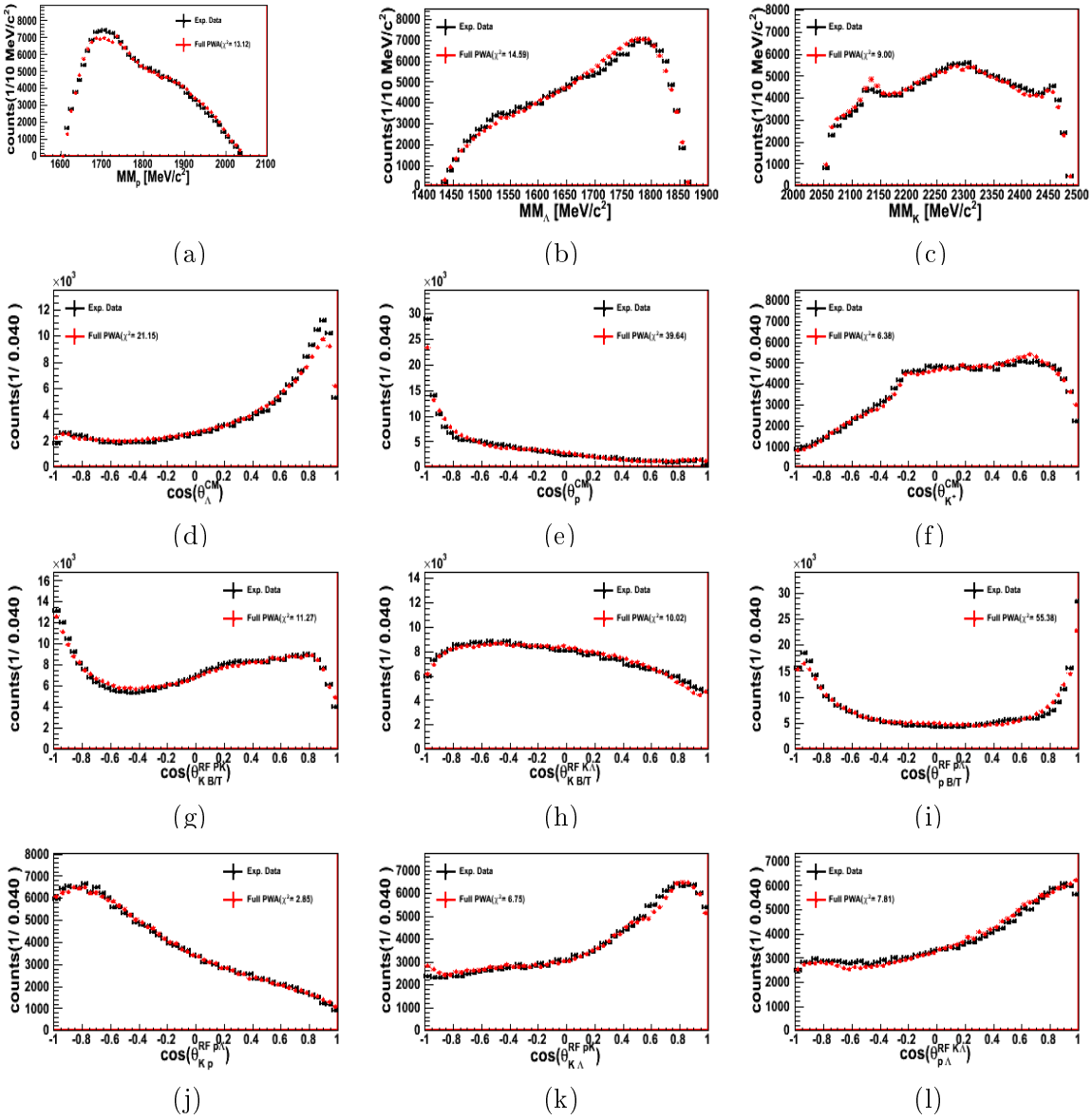

(a) (b) (c)

(d) (e) (f)

(g) (h) (i)

(j) (k) (l)

Figure B.11: Comparison of experimental data (black dots) from the data sample DISTO@2.85 GeV with the results from the Partial Wave Analysis (red dots).. Results are obtained from fitting the single data set. The plot show the Missing Mass MM_p (a), MM_λ(b) and MM_K (c), the Center-of-mass distribution ($cos\left(\theta_{cms,X}\right)$) of the Λ (d), Proton (e) and Kaon (f), the Gottfried-Jackson distributioncos $\left(\theta^{RFpK}_{KB/T}\right)$ (g),cos $\left(\theta^{RFK\lambda}_{KB/T}\right)$ (h),cos $\left(\theta^{RFp\Lambda}_{pB/T}\right)$ (f) and the Helicity angles cos $\left(\theta^{RFp\lambda}_{Kp}\right)$ (j),cos $\left(\theta^{RFpK}_{K\lambda}\right)$ (k) cos $\left(\theta^{RFK\lambda}_{K\lambda}\right)$ (l).

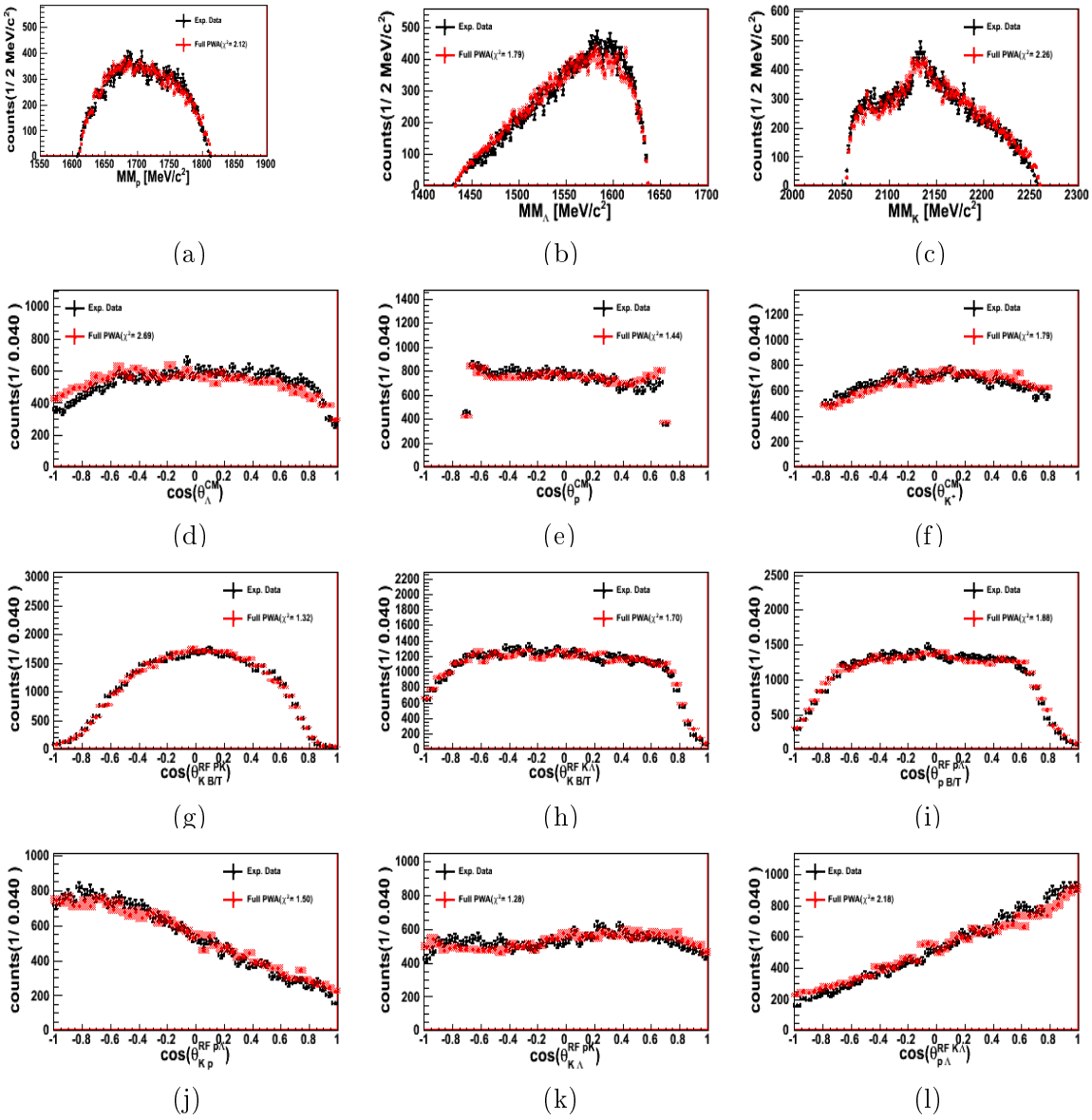

Figure B.12: Comparison of experimental data (black dots) from the data sample COSY-TOF@2.16 GeV with the results from the Partial Wave Analysis (red dots).. Results are obtained from fitting the single data set. The plot show the Missing Mass MM_p (a), MM_λ(b) and MM_K (c), the Center-of-mass distribution ($cos\left(\theta_{cms,X}\right)$) of the Λ (d), Proton (e) and Kaon (f), the Gottfried-Jackson distributioncos $\left(\theta^{RFpK}_{KB/T}\right)$ (g),cos $\left(\theta^{RFK\lambda}_{KB/T}\right)$ (h),cos $\left(\theta^{RFp\Lambda}_{pB/T}\right)$ (f) and the Helicity angles cos $\left(\theta^{RFp\lambda}_{Kp}\right)$ (j),cos $\left(\theta^{RFpK}_{K\lambda}\right)$ (k) cos $\left(\theta^{RFK\lambda}_{K\lambda}\right)$ (l).

B.b.iii.i Systematic Scan

parameter set	A	B	C	D	E
$pK\Lambda$ (direct)	$26.32 \pm 4.74\%$	$25.26 \pm 4.21\%$	$26.84 \pm 4.74\%$	$26.32 \pm 4.74\%$	$25.26 \pm 4.21\%$
$N^*(1650)$	$25.26 \pm 4.21\%$	$24.74 \pm 4.21\%$	$23.68 \pm 4.21\%$	$26.84 \pm 4.74\%$	$27.90 \pm 4.74\%$
$N^*(1710)$	$24.74 \pm 4.21\%$	$24.74 \pm 4.21\%$	$24.74 \pm 4.21\%$	$22.63 \pm 4.21\%$	$22.63 \pm 4.21\%$
$N^*(1720)$	$2.11 \pm 0.53\%$	$2.63 \pm 0.53\%$	-	-	$2.11 \pm 0.53\%$
$N^*(1875)$	$0.53 \pm 0\%$	0.53 ± 0	$0.53 \pm 0\%$	0.53 ± 0	-
$N^*(1880)$	$4.21 \pm 0.53\%$	$4.21 \pm 0.53\%$	$3.68 \pm 0.53\%$	$3.68 \pm 0.53\%$	$4.21 \pm 0.53\%$
$N^*(1895)$	$4.21 \pm 0.53\%$	$4.5 \pm 0.53\%$	$4.74 \pm 1.05\%$	$4.21 \pm 0.53\%$	$3.16 \pm 0.53\%$
$N^*(1900)$	$0.53 \pm 0\%$	-	$1.05 \pm 0\%$	-	-
S_0^+-Cusp	$1.05 \pm 0\%$	$1.05 \pm 0\%$	$1.05 \pm 0\%$	$0.53 \pm 0\%$	$1.05 \pm 0\%$
S_1^+-Cusp	$10.53 \pm 2.11\%$	$12.63 \pm 2.11\%$	$12.63 \pm 2.11\%$	$15.26 \pm 2.63\%$	$13.16 \pm 2.11\%$
D_1^+-Cusp	$0.2 \pm 0\%$	$0.2 \pm 0\%$	$0.2 \pm 0\%$	$0.2 \pm 0\%$	$0.2 \pm 0\%$

Table B.4: Contribtuion of the included channels in the DISTO@2.14 GeV sample for five parameters set of the systematical scan of the PWA for the combined analysis with the flatté parametrization.

parameter set	A	B	C	D	E
$pK\Lambda$ (direct)	$24.92 \pm 4.59\%$	$23.93 \pm 4.59\%$	$25.25 \pm 4.59\%$	$23.61 \pm 4.26\%$	$24.26 \pm 4.59\%$
$N^*(1650)$	$13.12 \pm 2.30\%$	$13.44 \pm 2.62\%$	$13.44 \pm 2.62\%$	$16.07 \pm 2.95\%$	$15.41 \pm 2.95\%$
$N^*(1710)$	$28.85 \pm 5.25\%$	$27.87 \pm 5.25\%$	$27.54 \pm 5.25\%$	$26.89 \pm 4.92\%$	$27.21 \pm 5.25\%$
$N^*(1720)$	$2.95 \pm 0.66\%$	$3.28 \pm 0.66\%$	-	-	$3.28 \pm 0.66\%$
$N^*(1875)$	$1.31 \pm 0.33\%$	$1.31 \pm 0.33\%$	$1.64 \pm 0.33\%$	$1.64 \pm 0.33\%$	-
$N^*(1880)$	$9,84 \pm 1.97\%$	$9.84 \pm 1.97\%$	$9.51 \pm 1.64\%$	$10.16 \pm 1.97\%$	$10.82 \pm 1.97\%$
$N^*(1895)$	$9,51 \pm 1.64\%$	$8.85 \pm 1.64\%$	$10.82 \pm 1.97\%$	$9.51 \pm 1.64\%$	$8.20 \pm 1.64\%$
$N^*(1900)$	$1.64 \pm 0.33\%$	-	$1.64 \pm 0.33\%$	-	-
S_0^+-Cusp	$3.28 \pm 0\%$	$0.66 \pm 0\%$	$0.33 \pm 0\%$	$0.33 \pm 0\%$	$0.33 \pm 0\%$
S_1^+-Cusp	$7.21 \pm 1.31\%$	$9.84 \pm 1.64\%$	$9.18 \pm 1.64\%$	$11.15 \pm 1.97\%$	$9.84 \pm 1.97\%$
D_1^+-Cusp	$0.2 \pm 0\%$	$0.2 \pm 0\%$	$0.2 \pm 0\%$	$0.2 \pm 0\%$	$0.2 \pm 0\%$

Table B.5: Contribtuion of the included channels in the DISTO@2.5 GeV sample for five parameters set of the systematical scan of the PWA for the combined analysis with the flatté parametrization.

parameter set	A	B	C	D	E
$pK\Lambda$ (direct)	$24.37 \pm 4.57\%$	$23.35 \pm 4.06\%$	$25.89 \pm 4.57\%$	$25.38 \pm 4.57\%$	$23.35 \pm 4.06\%$
$N^*(1650)$	$26.40 \pm 4.57\%$	$25.38 \pm 4.57\%$	$24.37 \pm 4.06\%$	$26.90 \pm 4.57\%$	$28.93 \pm 5.08\%$
$N^*(1710)$	$23.86 \pm 4.06\%$	$23.35 \pm 4.06\%$	$23.86 \pm 4.06\%$	$21.34 \pm 3.55\%$	$21.32 \pm 3.55\%$
$N^*(1720)$	$2.54 \pm 0.51\%$	$2.54 \pm 0.51\%$	-	-	$2.03 \pm 0.51\%$
$N^*(1875)$	$0.51 \pm 0\%$	$0.51 \pm 0\%$	$0.51 \pm 0\%$	$0.51 \pm 0\%$	$4.06 \pm 0.51\%$
$N^*(1880)$	$3.55 \pm 0.51\%$	$3.55 \pm 0.51\%$	$3.55 \pm 0.51\%$	$3.55 \pm 0.51\%$	$3.05 \pm 0.51\%$
$N^*(1895)$	$3.55 \pm 0.51\%$	$3.55 \pm 0.51\%$	$4.06 \pm 0.51\%$	$3.55 \pm 0.51\%$	-
$N^*(1900)$	$1.02 \pm 0\%$	-	1.02 ± 0	-	$1.02 \pm 0\%$
S_0^+-Cusp	$1.02 \pm 0\%$	$1.02 \pm 0\%$	$1.02 \pm 0\%$	$0.51 \pm 0\%$	$1.02 \pm 0\%$
S_1^+-Cusp	$12.69 \pm 2.03\%$	$15.23 \pm 2.54\%$	$15.23 \pm 2.54\%$	$17.77 \pm 3.05\%$	$15.74 \pm 2.54\%$
D_1^+-Cusp	$0.2 \pm 0\%$	$0.2 \pm 0\%$	$0.2 \pm 0\%$	$0.2 \pm 0\%$	$0.2 \pm 0\%$

Table B.6: Contribtuion of the included channels in the COSY-TOF@2.16 GeV sample for five parameters set of the systematical scan of the PWA for the combined analysis with the flatté parametrization.

parameter set	A	B	C	D	E
$pK\Lambda$ (direct)	$21.19 \pm 4.39\%$	$20.93 \pm 4.13\%$	$21.45 \pm 4.39\%$	$19.64 \pm 3.88\%$	$21.19 \pm 4.39\%$
$N^*(1650)$	$8.53 \pm 1.81\%$	$9.31 \pm 1.81\%$	$9.30 \pm 1.81\%$	$11.37 \pm 2.33\%$	$10.34 \pm 2.07\%$
$N^*(1710)$	$25.32 \pm 5.17\%$	$24.29 \pm 4.91\%$	$23.00 \pm 4.65\%$	$23.77 \pm 4.91\%$	$24.81 \pm 4.91\%$
$N^*(1720)$	$3.36 \pm 0.78\%$	$3.62 \pm 0.78\%$	-	-	$3.88 \pm 0.78\%$
$N^*(1875)$	$2.33 \pm 0.52\%$	$2.07 \pm 0.52\%$	$2.58 \pm 0.52\%$	$3.10 \pm 0.52\%$	-
$N^*(1880)$	$14.99 \pm 3.10\%$	$14.99 \pm 3.10\%$	$14.99 \pm 3.10\%$	$16.02 \pm 3.10\%$	$16.80 \pm 3.36\%$
$N^*(1895)$	$17.05 \pm 3.36\%$	$16.02 \pm 3.10\%$	$18.86 \pm 3.88\%$	$17.83 \pm 3.62\%$	$15.50 \pm 3.10\%$
$N^*(1900)$	$2.07 \pm 0.52\%$	-	$2.33 \pm 0.52\%$	-	-
S_0^+-Cusp	$0.26 \pm 0\%$	$0.52 \pm 0\%$	$0.26 \pm 0\%$	$0.2 \pm 0\%$	$0.26 \pm 0\%$
S_1^+-Cusp	$4.91 \pm 1.03\%$	$7.49 \pm 1.55\%$	$6.46 \pm 1.29\%$	$8.27 \pm 1.55\%$	$7.24 \pm 1.55\%$
D_1^+-Cusp	$0.2 \pm 0\%$	$0.2 \pm 0\%$	$0.2 \pm 0\%$	$0.2 \pm 0\%$	$0.2 \pm 0\%$

Table B.7: Contribtuion of the included channels in the DISTO@2.85 GeV sample for five parameters set of the systematical scan of the PWA for the combined analysis with the flatté parametrization.

Appendix C

C.a Flatté Spectral Function

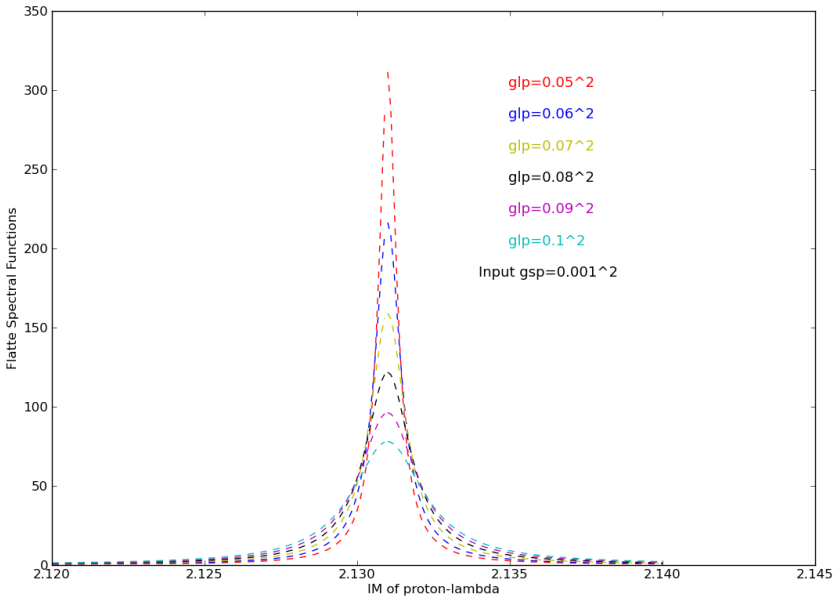

Figure C.1: Plotting of Flatté Spectral Function by python program

In Figure C.1, as coupling constant for pΛ is getting bigger, the amplitudes are reduced.

C.b Relative Momentum

In Figure C.2, the relative momentum for pΛ is always increasing, while for NΣ , the relative momentum is approaching to zero at the threshold mass. The total width shows same trend with $q_N\Sigma$.

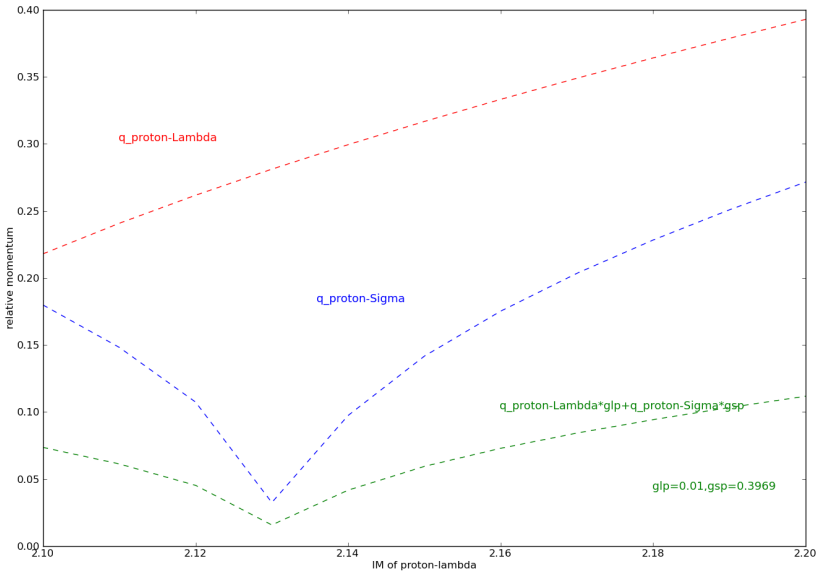

Figure C.2: Plotting of relative momentum for pΛ and NΣ two particles subsystem in Flatté Function and total partial width by python program.

Bibliography

[1] S. Abd El-Samad et al. On the σn cusp in the $pp \to pk^+\lambda$ reaction. *Eur.Phys.J.*, A49:41, 2013.

[2] Gideon Alexander, Jared A Anderson, Frank S Crawford Jr, William Laskar, and Lester J Lloyd. Interactions of lambdas with protons. *Physical Review Letters*, 7(9):348, 1961.

[3] A.V. Anisovich and A.V. Sarantsev. Partial decay widths of baryons in the spin-momentum operator expansion method. *Eur.Phys.J.*, A30:427–441, 2006.

[4] AM Badalyan, LP Kok, MI Polikarpov, and Yu A Simonov. Resonances in coupled channels in nuclear and particle physics. *Physics Reports*, 82(2):31–177, 1982.

[5] F Balestra, Y Bedfer, R Bertini, LC Bland, A Brenschede, F Brochard, MP Bussa, V Chalyshev, Seonho Choi, M Debowski, et al. Disto: a large acceptance multiparticle spectrometer for 1–3gev proton beams. *Nuclear Instruments and Methods in Physics Research Section A: Accelerators, Spectrometers, Detectors and Associated Equipment*, 426(2):385–404, 1999.

[6] V Baru, J Haidenbauer, C Hanhart, A Kudryavtsev, and Ulf-G Meißner. Flatte-like distributions and the a0 (980)/f0 (980) mesons. *The European Physical Journal A-Hadrons and Nuclei*, 23(3):523–533, 2005.

[7] J. Beringer et al. Review of particle physics (rpp). *Phys.Rev.*, D86:010001, 2012.

[8] David J Champion, Scott M Ransom, Patrick Lazarus, Fernando Camilo, Cees Bassa, Victoria M Kaspi, David J Nice, Paulo CC Freire, Ingrid H Stairs, Joeri Van Leeuwen, et al. An eccentric binary millisecond pulsar in the galactic plane. *Science*, 320(5881):1309–1312, 2008.

[9] COSY-TOF Collaboration, S Jowzaee, E Borodina, H Clement, E Doroshkevich, R Dzhygadlo, K Ehrhardt, W Eyrich, W Gast, A Gillitzer, et al. High precision measurement of the associated strangeness production in proton proton interactions. *arXiv preprint arXiv:1509.03980*, 2015.

[10] The COSY-TOF Collaboration, M Abdel-Bary, S Abdel-Samad, K-Th Brinkmann, H Clement, J Dietrich, E Doroshkevich, S Dshemuchadse, K Ehrhardt, A Erhardt, et al. Production of lambda and sigma^ 0 hyperons in proton-proton collisions. *arXiv preprint arXiv:1008.4287*, 2010.

[11] RH Dalitz and BW Downs. Hypernuclear binding energies and the λ-nucleon interaction. *Physical Review*, 111(3):967, 1958.

[12] Paweł Danielewicz. Nuclear equation of state. *arXiv preprint nucl-th/0112006*, 2001.

[13] Paul Demorest, Tim Pennucci, Scott Ransom, Mallory Roberts, and Jason Hessels. Shapiro delay measurement of a two solar mass neutron star. *arXiv preprint arXiv:1010.5788*, 2010.

[14] Eliane Epple. *Measurable consequences of an attractive $\bar{K}N$ interaction.* Dissertation, TU München, 2014.

[15] KN Ermakov, VI Medvedev, VA Nikonov, OV Rogachevsky, AV Sarantsev, VV Sarantsev, and SG Sherman. The study of the proton-proton collisions at the beam momentum 1581 mev/c. *The European Physical Journal A*, 50(6):1–6, 2014.

[16] L Fabbietti, G Agakishiev, C Behnke, D Belver, A Belyaev, JC Berger-Chen, A Blanco, C Blume, M Böhmer, P Cabanelas, et al. pk+ λ final state: Towards the extraction of the ppk- contribution. *Nuclear Physics A*, 914:60–68, 2013.

[17] L. Fabbietti, G. Agakishiev, C. Behnke, D. Belver, A. Belyaev, et al. $pk^+\lambda$ final state: Towards the extraction of the ppk^+ contribution. *Nucl.Phys.*, A914:60–68, 2013.

[18] Kenji Fukushima and Tetsuo Hatsuda. The phase diagram of dense qcd. *Reports on Progress in Physics*, 74(1):014001, 2011.

[19] J Haidenbauer, U-G Meißner, A Nogga, and H Polinder. The hyperon-nucleon interaction:conventional versus effective field theory approach. In *Topics in Strangeness Nuclear Physics*, pages 113–140. Springer, 2007.

[20] J Haidenbauer and Ulf-G Meißner. Jülich hyperon-nucleon model revisited. *Physical Review C*, 72(4):044005, 2005.

[21] B Holzenkamp, K Holinde, and J Speth. A meson exchange model for the hyperon-nucleon interaction. *Nuclear Physics A*, 500(3):485–528, 1989.

[22] BA Jacoby, A Hotan, M Bailes, S Ord, and SR Kulkarni. The mass of a millisecond pulsar. *The Astrophysical Journal Letters*, 629(2):L113, 2005.

[23] Philipp Klose. Description of 2.13gev cusp in the disto data with partial wave analysis. 2014.

[24] JM Lattimer and M Prakash. Neutron star structure and the equation of state. *The Astrophysical Journal*, 550(1):426, 2001.

[25] H Machner, J Haidenbauer, F Hinterberger, A Magiera, JA Niskanen, J Ritman, and R Siudak. Study of the λp interaction close to the σ+ n and σ0p thresholds. *Nuclear Physics A*, 901:65–88, 2013.

[26] PMM Maessen, Th A Rijken, and JJ De Swart. Soft-core baryon-baryon one-boson-exchange models. ii. hyperon-nucleon potential. *Physical Review C*, 40(5):2226, 1989.

[27] M Maggiora, DISTO collaboration, et al. New results from disto for spin observables in exclusive hyperon production. *Nuclear Physics A*, 691(1):329–335, 2001.

[28] M Maggiora, P Kienle, K Suzuki, T Yamazaki, M Alexeev, A Amoroso, F Balestra, Y Bedfer, R Bertini, LC Bland, et al. Disto data on k- pp. *Nuclear Physics A*, 835(1):43–50, 2010.

[29] K Miyagawa and H Yamamura. S-matrix poles near the λ n and σ n thresholds in the coupled λ n- σ n system. *Physical Review C*, 60(2):024003, 1999.

[30] Robert Münzer. *Search for the kaonic bound state ppK^- - Exclusive analysis of the reaction $p+p \rightarrow pK^+\Lambda$ at the FOPI experiment at GSI.* Dissertation, TU München, 2014.

[31] Wolfgang Nörenberg. *Restoration of Chiral Symmetry in Nucleus Nucleus Collisions Around 10 GeV, U.* Ges. für Schwerionenforschung, 1998.

[32] Henk Polinder, Johann Haidenbauer, and Ulf-G Meißner. Hyperon–nucleon interaction-a chiral effective field theory approach. *Nuclear Physics A*, 779:244–266, 2006.

[33] B Povh. Hypernuclei. *Annual Review of Nuclear and Particle Science*, 28(1):1–32, 1978.

[34] Th A Rijken, VGJ Stoks, and Y Yamamoto. Soft-core hyperon-nucleon potentials. *Physical Review C*, 59(1):21, 1999.

[35] Laura Fabbietti Robert Muenzer et al. Partial wave analysis for disto , cosy-tof , hades and fopi of pp to pkl data, 2015.

[36] Matthias Röder. *Final state interactions and polarization variables in the reaction pp $\rightarrow pK^+\Lambda$ close to threshold.* PhD thesis, PhD thesis, Ruhr-Universität Bochum, 2011.

[37] Matthias Röder and James Ritman. Final state interactions and polarization observables in the reaction p+p→p + K^++ Λ . In *EPJ Web of Conferences*, volume 37, page 01008. EDP Sciences, 2012.

[38] G Roger. Newton, scattering theory of waves and particles. *Texts and Monographs in Physics. Springer-Verlag*, 2, 2002.

[39] Th Roth, M Buballa, and J Wambach. Medium modifications of antikaons in dense matter. *arXiv preprint nucl-th/0504056*, 2005.

[40] T. Rozek. *Phys.Rev.Lett.*, B643:251, 2006.

[41] Jürgen Schaffner-Bielich. Hypernuclear physics for neutron stars. *Nuclear Physics A*, 804(1):309–321, 2008.

[42] Johannes Siebenson. *Strange baryonic resonances below the KN threshold - Results from p+p reactions at the HADES experiment.* PhD thesis, Technische Universität München, 2013.

[43] Simon Weissenborn, Debarati Chatterjee, and Juergen Schaffner-Bielich. Hyperons and massive neutron stars: The role of hyperon potentials. *Nuclear Physics A*, 881:62–77, 2012.

Ackownledgement

First of all, I would like to thank Prof. Laura Fabbietti for giving me the great opportunity and making this thesis possible. I also want to thank her for her outstanding motivational spirit and the brilliant input she provided. I would also like to thank for her confidence and trust to allow me doing the analysis work. I am most thankful to my supervisor Dr. Robert M$^{'}$unzer who not only taught me a lot about PWA analysis and the underlying physics but also supported me. Regarding his inspiring motivation and deep knowledge of experimental physics, I am very thankful for his involvement in my work and also spares his time reading and correcting my master thesis on this paper. Also I also would like to thank Dr. Eliane Epple who also taught me a lot on the analysis and also other people in the group. They are very supportive and very kind to offer helps in my time spending in the universe cluster.

Of course I want to thank the people I love, my parents and my friends for their outstanding motivating words and great support.